Optimization of semi-controlled low-thrust de-orbit strategies to reduce human casualty risk

Master thesis

Frank Hogervorst

Delft University of Technology

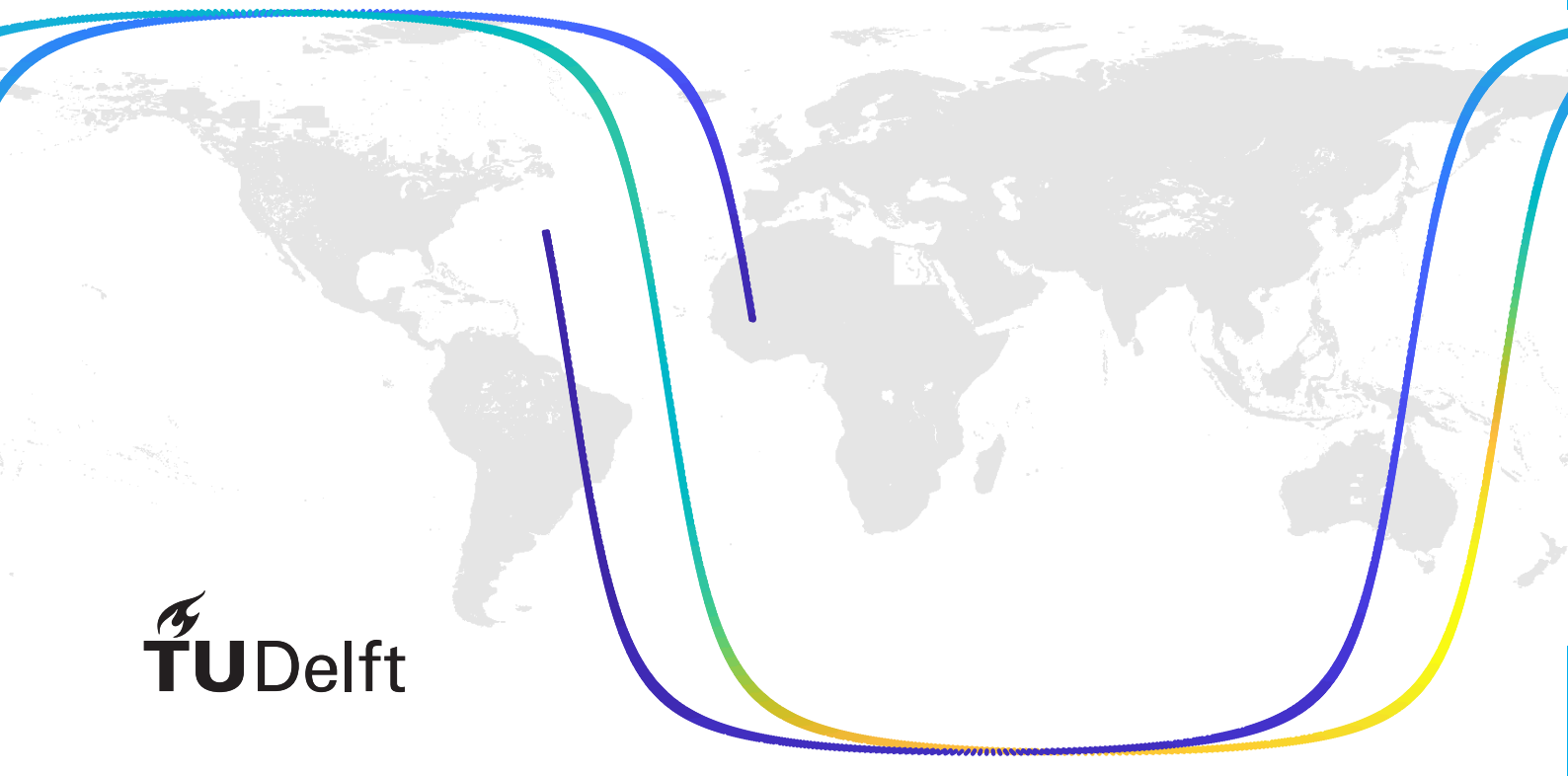

TU Delft

Optimization of semi-controlled low-thrust de-orbit strategies to reduce human casualty risk

by

Frank Hogervorst

Dissertation for the degree of

Master of Science

at The Astrodynamics and Space Missions Section,
Delft University of Technology,
to be defended publicly on Wednesday, April 25th, 2018.

Thesis committee:	Prof. dr. ir. P. N. A. M. Visser,	Committee chair
	Dr. ir. D. Dirkx,	Daily supervisor
	Dr. ir. E. Mooij,	Examinator
	Dr. ir. E. van Kampen,	External examinator

TU Delft

Nomenclature

Abbreviations and acronyms

ABM	= Adams-Bashforth-Moulton method
BS	= Bulirsch-Stoer method
CNES	= Centre National d'Études Spatiales
DE	= Differential Evolution
DLR	= German Aerospace Center
DOPRI	= Dormand and Prince method
GNC	= Guidance Navigation and Control
jDE	= self-adaptive Differential Evolution
KDE	= Kernel Density Estimation
LEO	= Low Earth Orbit
MEE	= Modified Equinoctial Elements
PDF	= Probability Density Function
PaGMO	= Parallel Global Multi objective Optimizer
RK	= Runge-Kutta method
RK7(8)	= Runge-Kutta-Fehlberg 7(8) integrator
Tudat	= TU Delft Astrodynamics Toolbox

Latin symbols

a	= semi-major axis [m]
c	= speed of light [m/s]
A	= area [m^2]
C_D, C_S, C_L	= drag, side, and lift coefficient [-]
C_R	= radiation pressure coefficient [-]
CR	= crossover factor [-]
$\mathbf{C}_{B,A}$	= transformation matrix from reference frame A to B [-]
D	= drag force [N]
e	= eccentricity [-]
E	= expected number of casualties [-]
$\frac{\Delta E}{\Delta t}$	= power of the Sun [W]
f, g, j, k	= second to fifth modified equinoctial element [-]
F	= mutation factor [-]
$\mathbf{F}$	= force vector [N]
G	= gravitational constant [$m^3/s^2/kg$]
G	= number of generations [-]
h	= altitude with respect to the spheroid [m]
H	= Hamiltonian [-]
i	= inclination [rad]
I	= MEE retrograde factor [-]
K	= ballistic coefficient [m^2/kg]
l	= true longitude [rad]
L	= lift force [N]
m	= mass [kg]
M	= mass of celestial body [kg]
n	= number of samples [-]
N	= number of casualties [-]
NP	= number of individuals in the population [-]
p	= semi-latus rectum [m]
P	= radiation pressure [Pa]

P_{nm} = Legendre polynomial of degree n and order m [-]
$P_{i,j}$ = probability of impact in point (i,j) [-]
q = dynamic pressure [Pa]
r = distance to center of mass of central body [m]
$\mathbf{r}$ = Cartesian position vector [m]
R = mean equatorial radius of central body [m]
sf = shadow function [-]
$\mathbf{s}$ = Cartesian position vector perturbing body [m]
S = side force [N]
t = time [s]
T = magnitude of the thrust force [N]
U = gravitational potential [J]
$\mathbf{U}$ = trial parameter vector of individual [-]
v = velocity [m/s]
$\mathbf{V}$ = mutated parameter vector of individual [-]
x, y, z = Cartesian position coordinates [m]
$\hat{\mathbf{x}}, \hat{\mathbf{y}}, \hat{\mathbf{z}}$ = unit vectors defining axis of reference frame [-]
$\mathbf{X}$ = parameter vector of individual [-]

Greek symbols

α = thrust steering pitch angle [rad]
β = thrust steering yaw angle [rad]
γ = flight path angle [rad]
δ = geocentric latitude [rad]
ϵ = reflectivity satellite [-]
η = flattening parameter spheroid [-]
θ = true anomaly [rad]
κ = tolerance [-]
λ = geodetic latitude [rad]
$\lambda_{\_}$ = costate [-]
μ = standard gravitational parameter [m^3/s^2]
μ^* = log normal mean [-]
ξ = probability of changing parameter F and CR [-]
ρ = density [kg/m^3]
σ = bank angle [rad]
σ^* = log normal standard deviation [-]
τ = geocentric longitude [rad]
ϕ = geodetic longitude [rad]
χ = heading angle [rad]
ω = argument of perigee [rad]
ω_{Earth} = rotational rate of the Earth [rad/s]
Ω = longitude of ascending node [rad]

Subscripts

A = aerodynamic reference frame
A = aerodynamic perturbation
B = body reference frame
c = casualty
G = gravitational perturbation
h = human
I = inertial planetocentric reference frame
nm = spherical harmonics degree and order
NTW = NTW reference frame
oc = occulted
r = reference
R = rotating planetocentric reference frame

RP = radiation pressure perturbation
SS = Sun-satellite line
TB = third body perturbation
V = vertical reference frame

Superscripts

$\dot{}$ = differentiation with respect to time
$\hat{}$ = unit vector
$'$ = parameter belongs to individual mass element dm
$*$ = scaled with shadow function

Preface

Cleaning up your own waste sounds like a naturally thing to do. However, in the space industry, this has not been the case for a long period of time and has resulted in a serious problem for current space operations. I found the problem very interesting and I knew it was up to the current generation to solve it. This thesis contains my contribution to a possible solution for this problem and I very much enjoyed working on it.

This document is submitted in partial fulfillment of the requirements for the degree of Master of Science at the faculty of Aerospace Engineering and concludes my time at the Delft University of Technology. Before diving into all the work that I have done in the last year, I would like to use this opportunity to thank those who have been the most important to me during my thesis and my time in Delft in general.

First, I would like to thank Dr.ir. Dominic Dirkx. I very much appreciate his time and effort during my literature study and thesis. Although I can be short-spoken and often required only 30 minutes or less for a meeting, there was always a full hour planned in his schedule, every week, to discuss my progress of that week or discuss personal matters. I have always looked forward to these weekly meetings. He saved me valuable time by providing a helping hand when I got stuck with my code, some problems were solved even before I could get a cup of coffee. His critical views and enthusiasm about my results inspired me throughout my thesis.

Next, I would like to thank my friends from office 2.60. The (mostly) punctual brakes encouraged me to work efficiently. Sparring about problems with my research has helped me improve the quality significantly. But mostly I want to thank them for taking my mind off work, the drinks on Friday, and the occasional drone-flying.

Finally, I would like to thank my friends and family. They have made my time as a student in Delft epic and have supported me throughout my studies. Especially during the rough times in the past year.

Frank Hogervorst
Delft, April 2018

Abstract

Currently, an increasing amount of debris is floating in Low Earth Orbit (LEO) endangering space operations. Left-over rocket stages and non-operational satellites increase the risk of in-orbit collisions, which in turn, increase the amount of debris floating in the LEO region. The current use of the space environment is not sustainable, and therefore, measures need to be taken to reduce the amount of space debris. Currently, ESA set a requirement that all launched objects need to re-enter within 25 years with a maximum risk of 1 casualty per 10000 re-entries.

One method to meet both of these requirements is to employ a semi-controlled de-orbit strategy for end-of-life satellites using electric low-thrust propulsion. In this strategy the satellite is controlled from the end-of-life orbit down to low altitudes (120 to 200 km). From this altitude the satellite follows a ballistic trajectory towards the surface of the Earth. The target of such maneuver is to phase the impact probability track, which is the result of uncertainties in the applied models, with the Earth, such that the resulting impact track covers mostly uninhabited areas. Controlling only a part of the re-entry results in mass savings on the satellite compared to fully controlled entries. These fully controlled entries require larger thrust levels, which in general, require propulsion systems which are heavier and less fuel efficient than electric low-thrust propulsion systems. Because the mass of a satellite is strongly related to mission costs, the semi-controlled de-orbit strategy is an interesting alternative for fully controlled de-orbit strategies. Furthermore, the semi-controlled strategy can reduce the risk of casualties compared to the uncontrolled case. Recent studies found reductions of the casualty risk of more than one order of magnitude. However, these studies made assumptions to calculate the casualty risk of such semi-controlled entries but did not investigate the effect of these assumptions properly. Therefore, the objective of this thesis, is to provide insights into the effects of these assumptions. Furthermore, the extent to which the casualty risk can be reduced is investigated. Current literature mostly focuses on reaching the requirement set by ESA, while it is also interesting to see the actual reductions possible such that the strategy is employed more often and the risk for the human population is reduced.

To fulfill the objective of this thesis, two optimization strategies are carried out. First, the control profile for the complete semi-controlled de-orbit strategy is optimized for minimum casualty risk using a differential evolution algorithm. The simulation of the complete strategy provides insight into the extent if the reduction in casualty risks achievable with the semi-controlled de-orbit strategy. Furthermore, this method allows for the preliminary investigation of the achievable states at the point where to controls are turned off. These states are expected to have a large influence on the value of the resulting casualty risk and are therefore important for analyzing the semi-controlled de-orbit strategy. Second, the initial state of the ballistic trajectory, at the point where the controls are turned off, is also optimized for minimum casualty risk using a differential evolution algorithm. This optimization method is applied to reduce the computational effort of the optimization and allows for easier calculation of the effects of the assumptions made in previous research. In case similar impact tracks are achieved for both optimizations, future analysis of the semi-controlled de-orbit strategy can be performed which less computational effort.

Employing a semi-controlled low-thrust de-orbit strategy can reduce the casualty risk with 2 to 3 orders of magnitude with respect to an uncontrolled de-orbit strategy. Large ballistic coefficients are beneficial for the reduction of the casualty risk. Furthermore, orbits with high inclinations results in larger reductions of the casualty risk with respect to low inclination orbits. Also the results for low inclination orbits are less sensitive to errors in the re-entry state caused by imperfections in the GNC system of the satellite during the de-orbit maneuver. The lower sensitivity is the result of a better configuration of the impact track with respect to the large land masses on Earth. To find optimal impact tracks on the Earth, it is sufficient to optimize only the last 150 km of the trajectory. In case an accurate estimation for the value for the casualty risk is needed, higher fidelity models must be applied and the uncertainties in initial state at 150 km need to be investigated in more detail. The assumptions made in previous research influence the results with less than 33% and can easily be applied when an optimal impact track is sought for with low fidelity models. For investigating the range of re-entry conditions

for which the resulting casualty risk is below the set requirement, some of the assumptions cannot be applied since it limits the solution space for the GNC system to target. Furthermore, in case an accurate value for the risk needs to be found, high-fidelity models are required and in that case, the effect if the assumptions is too large.

Contents

Nomenclature iii

Abstract ix

1 Introduction 1
- 1.1 Research questions . . . 3
- 1.2 Report outline . . . 3

2 Dynamical model 5
- 2.1 Reference frames . . . 5
- 2.2 State representation . . . 6
- 2.3 Transformations . . . 6
- 2.4 Equations of motion . . . 7
- 2.5 Perturbations . . . 8
  - 2.5.1 Aerodynamic . . . 8
  - 2.5.2 Gravitational . . . 9
  - 2.5.3 Solar radiation . . . 10
  - 2.5.4 Propulsive perturbation . . . 10
- 2.6 Control parameterization . . . 11

3 Numerical methods 15
- 3.1 Integrator . . . 15
- 3.2 Differential evolution . . . 16
  - 3.2.1 Classic differential evolution . . . 17
  - 3.2.2 Self-adaptive differential evolution . . . 17
- 3.3 Kernel density estimation . . . 19
- 3.4 Casualty risk calculation . . . 19

4 Simulation setup 23
- 4.1 Simulation cases . . . 23
- 4.2 Assumptions . . . 23
- 4.3 Perturbation analysis . . . 24
- 4.4 Propagation termination altitude . . . 26
- 4.5 Impact probability distribution . . . 27
- 4.6 Control cut-off altitude . . . 29
- 4.7 Validation . . . 30
- 4.8 Optimization complete de-orbit strategy . . . 31
- 4.9 Optimization last 150 km . . . 32

5 Results and discussion 33
- 5.1 Case 1: PARASOL . . . 33
- 5.2 Case 2: SMOS . . . 36
- 5.3 Case 3: SPOT5 . . . 37
- 5.4 Case 4: SPOT5LIKE . . . 38
- 5.5 General discussion of results . . . 40

6 Sensitivity analysis 43
- 6.1 Exact state at 150 km altitude . . . 43
  - 6.1.1 Case 1: PARASOL . . . 43
  - 6.1.2 Case 2: SMOS . . . 44
  - 6.1.3 Case 3: SPOT5 . . . 45
  - 6.1.4 Case 4: SPOT5LIKE . . . 46
  - 6.1.5 General discussion on the sensitivity to deviations in state at 150 km . . . 46

6.2 Seed variability . . . 48
6.3 Population growth . . . 49
6.4 Effect of a normally distributed impact probability function . . . 50

7 Conclusions and recommendations **53**
7.1 Conclusions . . . 53
7.2 Recommendations . . . 56
7.3 Implications . . . 57

A Verification **59**
A.1 Control parameterization . . . 59
A.2 Differential evolution . . . 63
A.2.1 Initial conditions and objective function . . . 63
A.2.2 Single orbital element targeting . . . 64
A.2.3 Multiple orbital elements targeting . . . 64
A.3 Optimization with simple population map . . . 65
A.3.1 Latitude dependent population map . . . 66
A.3.2 Longitude dependent population map . . . 67

B Optimal low-thrust trajectories. **69**

Bibliography **73**

1 Introduction

The amount of space debris in Low Earth Orbit (LEO) is increasing, this is caused by amongst others, left-over rocket upper stages, non-operational satellites, and fragments of satellite caused by the intentional or accidental break-up of satellites. This debris poses a large problem for space operations nowadays as the risk for collisions is increasing. Currently, thousands of pieces of space debris need to be tracked and satellites frequently require orbit maneuvering to avoid debris to safeguard operations [1]. The current use of the space environment is not sustainable. Therefore, to limit the contribution of the end-of-life satellites to the space debris problem, action is taken. This is mainly accomplished by decreasing the perigee of the satellites, such that the satellites re-enter the atmosphere within 25 years after mission completion. The 25 year limit is a requirement for all European space missions as defined in Ref. [2]. Examples of missions that decrease their perigee at the end-of-life are the Upper Atmosphere Research satellite, the Akari satellite, and the ERS-2 satellite [3][1]. However, these re-entries are uncontrolled, resulting in impact locations of the debris that can be at any latitude between plus and minus the value of the inclination of the orbit. In contrast, another option for the disposal of a satellite at end-of-life is to perform a controlled re-entry. Such a re-entry utilizes high-thrust engines to steer the satellite towards uninhabited areas of the Earth. However, these controlled re-entries require either the addition of a propulsion system or additional fuel on board of the satellite, both of which increase the launch mass, which is in turn closely related to the cost of the space mission.

In an effort to limit the amount of space debris in the future, ESA has defined the 'Space Debris Mitigation Policy for Agency Project' in Ref. [2] and the corresponding implementation guidelines in Ref. [4]. The policy demands controlled re-entries over unpopulated areas if the casualty risk for uncontrolled re-entry exceeds a value of 10^{-4}. This casualty risk is defined as the probability of having at least one casualty resulting from the re-entry. Luckily, to date, there are no confirmed casualties as a result of the impact of debris from space. The method of calculating this casualty risk for both controlled and uncontrolled re-entry is extensively described in Ref. [4].

For satellites between 700 kg and 2500 kg, adding a high-thrust propulsion system to perform a controlled re-entry at end-of-life is expensive in terms of the mass required [1]. Below this mass range, the risk is often below the limit that has been set for the casualty risk. For higher masses a controlled re-entry is necessary as the casualty risks are too high and controlled re-entry is required. To limit the costs of the end-of-life strategy for space missions, use can be made of a semi-controlled re-entry utilizing an electric low-thrust propulsion system. Electric low-thrust propulsion systems are often lighter and more fuel efficient than high-thrust propulsion systems, reducing the impact on the launch mass and therefore the mission costs [5]. In a semi-controlled re-entry strategy, the satellite is slowed down according to a controlled thrust profile from its end-of-life orbit down to the Earth. However, the last part of the re-entry is dominated by large atmospheric perturbations. Due to these perturbations, the attitude control system is no longer capable of providing accurate controls to maintain the desired attitude [6]. The altitude limit for the attitude control system is located around 150 km altitude [6]. The controls are turned off at this altitude and the satellite continues on an uncontrolled trajectory towards the surface,

[1] NASA Orbital Debris Program Office, "Orbital Debris Quaterly News October 2011 and January 2012" https://orbitaldebris.jsc.nasa.gov/quarterly-news/newsletter.html retrieved 16/1/2017

hence the name semi-controlled re-entry. The point where the controls are turned off, determines the orientation of the impact probability track on the Earth. The associated casualty risk of the end-of-life disposal maneuver is minimized by an optimal placement of this impact track on the Earth.

ESA is investigating the different end-of-life strategies for LEO satellites in order to reduce the contribution of non-operational satellites to the space debris problem. Therefore, ESA announced a statement of work in Ref. [1]. This requested research is a follow-up on feasibility studies performed by the German Aerospace Center (DLR) and Centre National d'Études Spatiales (CNES) [6, 7]. Reference [7] recommends to put non-operational satellites in an orbit with a lifetime between 15 and 40 years. Note that this study formed the basis of the 25 year requirement set later by ESA in Ref. [2]. The use of electric propulsion systems to perform a semi-controlled re-entry was not found to be the optimal solution in terms of mass. This is because none of the considered satellites in Ref. [7] are equipped with electric propulsion systems. Therefore, an electric propulsion system needed to be added to the satellites, which was not effective in terms of mass, and made that particular solution undesirable. However, the study notes that if an electric propulsion system would have already been on board of the satellite, and if the satellites have enough power and mass, the outcomes of the study could be significantly different [7]. Currently more satellites are equipped with electric propulsion systems for station-keeping purposes and the power generation and efficiency of the engines have increased [8, 9]. These factors all increase the feasibility of a semi-controlled disposal strategy.

To further analyze the semi-controlled disposal strategy, a study on the feasibility of low-thrust propulsion de-orbit strategies was performed by CNES [6]. This study reports that semi-controlled strategies could reduce the risk in comparison with uncontrolled re-entries with a factor 10 [6]. These results are promising, but there are still some gaps in the current knowledge to verify the feasibility of semi-controlled disposal strategy. For example, current efforts have not investigated the trajectory from the end-of-life orbit towards atmospheric capture in detail. Since the achievable states at atmospheric capture are determined by the end-of-life trajectory, it is essential to verify the combination of the controlled and uncontrolled part of the de-orbit maneuver. Furthermore, the resulting range of achievable states at capture could influence the results presented in Ref. [6], because that work makes assumptions to simplify the controlled part of the re-entry. The assumptions made in Ref. [6] are the following. First, a normally distributed impact probability function was used for the calculation of the casualty risk of the end-of-life disposal maneuver. Also, this probability function is assumed to be constant for all possible latitudes of the point of atmospheric capture. And finally, the orbit at atmospheric capture has a flight path angle of 0° and the point of atmospheric capture can be located at any latitude between plus and minus the value for the inclination [6].

This thesis investigates the impact of these assumptions by simulating the complete semi-controlled disposal strategy from the end-of-life orbit down to the ground. For the sake of comparison, this thesis employs the same cases as used in Ref. [6]. The considered cases have distinct characteristics, allowing to investigate a large range of LEO satellites for which this strategy could be viable. The simulations of the semi-controlled disposal strategy are performed using the TU Delft Astrodynamics Toolbox (Tudat), which is "a set of C++ libraries that support astrodynamics and space research" [2]. Using this toolbox, the trajectory of the satellite is simulated from the end-of-life orbit to the ground. This trajectory is controlled by the low-thrust propulsion system on-board the satellite down to the altitude where the controls are turned off because the atmospheric perturbations are too large. This trajectory is optimized by using the Parallel Global Multi-objective Optimizer (PaGMO) developed by ESA [10]. The control profile is constructed using the method of control parameterization based on optimal control theory, in order to limit the number of control parameters for the optimization [11]. From the point where the controls are turned off, the satellites follows a ballistic trajectory. During this phase uncertainties in atmospheric density and incomplete knowledge of the satellite parameters causes uncertainties in the location of the satellite. These uncertainties result in an impact probability distribution function (PDF) around the nominal impact point. This PDF does not resemble continuous distributions known from probability theory as was found in Ref. [12, 13]. Therefore, a non-parametric method called Kernel Density Estimation (KDE) is used to find the impact PDF. Combining the knowledge of the nominal trajectory and the PDF, a probability impact track on the Earth can be constructed. This impact track, in combination with a population map of the Earth and information about the size of the satellite that survived the re-entry, results in a value for the casualty risk. The population map is obtained

[2] Astrodynamics & Space Missions, "TU Delft Astrodynamics Toolbox", `https://github.com/Tudat/tudat` retrieved 26/02/2018

from Ref. [14] which uses population data from national and subnational administrative units for the construction of the population map. The same data is used in risk assessment tools such as ESAs Debris Risk Assessment and Mitigation Analysis tool and NASAs Debris Assessment Software [15, 16]. The information about the size of the satellite surviving entry is found from literature in Ref. [4].

To fulfill the objective of this thesis, two optimization strategies are carried out. First, the control profile for the complete semi-controlled disposal strategy is optimized for minimum casualty risk using a differential evolution algorithm. As the complete strategy is simulated this gives insight into what casualty risks are achievable with the trajectory. Furthermore, this strategy allows for the investigation of the achievable states at the point where to controls are turned off, since the values for the thrust are low, the achievable flight path angles are small. The achievable flight path angles are further reduced by the drag which circularizes the orbit. The states at the points where the controls are turned off are expected to have a large influence on the value of the resulting casualty risk and are therefore important for analyzing the semi-controlled de-orbit strategy. Second, the initial state of the ballistic trajectory, at the point where the controls are turned off, is also optimized for minimum casualty risk using a differential evolution algorithm. This optimization strategy is applied to reduce the computational effort of the optimization, since the low-thrust maneuver from the end-of-life orbit towards the point where to controls are turned off requires several months of thrusting, which is computationally intensive. It is interesting to see whether both optimization strategies find similar optimal impact tracks. In case similar impact tracks are achieved, future analysis of the semi-controlled disposal strategy can be performed which less computational effort. The results of both optimizations are essential to verify that the optimized states of ballistic trajectory optimization are actually achievable by the satellites under consideration and to verify the results of Ref. [6] which did not perform an analysis of the controlled part of the strategy.

1.1. Research questions

The research presented in this thesis will perform the next step of the investigation on the feasibility of the semi-controlled end-of-life de-orbit strategy. To clearly define the aim of this research, the following research questions have been formulated:

1. What is the reduction in casualty risk possible by employing a semi-controlled end-of-life disposal strategy compared to an uncontrolled strategy?
   (a) What is the effect of only propagating the uncontrolled part of the disposal strategy compared to propagating the complete disposal strategy from the end-of-life orbit?
   (b) What is influence of different ballistic coefficients and/or different initial mass of the satellite on the calculated casualty risk?
   (c) To what extent does the inclination of the end-of-life orbit affect the calculated casualty risk?
2. To what extent do the assumptions made in Ref. [6] affect the calculated casualty risk of the semi-controlled disposal strategy?
   (a) What is the effect of assuming a circular orbit at the point of atmospheric re-entry for the calculation of the casualty risk?
   (b) What is the effect of scaling the casualty risk with the average population growth with respect to regional expected population growth?
   (c) What is the effect of assuming a normally distributed impact probability function for the calculation of the casualty risk with respect to a non-parametric probability function dependent on the location of the atmospheric re-entry?

1.2. Report outline

The outline of this research is structured as follows. First, in Chapter 2, the dynamical model used in the simulations is described. This chapter contains the used framework and discusses the discretization of the control profile to reduce the amount of control parameters used in the optimizations. Following this, the necessary numerical methods are described in Chapter 3. These methods are required for the numerical propagation of the satellite cases and both optimizations. Furthermore, it is required to find the associated casualty risks for both optimizations. Next, in Chapter 4, the different satellite cases from Ref. [6] are discussed, as well as the assumptions made during this research. Chapter 4

also contains the investigations that have been carried out to limit the computational effort for the optimizations. Furthermore, intermediate results are discussed, which are subsequently integrated into the simulator for the optimizations. The chapter concludes with the results from the validation of the complete simulation setup, and an overview of setup for both optimization strategies. After that, the results are presented in Chapter 5, where the results for all cases are discussed, and a general discussion of the findings is presented. Then, in Chapter 6, the sensitivity of the obtained results is analyzed and the assumptions made in Chapter 4 are assessed for validity. The report ends with the conclusions, recommendations, and implications of this research in Chapter 7.

2

Dynamical model

This chapter contains the dynamical framework for this research. It forms the groundwork on which the optimizations are performed. To correctly model the state of the satellite, and all perturbations on the satellite, first the relevant reference frames and state representations are described in Sections 2.1 and 2.2 respectively. Next, the transformations between these reference frames and states are discussed in Section 2.3, as these are used in all stages of the research. Then, two relevant sets of equations of motion are described in Section 2.4, where the first set utilizes a Cartesian state representation for the propagation of the satellite, and the second set employs Modified Equinoctial Elements used for the parameterization of the control. The perturbing accelerations which are fed into the equations of motion are described in Section 2.5. Finally, in Section 2.6, the parameterization of the controls is discussed.

2.1. Reference frames

The reference frames used in this research are described below.

- **Inertial planetocentric reference frame**, $\hat{\mathbf{x}}_I, \hat{\mathbf{y}}_I, \hat{\mathbf{z}}_I$: this reference frame has an inertial orientation and is centered on the center of mass of the central body. The $\hat{\mathbf{z}}_I$-axis points North along the rotational axis of the central body and the $\hat{\mathbf{x}}_I$-axis is pointing to the Vernal Equinox on January 1, 2000, 12:00 (noon) [17]. The $\hat{\mathbf{y}}_I$-axis completes the right-handed system [18].
- **Rotating planetocentric reference frame**, $\hat{\mathbf{x}}_R, \hat{\mathbf{y}}_R, \hat{\mathbf{z}}_R$: this reference frame is centered on the center of mass of the central body and co-rotates with the central body. The $\hat{\mathbf{z}}_R$-axis points North along the rotational axis of the central body, the $\hat{\mathbf{x}}_R$-axis intersects the equator at zero longitude, and the $\hat{\mathbf{y}}_R$ completes the right-handed system [18].
- **Vertical reference frame**, $\hat{\mathbf{x}}_V, \hat{\mathbf{y}}_V, \hat{\mathbf{z}}_V$: the origin is located at the center of mass of the satellite. The $\hat{\mathbf{z}}_V$-axis points in the direction of the local vertical along the radial component of the gravitational acceleration. The $\hat{\mathbf{x}}_V$-axis points towards the Northern Hemisphere and lies in the meridian plane. The $\hat{\mathbf{y}}_V$-axis completes the right-handed system [18].
- **Normal tangential W (NTW) reference frame**, $\hat{\mathbf{x}}_{NTW}, \hat{\mathbf{y}}_{NTW}, \hat{\mathbf{z}}_{NTW}$: the origin is located at the center of mass of the satellite. The $\hat{\mathbf{x}}_{NTW}$-axis lies in the orbital plane and points outward away from the direction of Earth. The $\hat{\mathbf{y}}_{NTW}$-axis is tangent to the velocity vector, and the $\hat{\mathbf{z}}_{NTW}$-axis is normal to the orbital plane and completes the right-handed system [19]. This reference frame is used for the control parameterization as discussed in Section 2.6.
- **Body reference frame**, $\hat{\mathbf{x}}_B, \hat{\mathbf{y}}_B, \hat{\mathbf{z}}_B$: the origin is located at the center of mass of the satellite. The $\hat{\mathbf{x}}_B$-axis points along the direction of the thrust acceleration. The $\hat{\mathbf{z}}_B$-axis points downward in nominal mode. The $\hat{\mathbf{y}}_B$-axis completes the right-handed system [18].
- **Aerodynamic reference frame (airspeed based)**, $\hat{\mathbf{x}}_A, \hat{\mathbf{y}}_A, \hat{\mathbf{z}}_A$: the origin is located at the center of mass of the satellite, the $\hat{\mathbf{x}}_A$-axis in the direction of the velocity relative to the rotating planetocentric frame R. The $\hat{\mathbf{z}}_A$-axis is aligned with the lift force but opposite in direction. The $\hat{\mathbf{y}}_A$-axis completes the right-handed system.

2.2. State representation

The state representations used in this research are discussed below.

- **Cartesian state representation** $[x, y, z, \dot{x}, \dot{y}, \dot{z}]$: where x, y, and z are the position coordinates, and $\dot{x}$, $\dot{y}$, $\dot{z}$ the velocity components. This state representation is used in Tudat for the propagation of the satellite. The propagation of the equations of motion is performed in the inertial planetocentric reference frame as discussed in Section 2.1.
- **Keplerian elements state representation** $[a, e, i, \omega, \Omega, \theta]$: where a is the semi-major axis, e and i the eccentricity and inclination. ω the argument of perigee, Ω the longitude of the ascending node and θ the true anomaly. This state representation is used for visualization of orbits as these elements are easily interpretable for users. It is further used to set the initial orbit of the satellite. Note that this state representation has singularities at $e = 0$, $e = 1$, $i = 0$, $i = \pi$, where either ω or Ω are undefined.
- **Spherical orbital state representation** $[r, \tau, \delta, \gamma, \chi, v]$: where r is the distance between the satellite and the center of mass of the central body. τ and δ are geocentric longitude and latitude. Furthermore, γ and χ are the flight path angle and heading angle respectively and v indicates the magnitude of the velocity. This state representation is used to set the flight path angle for the initial state of the Monte Carlo simulations in Section 4.5.
- **Geodetic state representation** $[h, \phi, \lambda]$: where h is the altitude above the spheroid, ϕ the geodetic longitude, and λ the geodetic latitude. The WSG-84 spheroid is used for the shape of the Earth because this is used in both Tudat[1] and by the population map as discussed in Section 3.4 [14]. The coordinates are relative to the rotating planetocentric reference frame R as discussed in Section 2.1. This representation is used to find the population density on the surface of the Earth for the calculation of the casualty risk as described in Section 3.4.
- **Modified Equinoctial Elements (MEE) state representation** $[p, f, g, h, k, l]$: where p is the semi-latus rectum, f, g, h and k the second, third, fourth, fifth equinoctial elements and l the true longitude. MEE are nonsingular for all eccentricities and inclinations. The reference cases discussed in this thesis are near circular as described in Section 4.1. The behavior of MEE is much more stable for near circular orbits compared to Keplerian elements [20]. Therefore, this elements set is used in this thesis for the control parameterization as discussed in Section 2.6. This results in more stable behavior for the thrust steering angles.

2.3. Transformations

Transformations between any two reference frames A and B are performed with transformation matrices denoted by $\mathbf{C}_{B,A}$. The rotation sequence used for all transformations is 1-3-2[1]. The transformations between the I, R, V, NTW, B and A reference frames, are described in Ref. [18] and are already extensively tested and validated within Tudat. Therefore, the rotation matrices are not given here. Only a description of what parameters are required to perform each of these transformations is given by:

$$\mathbf{C}_{I,R}(\omega_{Earth}, t), \quad (2.1a) \qquad \mathbf{C}_{R,V}(\tau, \delta), \quad (2.1b) \qquad \mathbf{C}_{V,NTW}(\gamma, \chi), \quad (2.1c) \qquad \mathbf{C}_{NTW,B}(\alpha, \beta), \quad (2.1d) \qquad \mathbf{C}_{NTW,A}(\sigma), \quad (2.1e)$$

where ω_{Earth} is the rotational rate of the Earth, t the time from January 1, 2000, 12:00 (noon), α and β the thrust steering angles as will be discussed in Section 2.6, and σ indicates the bank angle.

In Eq. (2.2) the transformations between state representations are shown. The transformations between state representations are described in Ref. [21] and are already extensively tested and validated with Tudat. Therefore, Eq. (2.2) merely describes what parameters are required to perform each of the relevant transformations. Parameters in brackets indicate what additional information is required.

[1] Astrodynamics & Space Missions, "TU Delft Astrodynamics Toolbox", `https://github.com/Tudat/tudat` retrieved 26/02/2018

Cartesian $\overset{(\mu)}{\longleftrightarrow}$ Kepler, (2.2a)

Cartesian $\longleftrightarrow$ Spherical, (2.2b)

Cartesian $\overset{(R,\eta,\kappa)}{\longleftrightarrow}$ Geodetic, (2.2c)

Kepler $\overset{(\mu,I)}{\longleftrightarrow}$ MEE, (2.2d)

where μ is the standard gravitational parameter, I the retrograde factor where $I = 1$ for posigrade and $I = -1$ for retrograde orbits [22], R the mean equatorial radius of the central body, η the flattening parameter as given by the WSG-84 spheroid, and κ the tolerance for the iterative procedure to find the coordinates.

As the MEE are important for the control parameterization discussed in Section 2.6, the state transformation between Keplerian elements and MEE as shown in Eq. (2.2d) is described in more detail here. This also gives an idea of the expected behavior for the control parameterization verification as described in Appendix A.1. The MEE can be expressed in terms of Keplerian elements as [22]:

$$p = a(1 - e^2), \tag{2.3a}$$

$$f = e\cos(\omega + I\Omega), \tag{2.3b}$$

$$g = e\sin(\omega + I\Omega), \tag{2.3c}$$

$$h = \tan^I(i/2)\cos\Omega, \tag{2.3d}$$

$$k = \tan^I(i/2)\sin\Omega, \tag{2.3e}$$

$$l = \omega + I\Omega + \theta. \tag{2.3f}$$

Note that parameters f and g are both dependent on e, ω, and Ω. Similarly, parameters h and k are depending on i and Ω. Equation (2.3) shows the advantage of MEE over Keplerian elements. For near zero eccentricity orbits, the value for ω could have rapid oscillations as the result of perturbation on the orbit. However, the variations in parameters f and g, which contain information about ω, are small for low values of eccentricity and does not exhibit such large oscillations [22]. When using these parameters for the control steering angles as defined in Section 2.6 the resulting control profile is also much more stable.

2.4. Equations of motion

The translational state of the satellite in the inertial reference frame as described in Section 2.1 is defined by the Cartesian position vector $\mathbf{r}_I = [x_I, y_I, z_I]$, and the velocity vector $\dot{\mathbf{r}}_I = [\dot{x}_I, \dot{y}_I, \dot{z}_I]$. The translational equations of motion are given by[19]

$$\frac{\mathrm{d}^2\mathbf{r}_I}{\mathrm{d}t^2} = \frac{\mathrm{d}\dot{\mathbf{r}}_I}{\mathrm{d}t} = \ddot{\mathbf{r}}_I = \frac{\sum \mathbf{F}}{m}, \tag{2.4}$$

where $\ddot{\mathbf{r}}_I$ are all perturbing accelerations in the inertial reference frame I as will be discussed in Section 2.5, and $\mathbf{F}$ the perturbing forces acting on the satellite. m indicates the mass of the satellite. The Gaussian variational equations for MEE as described in Section 2.2 are given in Eq. (2.5) [23, 24]. These are used for the control parameterization as discussed in Section 2.6. Note that the variational equation for the true longitude is not provided, because it is not used in the control parameterization as will be discussed in Section 2.6. This parameter is not used in the control parameterization because only the value of the true longitude at the end of the disposal maneuver is of interest which is controlled by correctly timing the re-entry into the atmosphere.

$$\frac{\mathrm{d}p}{\mathrm{d}t} = \sqrt{\frac{p}{\mu}}\frac{2p}{w}\ddot{y}_{NTW}, \tag{2.5a}$$

$$\frac{\mathrm{d}f}{\mathrm{d}t} = \sqrt{\frac{p}{\mu}}\left(\ddot{x}_{NTW}\sin l + \frac{((w+1)\cos l + f)\,\ddot{y}_{NTW}}{w} - \frac{g\,(h\sin l - k\cos l)\,\ddot{z}_{NTW}}{w}\right), \tag{2.5b}$$

$$\frac{\mathrm{d}g}{\mathrm{d}t} = \sqrt{\frac{p}{\mu}}\left(-\ddot{x}_{NTW}\cos l + \frac{((w+1)\sin l + g)\,\ddot{y}_{NTW}}{w} - \frac{f\,(h\sin l - k\cos l)\,\ddot{z}_{NTW}}{w}\right), \tag{2.5c}$$

$$\frac{\mathrm{d}h}{\mathrm{d}t} = \sqrt{\frac{p}{\mu}}\frac{s^2}{2w}\ddot{z}_{NTW}\cos l, \tag{2.5d}$$

$$\frac{\mathrm{d}k}{\mathrm{d}t} = \sqrt{\frac{p}{\mu}}\frac{s^2}{2w}\ddot{z}_{NTW}\sin l, \tag{2.5e}$$

with auxiliary variables

$$s^2 = 1 + h^2 + k^2,$$
$$w = 1 + f\cos l + g\sin l,$$

and $\ddot{x}_{NTW}$, $\ddot{y}_{NTW}$, and $\ddot{z}_{NTW}$ are the perturbing accelerations in the NTW frame as discussed in Section 2.1. Equation (2.5) shows that the value of the semi-latus rectum, p, is controlled by thrusting in the direction of velocity. Parameters h and k, which are related to the inclination and longitude of ascending node as shown in Eq. (2.3), are influenced by thrusting perpendicular to the orbital plane. The remaining parameters f and g are influenced by any direction of the thrust, since these are related to the eccentricity and argument of perigee, which are influenced by perturbations within the orbital plane but also related to the longitude of ascending node with is influenced by thrusting perpendicular to the orbital plane.

2.5. Perturbations

For correct modeling of the satellite orbit, multiple perturbations need to be incorporated into the model. This section describes the perturbations used in the simulations, which are all used in the equations of motion in Eq. (2.4). In Section 4.3 an analysis of these perturbations will be performed to find the perturbations which need to be taken into account during the optimizations. All perturbations in this section are combined in $\ddot{\mathbf{r}}_I$ with:

$$\ddot{\mathbf{r}}_I = \ddot{\mathbf{r}}_{A,I} + \ddot{\mathbf{r}}_{G,I} + \ddot{\mathbf{r}}_{TB,I} + \ddot{\mathbf{r}}_{RP,I} + \ddot{\mathbf{r}}_{T,I}, \tag{2.6}$$

where the first subscript indicates the source of the perturbing acceleration and the second subscript indicates the reference frame in which it is expressed. The perturbations discussed are the aerodynamic perturbations, A, the gravitational and third body perturbations, G and TB respectively. The radiation pressure perturbation, RP, and the propulsive perturbations T.

Perturbations due to dynamic solid tide, relativity, albedo and third body perturbations other than the Sun and the Moon are left out of the investigation entirely, based on Ref. [21].

2.5.1. Aerodynamic

The NRLMSISE-00 atmosphere is used as atmospheric model providing the air density used for the calculation of the aerodynamic drag of the satellite [25]. The model extends from the Earth's surface until 2000 km altitude, well within the LEO orbits analyzed in this research [25]. The uncertainty for the density calculation of NRLSMISE-00 was found to be log-normally distributed with $\mu^* = 0.98$ and $\sigma^* = 1.31$ [12] . The model requires date, geodetic coordinates, local solar time, magnetic index, and the 10.7 cm solar radiation flux index as input [25]. Furthermore, the model is available in Tudat, where these parameters are obtained from the current state of the satellite, the solar radiation flux index is obtained from Ref. [26]. The coverage of the complete region from the surface of the Earth to 2000 km, the known accuracy, and its availability make this model suited for this research.

The density obtained from this model is used to calculate the aerodynamic accelerations. These are given by[18]:

$$\ddot{\mathbf{r}}_{A,A} = -\frac{1}{m}\begin{bmatrix} D \\ S \\ L \end{bmatrix} = -\frac{1}{m}\begin{bmatrix} C_D q A_r \\ C_S q A_r \\ C_L q A_r \end{bmatrix}, \tag{2.7}$$

where D, S, and L are the drag, side, and lift force respectively, C_D, C_S, and C_L the dimensionless coefficients for the forces. Furthermore, $q = \frac{1}{2}\rho v_A^2$ is the dynamic pressure where ρ is the atmospheric density which can be found from the NRLMSISE-00 atmospheric model discussed above and v_A the speed in the aerodynamic frame A, which is, by assuming no wind, equal to the velocity of the satellite in the rotating planetocentric reference frame R as discussed in Section 2.1. Finally, A_r is the aerodynamic reference area. In this research only drag is considered as aerodynamic perturbation. Therefore $C_S = C_L = 0$ and Eq. (2.7) is rewritten to include the ballistic coefficient[19]:

$$\ddot{\mathbf{r}}_{A,A} = -Kq\begin{bmatrix} 1 \\ 0 \\ 0 \end{bmatrix}, \tag{2.8}$$

where

$$K = \frac{C_D A_r}{m}.$$

The aerodynamic perturbing acceleration is subsequently transformed to the body frame B and to the inertial frame I with Eq. (2.1).

2.5.2. Gravitational

The gravitational potential of the Earth can be written as[21]:

$$U = \frac{\mu}{r} \sum_{n=0}^{\infty} \sum_{m=0}^{n} \left(\frac{R}{r}\right)^n P_{nm}(\sin\delta)\left(C_{nm}\cos m\tau + S_{nm}\sin m\tau\right), \tag{2.9}$$

where μ the gravitational parameter of the Earth, R the mean equatorial radius of the Earth, and r the distance between the center of mass of the central body and the satellite. Furthermore, P_{nm} is the associated Legendre polynomial of degree n and order m. τ is the geocentric longitude, and δ the geocentric latitude. And finally, coefficients C_{nm} and S_{nm} are given as[21]:

$$C_{nm} = \frac{2-\delta_{0m}}{M}\frac{(n-m)!}{(n+m)!}\int \frac{s^n}{R^n} P_{nm}(\sin\delta')\cos(m\tau')\rho(\mathbf{s})d^3\mathbf{s}\mathrm{d}m, \tag{2.10}$$

$$S_{nm} = \frac{2-\delta_{0m}}{M}\frac{(n-m)!}{(n+m)!}\int \frac{s^n}{R^n} P_{nm}(\sin\delta')\sin(m\tau')\rho(\mathbf{s})d^3\mathbf{s}\mathrm{d}m, \tag{2.11}$$

where $\delta_{0m} = 1$ for $m = 0$ and $\delta_{0m} = 0$ for $m \neq 0$, M is the mass of the celestial body, τ' and δ' indicate the geocentric longitude and latitude of individual mass element dm respectively. Furthermore, $\mathbf{s}$ is the distance to an individual mass element dm inside the Earth. These coefficients describe the internal mass distribution of the Earth. These coefficients cover a large range of magnitudes, and can give rise to truncation errors during simulations. Therefore, these coefficients are normalized as[21]:

$$\begin{bmatrix}\bar{C}_{nm}\\ \bar{S}_{nm}\end{bmatrix} = \sqrt{\frac{(n+m)!}{(2-\delta_{0m})(2n+1)(n-m)!}}\begin{bmatrix}C_{nm}\\ S_{nm}\end{bmatrix}, \tag{2.12}$$

$$\bar{P}_{nm} = \sqrt{\frac{(2-\delta_{0m})(2n+1)(n-m)!}{(n+m)!}}P_{nm}. \tag{2.13}$$

The gravitational accelerations on the satellite in the inertial planetocentric reference frame I can then be found by substituting $\mathbf{r}$, Eqs. (2.12) and (2.13) in Eq. (2.9)[21]:

$$\ddot{\mathbf{r}}_{G,R} = \nabla U \tag{2.14}$$

In this research the coefficients are obtained from the EGM96 gravitational model [27]. This set is already implemented in the Tudat repository[2]. In Section 4.3 the required values for n and m are found. Since higher order and degree results in larger computational effort, a trade-off needs to be performed.

The celestial bodies surrounding the Earth also cause a perturbation on the trajectory of the satellite, most notably the Sun and the Moon [21]. The acceleration due to these third bodies can be estimated by approximating the mass of the third body as a point mass. The acceleration in the inertial reference, I, is as:

$$\ddot{\mathbf{r}}_{TB,I} = GM\left(\frac{\mathbf{s}-\mathbf{r}}{|\mathbf{s}-\mathbf{r}|^3} - \frac{\mathbf{s}}{|\mathbf{s}|^3}\right), \tag{2.15}$$

where G is the gravitational constant, $\mathbf{r}$ the Cartesian coordinates of the satellite and $\mathbf{s}$ the Cartesian coordinates of the perturbing body.

[2]Astrodynamics & Space Missions, "TU Delft Astrodynamics Toolbox", `https://github.com/Tudat/tudat` retrieved 26/02/2018

2.5.3. Solar radiation

The radiation of the Sun perturbs the orbit of satellites due to reflection of this radiation on the surface of the satellite. The radiation pressure acting on the satellite is calculated as[21]:

$$P = \frac{\Delta E}{\Delta t}\frac{1}{4\pi r_{SS}^2 c}, \tag{2.16}$$

where $\frac{\Delta E}{\Delta t}$ is the power of the Sun, r_{SS} is the distance between the satellite and the Sun, and c the speed of light. The power of the Sun is assumed constant, the relative position of the Sun with respect to the Earth is obtained from SPICE by providing the local time [28, 29]. For the calculation of the resulting perturbing acceleration a simple cannonball model is used, which approximates the shape of the satellite as a sphere. This is relatively simple to implement, and a higher fidelity model is only required if this perturbation is significant compared to the other perturbations as will be investigated in Section 4.3. The accelerations due to the radiation pressure, P, are calculated as [21]:

$$\ddot{\mathbf{r}}_{RP,I} = -PC_R\frac{A_r\hat{\mathbf{r}}_{SS}}{m}, \tag{2.17}$$

where A_r is the reference surface area normal to the Sun-satellite line, and $C_R = 1 + \epsilon$ is the radiation pressure coefficient, where ϵ is the reflectivity of the satellite, $\epsilon = 0$ for full absorption, $\epsilon = 1$ for a fully reflective surface.

2.5.4. Propulsive perturbation

One of the most relevant perturbations in this research is the propulsive perturbation. It is responsible for steering the satellite to the correct state until the thrust is turned off. The thrust is defined in the NTW frame as discussed in Section 2.1, with thrust steering angles for pitch, α and yaw, β, as shown in Fig. 2.1. These steering angles are a function of the costate parameters as will be discussed in Section 2.6. The acceleration due to this thrust is given by Eq. (2.18).

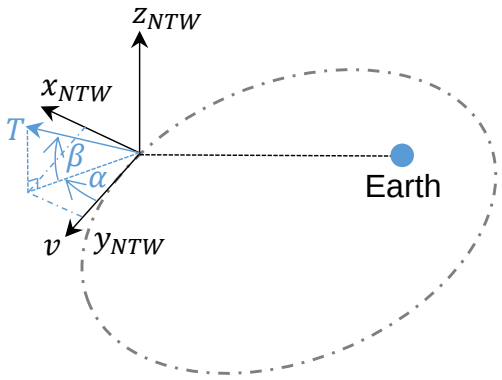

Figure 2.1: Steering angles in the NTW frame.

$$\ddot{\mathbf{r}}_{T,NTW} = \frac{T}{m}\begin{bmatrix}\sin\alpha\cos\beta\\ \cos\alpha\cos\beta\\ \sin\beta\end{bmatrix}, \tag{2.18}$$

where T is the magnitude of the thrust force. The acceleration is given in the NTW frame and is transformed to the I frame using the Eq. (2.1) before inserting it in Eq. (2.6).

The amount of thrust available depends on whether the satellite is in eclipse. A conical shadow model is implemented as described in Ref. [21] to determine whether the satellite is in eclipse. The eclipse situation is presented in Fig. 2.2.

When the satellite is in the umbra region, as indicated in Fig. 2.2, all sunlight is blocked by the Earth and no light is incident on the satellite. Therefore, the satellite is unable to provide thrust. In penumbra region, only part of the sunlight is blocked and there is still some sunlight incident on the

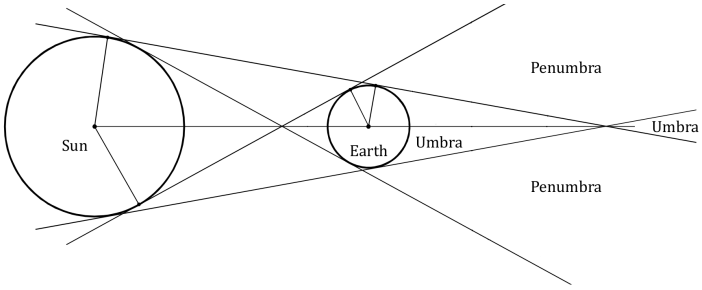

Figure 2.2: Conical shadow model as described in Ref. [21].

satellite. The engines can operate on less power in this region, providing only part of the maximum thrust. The amount of thrust in the penumbra region is found by a shadow function, which is calculated with a simple model of two overlapping circles as seen by the satellite in the penumbra region as shown in Fig. 2.3 [21].

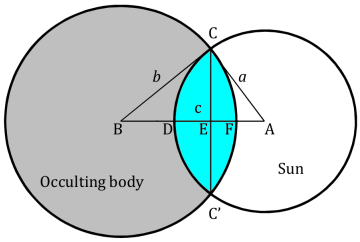

Figure 2.3: Occultation of the Sun by the Earth. Blue region indicates occulted area [21].

where a and b are the apparent radii of the Sun and Earth respectively, c indicates the apparent distance between the Sun and the Earth as seen by the satellite. The shadow function $sf, \in [0, 1]$ indicates the remaining fraction of sunlight and is calculated by[21]:

$$sf = 1 - \frac{A_{oc}}{\pi a^2}, \tag{2.19}$$

where A_{oc} is the occulted area of the Sun by the Earth indicated in blue in Fig. 2.3. The occulted area can be calculated by[21]:

$$A_{oc} = a^2 \cos^{-1}\left(\frac{AE}{a}\right) + b^2 \cos^{-1}\left(\frac{c - AE}{b}\right) - cEC, \tag{2.20}$$

where parameters AE, EC are the lengths as indicated in Fig. 2.3. For a detailed derivation of A_{oc} the interested reader is referred to Ref. [21]. The thrust of the satellite is then scaled as:

$$T^* = sfT. \tag{2.21}$$

This thrust is then substituted in Eq. (2.18).

2.6. Control parameterization

To control the satellite during the disposal maneuver, the direction of the thrust needs to be specified at every moment in time. Defining a flexible thrust profile requires the specification of the thrust direction at many points in time. This results in many parameters to be optimized, increasing the required computational effort of the problem. To reduce the amount of parameters required, the control profile is parameterized by applying the necessary condition from optimal control theory [11]. The advantage of this method compared to specifying the thrust angles at several nodes in time, is that one can define the optimal thrust direction at any point in the orbit with just 5 parameters. For example, the thrust direction for maximum change of the eccentricity is different for all positions along the orbit. Requiring many nodes if the thrust steering angles itself are chosen as control parameters. With the method

used in this research, this can be done with only 5 parameters. The same holds for varying other orbital elements.

The orbits of the considered satellite cases, as will be discussed in Section 4.1, are nearly circular. Therefore, Modified Equinoctial Elements (MEE), as described in Section 2.2, are used to avoid the singularities which would arise when using Keplerian elements, as discussed in Section 2.4. The use of this elements set is advised and used in [22, 30].

The method described below is based on the work of [11, 31–33] where this method for parameterization is successfully developed and applied. Note that this method is not used to solve a two-point boundary-value problem, the method is only used to parameterize the thrust direction in an efficient manner.

The control laws are derived from the Gaussian variational equations for MEE as shown in Eq. (2.5). First, the Hamiltonian for the optimal control problem is defined by[33]:

$$H = \lambda_p \frac{\mathrm{d}p}{\mathrm{d}t} + \lambda_f \frac{\mathrm{d}f}{\mathrm{d}t} + \lambda_g \frac{\mathrm{d}g}{\mathrm{d}t} + \lambda_h \frac{\mathrm{d}h}{\mathrm{d}t} + \lambda_k \frac{\mathrm{d}k}{\mathrm{d}t}, \tag{2.22}$$

where $\lambda\_$ indicate the costates of the different MEE, which can be seen as a weight for the importance of changing that specific MEE. As discussed in Section 2.4, only the first five MEEs are used. The thrust direction of the satellite is modeled with, α and β. To derive the control laws, the variational equations as found in Eq. (2.5) and the acceleration components from Eq. (2.18) are substituted into Eq. (2.22). To clarify the derivation of the control law, all terms without α or β are grouped. This results in the following Hamiltonian[11]:

$$H = (\Lambda_{f1} + \Lambda_{g1}) \sin\alpha \cos\beta + (\Lambda_p + \Lambda_{f2} + \Lambda_{g2}) \cos\alpha \cos\beta + (\Lambda_{f3} + \Lambda_{g3} + \Lambda_h + \Lambda_k) \sin\beta, \tag{2.23}$$

with constants:

$$\Lambda_p = \lambda_p \frac{T}{m}\sqrt{\frac{p}{\mu}}\frac{2p}{w}, \qquad \Lambda_{f1} = \lambda_f \frac{T}{m}\sqrt{\frac{p}{\mu}}\sin l, \qquad \Lambda_{f2} = \lambda_f \frac{T}{m}\sqrt{\frac{p}{\mu}}\frac{((w+1)\cos l + f)}{w},$$

$$\Lambda_{f3} = -\lambda_f \frac{T}{m}\sqrt{\frac{p}{\mu}}\frac{g\,(h\sin l - k\cos l)}{w}, \quad \Lambda_{g1} = -\lambda_g \frac{T}{m}\sqrt{\frac{p}{\mu}}\cos l, \quad \Lambda_{g2} = \lambda_g \frac{T}{m}\sqrt{\frac{p}{\mu}}\frac{((w+1)\sin l + g)}{w},$$

$$\Lambda_{g3} = -\lambda_g \frac{T}{m}\sqrt{\frac{p}{\mu}}\frac{f\,(h\sin l - k\cos l)}{w}, \quad \Lambda_h = \lambda_h \frac{T}{m}\sqrt{\frac{p}{\mu}}\frac{s^2}{2w}\cos l, \quad \Lambda_k = \lambda_k \frac{T}{m}\sqrt{\frac{p}{\mu}}\frac{s^2}{2w}\sin l.$$

The control law for the pitch angle can be found by differentiating the Hamiltonian with respect to α and equating it to zero:

$$\frac{\mathrm{d}H}{\mathrm{d}\alpha} = (\Lambda_{f1} + \Lambda_{g1}) \cos\alpha \cos\beta - (\Lambda_p + \Lambda_{f2} + \Lambda_{g2}) \sin\alpha \cos\beta = 0, \tag{2.24}$$

which can be rewritten to[11]:

$$\tan\alpha = \frac{\Lambda_{f1} + \Lambda_{g1}}{\Lambda_p + \Lambda_{f2} + \Lambda_{g2}}, \tag{2.25}$$

using basic geometry, the following can be obtained.

$$\sin\alpha = \frac{\pm(\Lambda_{f1} + \Lambda_{g1})}{\sqrt{(\Lambda_{f1} + \Lambda_{g1})^2 + (\Lambda_p + \Lambda_{f2} + \Lambda_{g2})^2}}, \tag{2.26}$$

$$\cos\alpha = \frac{\pm(\Lambda_p + \Lambda_{f2} + \Lambda_{g2})}{\sqrt{(\Lambda_{f1} + \Lambda_{g1})^2 + (\Lambda_p + \Lambda_{f2} + \Lambda_{g2})^2}}. \tag{2.27}$$

The sign can be found by checking the Legendre Clebsch condition: $\frac{\mathrm{d}^2 H}{\mathrm{d}\alpha^2} > 0$. This results in the following optimal control law for the pitch angle [11]:

$$\sin\alpha = \frac{-(\Lambda_{f1} + \Lambda_{g1})}{\sqrt{(\Lambda_{f1} + \Lambda_{g1})^2 + (\Lambda_p + \Lambda_{f2} + \Lambda_{g2})^2}}, \tag{2.28}$$

$$\cos\alpha = \frac{-(\Lambda_p + \Lambda_{f2} + \Lambda_{g2})}{\sqrt{(\Lambda_{f1} + \Lambda_{g1})^2 + (\Lambda_p + \Lambda_{f2} + \Lambda_{g2})^2}}. \tag{2.29}$$

A similar approach can be followed to obtain the optimal control law for the yaw steering angle β. The resulting control law is given by[11]:

$$\sin\beta = \frac{-(\Lambda_{f3} + \Lambda_{g3} + \Lambda_h + \Lambda_k)}{\sqrt{(\Lambda_{f3} + \Lambda_{g3} + \Lambda_h + \Lambda_k)^2 + \left((\Lambda_{f1} + \Lambda_{g1})\sin\alpha + (\Lambda_p + \Lambda_{f2} + \Lambda_{g2})\cos\alpha\right)^2}}, \tag{2.30}$$

$$\cos\beta = \frac{-\left((\Lambda_{f1} + \Lambda_{g1})\sin\alpha + (\Lambda_p + \Lambda_{f2} + \Lambda_{g2})\cos\alpha\right)}{\sqrt{(\Lambda_{f3} + \Lambda_{g3} + \Lambda_h + \Lambda_k)^2 + \left((\Lambda_{f1} + \Lambda_{g1})\sin\alpha + (\Lambda_p + \Lambda_{f2} + \Lambda_{g2})\cos\alpha\right)^2}}. \tag{2.31}$$

The values for $\cos\alpha$, $\sin\alpha$, $\cos\beta$ and $\sin\beta$ can be inserted into the propulsive perturbation as shown in Eq. (2.18). In this research the values for the costates are varied during the disposal maneuver by defining the costates at two points in time and linearly interpolate in between. This has been done to gain the flexibility of the optimizer to first focus on e.g. inclination changes which are most efficient at high altitudes, and then focus on decreasing the semi-major axis of the satellite to eventually impact on the surface of the Earth.

3

Numerical methods

This chapter contains the relevant numerical methods used in this research. First, the implemented integrator is discussed in Section 3.1, as the this has a large effect on the precision of the simulations and the required computational effort. Next, in Section 3.2 the implemented optimization technique is discussed. Here, the classical differential algorithm is discussed, after which this technique is advanced with a self-adaptive version of the algorithm, which removes the need for tuning the parameters that are used. Furthermore, the Kernel Density Estimation (KDE) is discussed in Section 3.3. This method is required to create the impact probability functions used to obtain the casualty risk. Finally, the calculation of this casualty risk is described in Section 3.4.

3.1. Integrator

During the first phase of the disposal maneuver, as discussed in Chapter 1, only small perturbations are encountered for which large steps can be taken in the integration. But, when the altitude of the satellite decreases, the perturbations on the satellite increase and smaller steps are required for the integration of the satellite. To limit the computational effort, care must be taken for the selection of the employed integrator. Employing a fixed step size integrator would either result in large computational effort, when a small step size is selected to account for the perturbations in the last part of the entry, or it would result in large errors at a later stage during the de-orbit maneuver when a large step size is selected. Therefore, this is not a viable option for this thesis. Variable step size integrators use the differences between methods of neighboring order to estimate the truncation error. Based on this error, the step size is adjusted to reduce the computational effort while restricting the error made within set tolerance. Examples of such variable step size integrators are the Runge-Kutta-Fehlberg (RK), Bulirsch-Stoer (BS), Dormand and Prince (DOPRI), and Adams-Bashforth-Moulton(ABM) integrators [21, 34, 35]. Figure 3.1 shows the maximum position error for the different integrator methods over 1 week of propagation time plotted against the number of function evaluations [36]. This gives information about the computational efficiency of the different methods available.

In Fig. 3.1 it can be seen that the RK7(8) integrator reaches higher accuracies for similar number of function evaluations compared to the lower order Runge-Kutta integrators. Both the ABM methods and BS methods perform better than the RK integrators. However, these methods were not implemented in Tudat at the start of this research. Therefore, the RK7(8) integrator is used in this work. For future work it is recommended to consider using a different integrator to decrease the computational effort. Figure 3.2 shows the position error over time for different tolerances for the RK7(8) integrator, this figure is used for the selection of the tolerance used in the simulations.

The de-orbit maneuver takes 2 to 3 months with the satellite characteristics as will be described in Section 4.1, the build-up of error needs to be limited to reasonable values during this period. Errors in the order of a few kilometer are assumed reasonable for this research, since the position influence of the thrust over the course of 3 months is much larger as will be shown in Section 4.3. Errors in the trajectory of this research can therefore be compensated by the guidance navigation and control (GNC) system of the satellite during the de-orbit maneuver. Furthermore, the impact track, as will be discussed in Section 4.5, has a length of thousand of kilometers and a width of 100 km, this makes

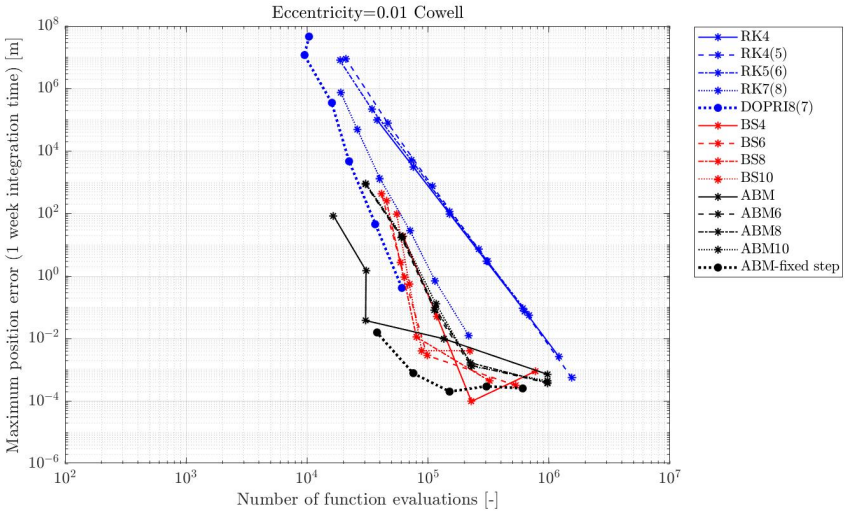

Figure 3.1: Integrator comparison, maximum position error after one week of integration for different amount of function evaluations for different integration methods [36].

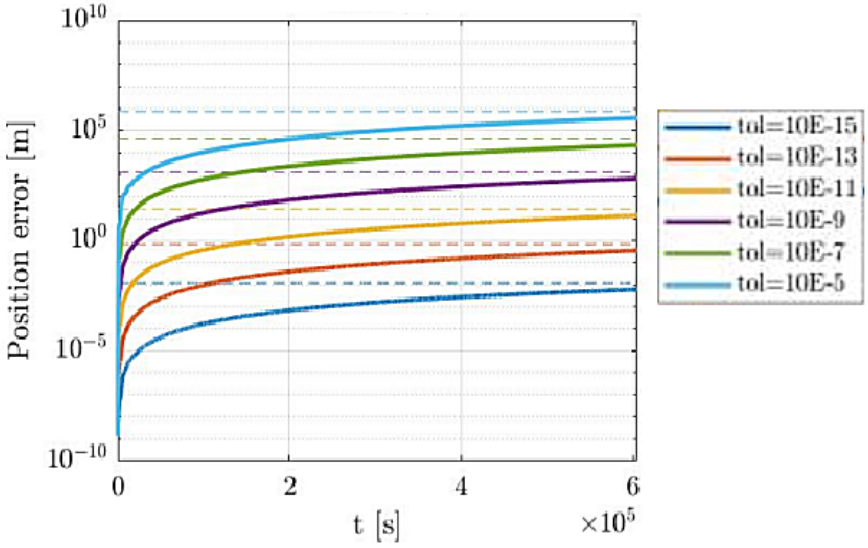

Figure 3.2: Integrator settings comparison, absolute position errors for the different tolerance settings of Runge-Kutta-Fehlberg7(8) integrator[36].

errors of a few kilometer irrelevant for this research. Following the asymptotic behavior observed in Fig. 3.2 to 3 months resulted in a tolerance of 10^{-10} for the RK7(8) integrator used in this thesis. For this tolerance setting errors in the order of 10^3 m are present. To verify the feasibility of the semi-controlled de-orbit strategy, higher accuracies are not required and will increase the computational effort of the simulations.

3.2. Differential evolution

The optimization problem in this research cannot be solved using calculus based approaches, because of the complex population distribution on Earth, and the non-normal impact probability distribution resulting from the uncertainty of the atmospheric and satellite parameters. Therefore, a global optimization method has to be applied. Promising methods to solve global optimization problems are meta-heuristic methods such as Particle Swarm Optimization (PSO), Genetic Algorithms (EA), and Differential Evolution (DE) [37–39]. The advantage of such techniques is that they only require in-

formation about the objective of the optimization, therefore removing the need for differentiability and continuity of the optimization problem [39]. This makes the algorithms suitable for a large range of problems. The methods are increasingly popular for early stage low-thrust transfer trajectory optimization [40–43]. The differential evolution method has been selected for this research, since previous work in low-thrust trajectory optimization employing control parameterization showed good results for this method [32, 33, 44]. However, the classic differential evolution (DE) employed in previous research requires tuning of crossover and mutation parameters which could be a time-consuming task [45]. This has been solved by the development of the self-adaptive differential evolution algorithm jDE, which removes the need of tuning the parameters for the crossover and mutation parameters [46]. The classic DE algorithms, as well as the jDE algorithms are both available in ESA's Parallel Global Multi-objective Optimizer (PaGMO) and are easy to integrate within the code in this research. PaGMO does contain many other optimization algorithms, but the DE is selected because of its heritage in low-thrust optimization in combination with Tudat as discussed in Refs. [32, 33] and due to its simple implementation [32].

In Section 3.2.1 the classic DE algorithm is explained. It gives an overview of the parameters used by the algorithm, the initialization of the population, and the mutation and crossover of genes inside this population. Then in Section 3.2.2 the classic DE algorithm is extended by implementing self-adaptive parameters as developed in Ref. [46].

3.2.1. Classic differential evolution

A graphical representation of the DE algorithm is shown in Fig. 3.3. The first step is to create a population with possible candidates for the solution of the optimization problem. This population has size NP and the individuals $\mathbf{X}_{i,G}$ are parameter vectors of length D. The parameters of the individuals are randomly initialized for the first generation, $G = 1$, after which the population is evolved every generation. The evolution is performed by taking the weighted difference between two random selected individuals $\mathbf{X}_{r2,G}$ and $\mathbf{X}_{r3,G}$ and adding them to a base vector $\mathbf{X}_{r1,G}$. This results in the mutated vector $\mathbf{V}_{i,G}$. The weight used for the weighted differences is indicated by parameter F. Next, crossover is performed between the mutated vector and a selected target vector $\mathbf{X}_{t,G}$ and the result is called the trial vector $\mathbf{U}_{i,G}$. The number of crossovers is determined by the crossover factor CR and is shown in Fig. 3.4. An objective function then determines whether the trial vector performs better than the target vector. If so, the target vector is replaced by this trial vector in the next generation. These steps are repeated NP times, such that all individuals have the role of the target vector once per generation.

This DE strategy can be described as the DE/rand/1/bin strategy, denoting that the base vector is chosen at random (/rand/), uses single differences for the mutation (/1/) and uses binomial experiments for the crossover of parameters (/bin) between the trial and target parameter vector [39]. Other variants, e.g., use the best individual for the base vector and/or use double weighted differences such as DE/best/1/bin and DE/best/2/bin [47, 48], or use the difference between the best of the current generation and the target vector such as DE/current-to-best/2/bin [47]. In addition, exponential functions are used for the crossover as used in DE/rand/1/exp or DE/rand/2/exp [49]. In this research the DE/rand/2/bin strategy is applied, based on the recommendations in [10]. The size of the population in this research is $NP = 10D$. Values between $5D$ and $10D$ are suggested in [39]. In Refs. [32, 33] lower values are used but based on some small tests these lower values resulted in premature convergence for the problem at hand.

3.2.2. Self-adaptive differential evolution

The problem with any of the strategies in Section 3.2.1 is that, besides the population size NP and the number of generations G, also the parameter for mutation, F, and the crossover rate, CR, need to be selected. These parameters influence the efficiency of the search and the quality of the solution [45, 46]. Tuning these parameters is a time-consuming task. Therefore, jDE algorithm is implemented.

The jDE algorithm adds the parameters F and CR to the optimization parameter vector, $\mathbf{X}_{i,G}$. These parameters are evolved in the optimization, alongside the original parameters. Good performing parameters for F and CR are more likely to produce good offspring and therefore remain in the population.

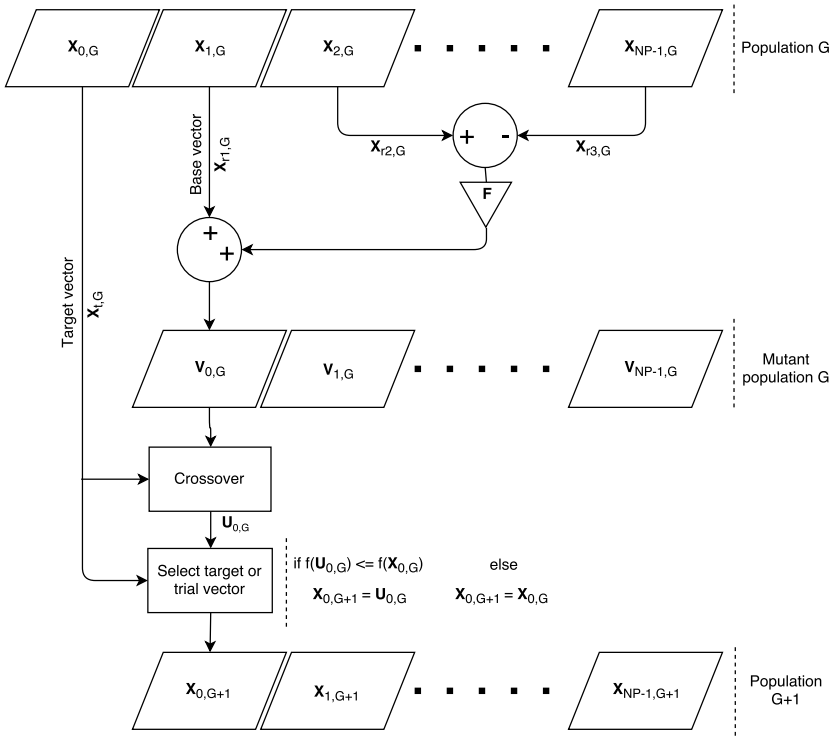

Figure 3.3: Overview of the evolution of the population in the DE algorithm [10].

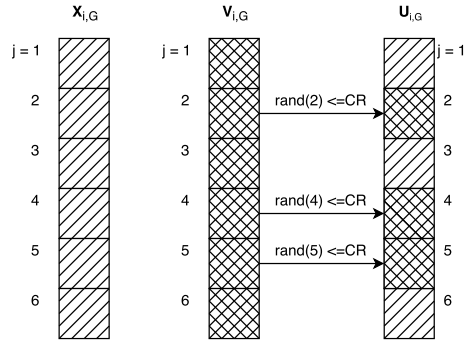

Figure 3.4: Crossover of parameters between the mutated and trial vector in the DE algorithm [33].

The evolution of these parameters is described as[10]:

$$F_{i,G+1} = \begin{cases} F_l + rand(1)F_u, & \text{if } rand(2) < \xi \\ F_{i,G}, & \text{otherwise} \end{cases}, \tag{3.1a}$$

$$CR_{i,G+1} = \begin{cases} rand(3), & \text{if } rand(4) < \xi \\ CR_{i,G}, & \text{otherwise} \end{cases}, \tag{3.1b}$$

where F_l and F_u are the lower and upper bounds for F respectively and set to 0.1 and 0.9 respectively as suggested in [46], ξ is a number indicating the probability of adjusting parameter F or CR, set to 0.1 as suggested in [10]. $rand(i)$ indicates the i^{th} draw from a uniform random distribution $\in [0, 1]$. $F_{i,G+1}$ and $CR_{i,G+1}$ are both obtained before the mutation step as shown in Fig. 3.3, such that they influence the mutation and crossover of generation $(G + 1)$. As the values of F and CR are developed during the optimization alongside the original parameter vector, the optimization is likely to be slower compared to a tuned DE. However, since tuning could be a time-consuming task, longer run times for the final optimization are accepted, as overall, time is saved. The value for NP is set to $10D$ as discussed in Section 3.2.1. If premature convergence occurs, the value for ξ could be adjusted to higher values.

However, the value of 0.1 used in this research, worked for all problems in Ref. [10]. Therefore, varying this parameter has not been investigated in this thesis.

3.3. Kernel density estimation

The results from the Monte Carlo simulation as will be described in Section 4.5 are not resembling known continuous Probability Density Functions (PDF), i.e., uniform, normal, or exponential PDFs. This is the result of a thinner atmosphere near the poles, resulting in different shapes of the PDF depending on the location of re-entry. Therefore, by approximating the distribution with known continuous PDFs, some characteristics of the actual PDF could be missed and errors are introduced in the calculation of the casualty risk. Therefore, the non-parametric method of Kernel Density Estimation (KDE) is used. The KDE approximates the PDF by the summation of multiple PDFs with the mean located at the location of each individual sample. With this method, PDF shapes other than the known continuous PDFs can be constructed from the sample data. The PDF is constructed using[50]:

$$P(t) = \frac{1}{nh}\sum_{i=1}^{n} K\left(\frac{t - t_i}{h}\right), \tag{3.2}$$

where t indicates the independent variable of the impact time, t_i indicates the impact time of sample i, n are the number of samples, h the bandwidth of the kernel determining the smoothness of the resulting function, K indicates the kernel function. In this study, a Gaussian function is used for all samples:

$$K(u) = \frac{1}{\sqrt{2\pi}} e^{\frac{1}{2}u^2}. \tag{3.3}$$

where $u = \frac{t-t_i}{h}$. The smoothness of the KDE is determined by the selected bandwidth, h. Too high values of h causes over-smoothing, thereby not capturing the relevant details of the distribution. For too small values of h, the function is under-smoothed and this the effect of individual samples becomes too large. In Ref. [50] a rule of thumb is presented to determine the value of h, solely based on the sampled data in case a Gaussian kernel is employed. The parameter h is derived from the standard deviation of the data set with[50]:

$$h = \sigma\left(\frac{4}{3n}\right)^{1/5}. \tag{3.4}$$

This method for bandwidth selection is implemented in software packages such as Matlab®[1] and Python [2] and applied in research in Ref. [12]. With this method, a PDF can be constructed per location of re-entry and for different values of the flight path angle at these points as will be discussed in Section 4.5.

3.4. Casualty risk calculation

The variable number of casualties, N, is discrete and finding the probability, P, requires integration over the probability space corresponding to the expected number of casualties ($E = N$). To do so, the underlying discrete probability function for the number of casualties is required, i.e., the probability distribution of having exactly 1, 2, 3, etc, casualties. However, this function is difficult to determine. Therefore, the following method is applied which erases the need of this underlying discrete probability function. In this case the probability of at least one casualty $P(N \geq 1)$ needs to be lower than the limit set in the mitigation guidelines in Ref. [4], which is set to 10^{-4} as discussed in Chapter 1. By applying the Markov's Inequality the underlying discrete probability function is not required. The Markov's inequality gives an upper limit for the probability, P, and relates the casualty risk, P to the expectation, E follows[4]:

$$P(N \geq a) \leq \frac{E}{a}, \tag{3.5}$$

where a is an integer number in this case equal to 1, since the probability of at least 1 casualty is sought for, resulting in:

$$P(N \geq 1) \leq E = N. \tag{3.6}$$

[1]MathWorks, "Kernel Distribution," `https://nl.mathworks.com/help/stats/kernel-distribution.html` retrieved 2/04/2018, 2018

[2]The SciPy community, "scipy.stats.gaussian kde" `goo.gl/1CHmLH` retrieved 2/04/2018, 2016

The casualty risk probability, P, can be approximated by the casualty expectation assuming that N is low. The casualty expectancy is found with Eq. (3.7) [4].

$$E = \sum_{i=1}^{n} \sum_{j=1}^{m} P_{i,j} \rho(\phi_{i,j}, \lambda_{i,j}) A_c, \tag{3.7}$$

where i and j indicate the cross-track, and along-track location indexes of the impact points respectively, where the along-track deviation, as will be found in Section 4.5, is split in n intervals such that the covered along-track distance per impact point (i,j) is lower than the resolution of the population map discussed below, the cross-track deviation is split in m intervals for the same reason, resulting in an impact area with $n \cdot m$ impact points. Furthermore, $P_{i,j}$ is the probability that the satellite crashes in point (i,j), $\rho(\phi_{i,j}, \lambda_{i,j})$ is the population density at point (i,j), and A_c is the casualty area. These parameters are discussed below.

The values for $P_{i,j}$ are obtained by multiplication of the along-track and cross-track probabilities. The along-track PDF is found empirically using a Monte Carlo simulation, by varying the density of the atmosphere and the ballistic coefficient of the satellites as discussed in Section 4.5. The probability $P_{i,j}$ is then found by integrating this distribution over a length Δt in which the impacting satellite covers 2 km of the Earth, justification of this value is discussed below. Drag is the only aerodynamic perturbation considered in this research as will be discussed in Section 4.2. Consequently, no cross-track deviations due to aerodynamic perturbations occur in the simulations. Therefore, the probability in cross-track direction is assumed constant over a range of +/-50 km relative to the unperturbed ground track at 40 km altitude. This assumption was made to account for any cross-track deviations not captured in the simulation. The cross-track probability of each cross-track point j is $\frac{1}{m}$. The value of the cross-track deviation range is based on literature in Ref. [15, 51]. In the last 40 km altitude only limited distance is covered by the satellite as the motion is mostly vertical, as will be discussed in Section 4.4. Therefore, the propagation is stopped at this altitude to reduce the computational effort of the simulation.

The map of population densities for all locations on Earth is obtained from Ref. [14]. The population map has a 12.5 arc-minute resolution. This amounts to 2 km at 85° latitude (highest inhabitated lattitude). Therefore, the size of any of the impact points in the simulations can not be larger than 2x2 km as this would result in skipping of some entries of the population density data. The latest population map of the Earth with exact data is from 2015 and is shown in Fig. 3.5.

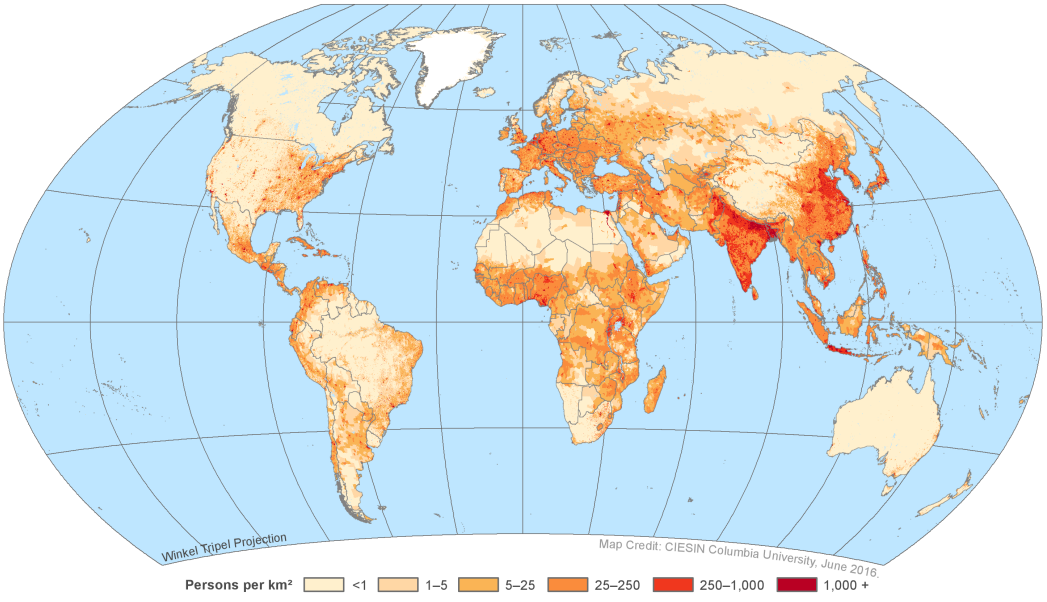

Figure 3.5: Population density Earth 2015 [14].

The casualty area of a surviving fragment of the satellite, $A_{c,k}$, leading to a casualty is given by[4]:

$$A_{c,k} = \left[\sqrt{A_{i,k}} + \sqrt{A_h}\right]^2 \tag{3.8}$$

where $A_{i,k}$ is the projected area of fragment k of the satellite which survived the re-entry and A_h is the cross-section of the average human. A graphical representation of this is shown in Fig. 3.6. The complete casualty area A_c is found by a summation over all u fragments:

$$A_c = \sum_{k=1}^{u} A_{c,k} \tag{3.9}$$

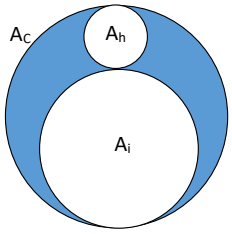

Figure 3.6: Graphical representation of the casualty area.

However, finding the cross-section of the different fragments of the satellite requires detailed re-entry analysis. This analysis includes the simulation of the different components of the satellite and calculating heat-loads and ablation of material. To simplify the calculation of the casualty area, Ref. [4] found a coarse relation between the re-entry mass of the satellite and the resulting casualty area by performing these simulations. The re-entries of multiple satellites from circular orbits have been simulated with high-fidelity models with two debris assessment software tools in Ref. [4]. These simulations split the satellite into multiple fragments of simple shapes such as cylinders, and spheres. These fragments resemble the different components of the satellite and are given dimensions and material properties corresponding to the different satellite components. The outer shapes are ablated during entry because of the encountered heat-load due to the atmosphere, when the outer shapes have been completely burned-up, the inner shapes are released. Again, when these components are burned-up the components inside these shapes are released. The area of the surviving fragments are then inserted into Eq. (3.9). The results of these simulations are shown in Fig. 3.7. The resulting relation for

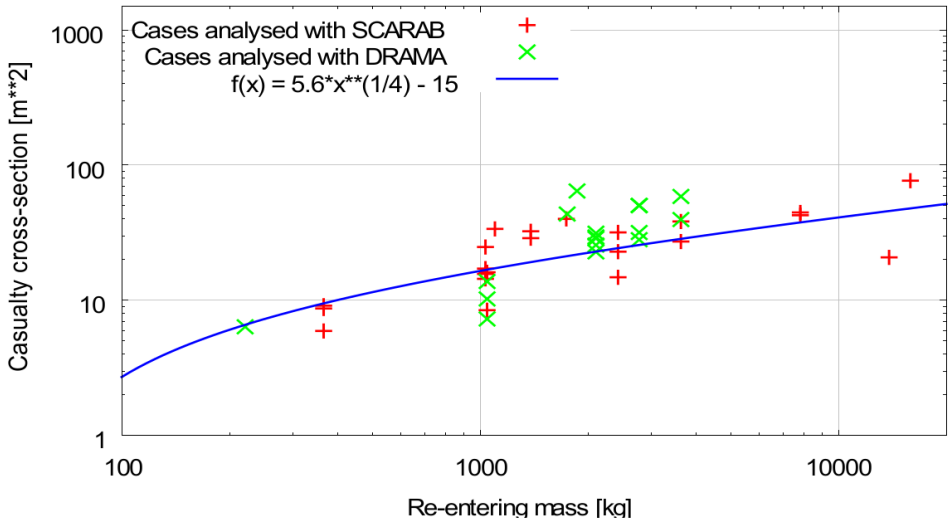

Figure 3.7: Relation between entry mass and casualty area from simulation with two different software tools and high-fidelity models.

the total casualty area was found to be:

$$A_c = 5.6m^{1/4} - 15. \tag{3.10}$$

Since this relation is used in this thesis, some accuracy is lost compared to high-fidelity models. However, this study aims to provide general information about the feasibility of the semi-controlled re-entry strategy. For that purpose, using this relation is extremely relevant. Note that for accurate determination of the risk for specific satellites, this relation is not sufficiently accurate since the risks can be two to three times larger or smaller due to the casualty area as shown in Fig. 3.7.

4

Simulation setup

This chapter gives an overview of the setup of the simulation. First, the cases used in both optimizations, as shortly explained in the introduction, are discussed in Section 4.1. Second, the assumptions made throughout the research are discussed in Section 4.2. Next, in Section 4.3, the perturbations on the satellite, as described in Section 2.5, are analyzed and the relevant perturbations are selected for the optimizations. In Section 4.4, justification is provided for propagating down to 40 km altitude instead of propagating to the ground to reduce the computational effort of the simulation. The impact probability density function, used for the calculation of the risk is treated in Section 4.5. Following this, in Section 4.6 the used control cut-off altitude of 150 km altitude is discussed. Section 4.7 describes the validation of the complete model after all the verification activities, as will be described in Appendix A, are performed. Finally, the setup of both optimization problems are described in Sections 4.8 and 4.9, for the optimization of the complete setup and the last 150 km, respectively.

4.1. Simulation cases

In Ref. [6] relevant cases are found for this research. For the sake of completeness, the parameters are repeated in Table 4.1. For the four cases, satellites in LEO with different masses are considered, which results in different casualty areas, as discussed in Section 3.4. In addition, different ballistic coefficients are considered, which have an effect on the impact PDF as found in Section 4.5. Furthermore, the cases assume different inclinations, which could affect the casualty risk, as the satellite travels more above densely populated areas. The different assumed thrust levels have an effect on the achievable state at 150 km altitude. The orbits are all have an eccentricity of 0.

Table 4.1: Simulation cases used in both optimizations. Same cases as used in [6].

	a [km]	i [deg]	m [kg]	K [m^2/kg]	T [mN]
Case 1: PARASOL	7078	98.28	120	0.01833	8
Case 2: SMOS	7098	98.445	630	0.03515	30
Case 3: SPOT5	7200	98.6	3000	0.015	140
Case 4: SPOT5LIKE	7200	51	3000	0.015	140

4.2. Assumptions

This section sums up the different assumptions made in this research and a justification is provided for each assumption. It is assumed that:

- **The Guidance Navigation and Control (GNC) system of the satellite is perfect down to an altitude of 150 km, after which it is cut-off.** The effect of this assumption is that the state at 150 km altitude is precise, although in reality the satellite will not be able to maneuver the satellite to an exact state at 150 km altitude. This assumption has been made based on previous

research in Ref. [6, 52]. Furthermore, the impact of the thrust from this altitude down to the surface is negligible compared to the effect of the atmosphere as will be described in Section 4.6. Furthermore, from this altitude downwards, the perturbations on the satellite are likely to be too extreme for the GNC to guarantee correct pointing. Therefore, the control is cut-off at this altitude. The impact of this assumption is investigated in Section 6.1.

- **Drag is the only aerodynamic perturbation.** Often the drag is considered the only perturbation for re-entry predictions [13, 51, 53]. As drag is the main contributor for the ground-track dispersion and to reduce the computational effort of the simulation, this is the only aerodynamic perturbation considered.
- **The population density distribution from 2015 is used to calculate the casualty risks.** This is the most recent population density map available with exact data [14]. In Section 6.3, the effect on the risk of future population growth will be assessed. To justify this, note that for the feasibility assessment of the semi-controlled de-orbit strategy, mostly the change in casualty risk compared to the uncontrolled risk is of interest.
- **Three degrees of freedom are considered and the satellite is modeled as a random tumbling sphere.** Previous studies [12, 13] indicated that six degrees of freedom propagation is required for accurate modeling of entries. However, since the effect of the attitude of the satellite is largest for large bodies, such as left-over rocket stages, and the satellites in this thesis are more cube-like satellites, six degrees of freedom propagation is not required for this research [6]. To account for the loss of accuracy of three degrees of freedom propagation, large bounds are used for the ballistic coefficient variations in the Monte Carlo analysis which will be described in Section 4.5. Furthermore, as this thesis wants to provide information about the feasibility of the semi-controlled entry in general, detailed analysis for very specific cases are not of interest here.
- **The impact probability distribution for a flight path angle of 0° at 150 km altitude is used for the calculation of the risk.** This assumption is made to reduce the complexity of the optimization problem. As will be discussed in Section 4.5, different flight path angles have similar effect as changing the true anomaly of the satellite at 150 km altitude, this results in multiple optima with the same resulting impact track on the Earth. The effect of this assumption is investigated in Section 6.1.
- **The thrust of the satellite is directly influenced by eclipses.** No use is made of on-board batteries to continue thrusting during eclipses. Therefore, the amount of available power is directly related to the amount of available thrust. As discussed in Section 2.5.4, a shadow function is used to scale the thrust level according to the amount of input power. Using batteries on-board the satellite could increase the efficiency of the de-orbit maneuver, since energy can be stored and used at the points in orbit where thrusting is most effective. In that case, the satellite can even thrust during eclipse. If the orbit is optimized for minimum fuel mass, the effect of this assumption should be investigated.

4.3. Perturbation analysis

This section describes what perturbations are taken into account during the optimization. Case 1, as described in Section 4.1 is simulated for 1 orbital revolution for radii between 6500 km and 7000 km. The absolute position differences are compared to an reference orbit with only central gravity taken into account are plotted in Fig. 4.1.

The spherical harmonics up to degree and order two are the dominant perturbations in Fig. 4.1 and therefore need to be included in the simulations. The drag is the second most important perturbation for low altitudes. For low altitudes, the contribution of the drag on the deviation is two to three orders of magnitude larger than the contribution of the spherical harmonics of degree and order three to five, third-body perturbations and the radiation pressure. Compared to the inaccuracies in the atmospheric density, as described in Section 2.5.1, where deviations of 10% are not uncommon, the contributions of the spherical harmonics of degree and order three to five, third-body perturbation, and the radiation pressure are not significant.

For larger altitudes, the influence of the thrust is one order of magnitude larger compared to these perturbations. Considering that the inaccuracies in thrust are $\pm 5\%$, the contributions of the spherical harmonics of degree and order three to five, third-body perturbation, and the radiation pressure are not significant for larger altitudes either. The GNC system of the satellite is assumed capable of compen-

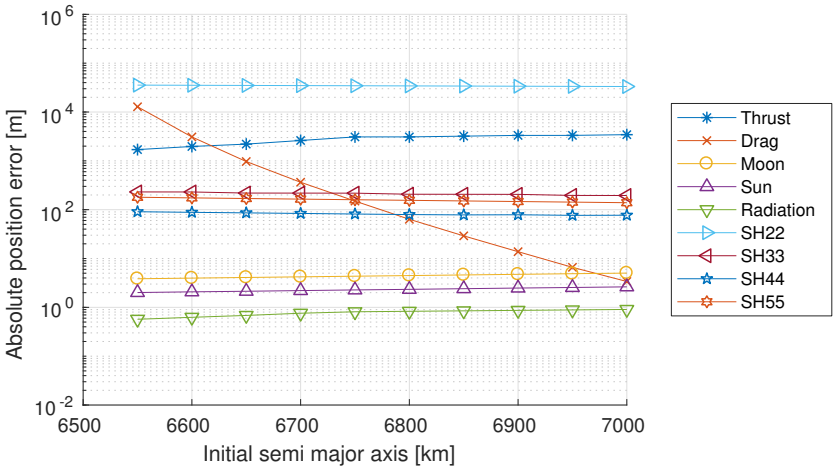

Figure 4.1: Maximum position differences encountered in one orbital revolution. Perturbations are compared to a reference orbit with only central gravity taken into account. $SHnm$ indicate the effect of spherical harmonics up to degree and order n and m, compared to $SH(n-1)(m-1)$.

sating for these smaller perturbations, as discussed in Section 4.2, since these perturbations are only a small portion of the perturbations which could be achieved by the thrust. Finding the exact capabilities of GNC systems for semi-controlled de-orbit strategies is considered out of scope of this research and is left for future work. Another advantage of leaving out spherical harmonics of degree and order three and higher is the reduction of computational effort. A spherical harmonics model with higher degree and order requires the evaluation of many more sinusoids as shown in Eq. (2.9). These sinusoids need to be evaluated at every integration point and therefore it is computational intensive.

Also, the long term effects of the perturbations are analyzed to verify the exclusion of the spherical harmonics of degree and order three to five, third-body perturbations and radiation pressure. The analysis for 10 orbital revolutions are shown in Fig. 4.2.

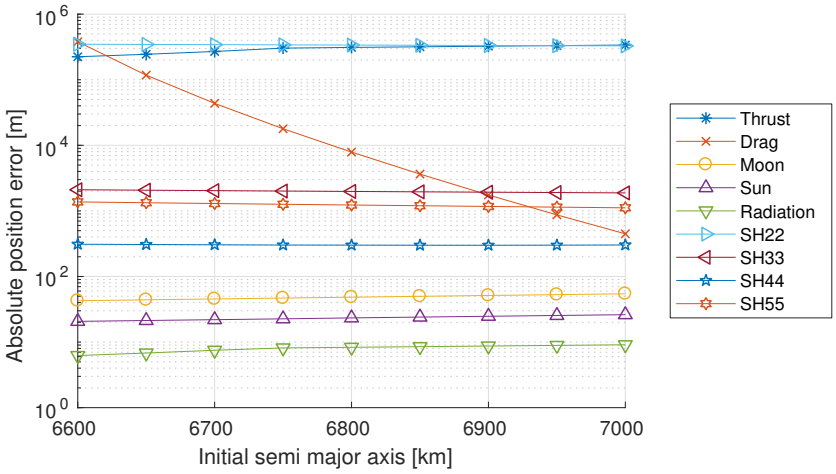

Figure 4.2: Maximum position differences encountered during 10 orbital revolution. Perturbations are compared to a reference orbit with only central gravity taken into account. $SHnm$ indicate the effect of spherical harmonics up to degree and order n and m, compared to $SH(n-1)(m-1)$.

From Fig. 4.2 it was found that for an increase of the simulation time by one order of magnitude, the deviations due to the spherical harmonics, third body perturbations and radiation pressure increase with less than one order of magnitude. This effect is attributed to periodic nature of the other perturbations and the secular nature of the propulsive perturbation. Similar behavior is observed for the aerodynamic perturbation. The findings from the propagation over 10 orbital revolution justify the decision of excluding these perturbations from the optimization.

To summarize this section, the perturbations taken into account in this research are:

- atmospheric drag,
- thrust,
- spherical harmonics up to and including degree and order two.

For the remainder of this thesis, these are the only perturbations considered.

4.4. Propagation termination altitude

As the satellite is propagated down to the surface, the aerodynamic perturbations increase. This reduces the velocity of the satellite which requires a small step size of the integrator, and in turn, large computational effort to keep the deviations within the tolerances. The distance covered in the last part of the re-entry is investigated in Fig. 4.3.

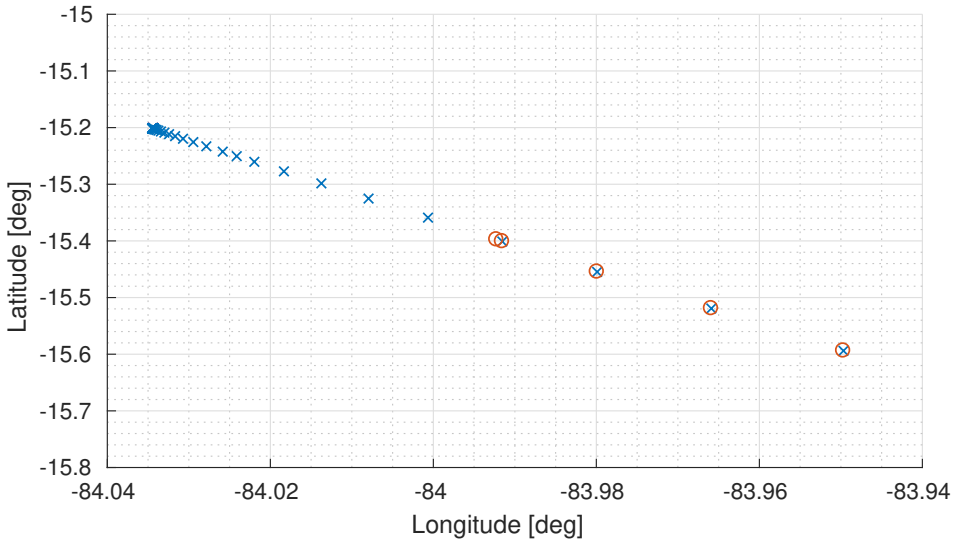

Figure 4.3: Coordinates of last part of entry for PARASOL case with random initial conditions, blue crosses indicate trajectory propagated to 1 km altitude, red circles indicate trajectory to 40 km altitude.

Figure 4.3 shows that the deviation of in the last 40 km of the re-entry is small. Only a difference of $0.04°$ in longitude direction is observed and $0.2°$ in latitude direction for this case. Also, the differences observed are only in along-track direction. The ground distance covered in this last 40 km is approximately 22 km. This is very limited when considering that the impact track length is between $4 \cdot 10^4$ to $1 \cdot 10^5$ km long as will be discussed in Section 4.5. Furthermore, the propagation from 150 km altitude down to 40 km altitude requires 92 steps with the integrator settings as discussed in Section 3.1. For the propagation of the last 40 km, an additional 183 integration steps are required. To verify whether the same behavior is seen for other cases and initial conditions, simulations have been performed for varying initial conditions for all four cases as discussed in Section 4.1. The results are shown in Table 4.2.

Table 4.2: Maximum and average deviations in coordinates and absolute ground distance in the last 40 km of the re-entry. 73 simulations per case are used with equally spaced values for the initial true anomaly.

	average $\Delta\phi$ [deg]	max $\Delta\phi$ [deg]	average $\Delta\lambda$ [deg]	max $\Delta\lambda$ [deg]	average Δd [km]	max Δd [km]
Case 1: PARASOL	0.50	2.0	0.16	0.26	23.8	33.2
Case 2: SMOS	0.056	0.69	0.088	0.14	10.4	17.5
Case 3: SPOT5	0.13	2.0	0.23	0.31	27.3	38.0
Case 4: SPOT5LIKE	0.25	0.46	0.13	0.20	27.1	32.0

Table 4.2 shows larger differences in coordinates compared to the ones found in Fig. 4.3. The maximum values for the coordinate deviations occurred when the satellite impacts at one of the poles, this is expected as the distance covered per degree longitude at the poles is smaller. The resulting along-track distance in the last 40 km is small and in the range between 10 and 40 km. Such variations are small compared to the total length of the impact track. The differences in the number of integration

steps required for the propagation were similar for all simulated cases. The reduction of integration steps and the relatively small differences in the last 40 km justifies the decision for only propagating to 40 km altitude.

4.5. Impact probability distribution

To find the along-track impact PDF, a Monte Carlo simulation with 2000 samples is performed. The satellites as described in Section 4.1, are propagated from circular orbits at 150 km altitude downwards, since at this altitude it is assumed that the controls of the satellites are turned-off as pointed out in Section 4.2 and will be described in more detail in Section 4.6. The satellites are propagated from this initial orbit down to 40 km altitude as discussed in Section 4.4.

In the Monte Carlo simulation a multiplication factor with respect to the baseline value is used to change the density and ballistic coefficient in the simulation. The distribution and corresponding parameters of these multiplication factors are given below.

- Density atmosphere, log-normally, with $\mu* = 0.98$ and $\sigma* = 1.13$.
- Ballistic coefficient, uniformly, with bounds $[0.8, 1.2]$.

The density parameters for the log-normal distribution are obtained from Ref. [12]. The range for the ballistic coefficient is based on the work in Ref. [13]. Smaller bounds are only recommended for high-fidelity six degrees of freedom propagation [13]. No thrust is considered for the uncontrolled phase of the de-orbit strategy, from 150 km altitude downwards. Therefore, for the Monte Carlo simulation discussed here, the only perturbations are the drag and the spherical harmonics up to degree and order 2. As stated in Section 4.2, it is assumed that the GNC system of the satellites is perfect down to 150 km altitude. Thus, no uncertainties are present in the state at 150 km altitude. The impact of this assumption will be investigated in Section 6.1. The PDFs are constructed for different values for the true anomaly, θ, and flight path angle, γ, at 150 km altitude. The impact PDFs for the PARASOL case are shown in Fig. 4.4.

From Fig. 4.4 it can be observed that the results do not follow a normal distribution as was assumed in Ref. [6]. The camel-like shape seen in the results is the effect of the flattening of the Earth. The atmosphere is thinner at the poles at a given distance from the center of mass of the Earth. Therefore a circular orbit makes ”dips” into the atmosphere at the equator. Furthermore, Fig. 4.4 shows that the true anomaly of the re-entry point at 150 km altitude has a large effect on the impact PDF. The true anomaly mostly affects the shape of the distribution and produces minor shifts of the complete distribution as the satellite follows different trajectories relative to the atmosphere, due to the flattening of the Earth.

The effect of the flight path angle is also clearly visible in Fig. 4.4. It can be seen that steeper entry angles result in shorter impact times, this can be seen from the shift of the complete function forward in time. This behavior is attributed to the higher densities encountered by the satellite, since the satellite reaches lower altitudes for steeper entries compared to less steep entries. The shift is also observed in the shift of the nominal trajectory forward in time indicated by the blue and red dash-dotted lines. The large shift observed for $\theta = 120°$ shows that most of the samples crash half an orbit earlier compared to the samples from $\gamma = 0°$. Important to note is that the length of the impact track (3σ-range), remains relatively constant for varying flight path angle. Since the impact track is constructed around the nominal impact point, any shift of the distribution function is accounted for automatically during the propagation to 40 km altitude in the optimizations. Also, it can be seen that the shapes for steeper entry angles show similarities with an increased true anomaly, i.e. the shape of the distribution for $\gamma = -0.1°$ of Fig. 4.4(b) resembles the shape of the Fig. 4.4(c) for $\gamma = 0°$. The same can be observed between Fig. 4.4(d) and Fig. 4.4(f), and between Fig. 4.4(f) and Fig. 4.4(a).

Based on the differences in shape and impact time observed for changing values of the true anomaly, the location of re-entry must be taken into account for the probability distribution during the optimization of the complete strategy and the optimization of the last 150 km.

The variations due to different flight path angles are not taken into account during both optimizations, since varying the value of the flight path angle has a similar effect as varying the true anomaly. This would increase the difficulty of the optimization, since multiple entry locations can achieve the same casualty risk. Since the optimization of the complete de-orbit strategy already requires large computational effort, increasing the complexity is likely to increase this effort even further. For the optimization of the last 150 km, the flight path angle is also set to $0°$. The effect of assuming this circular entry

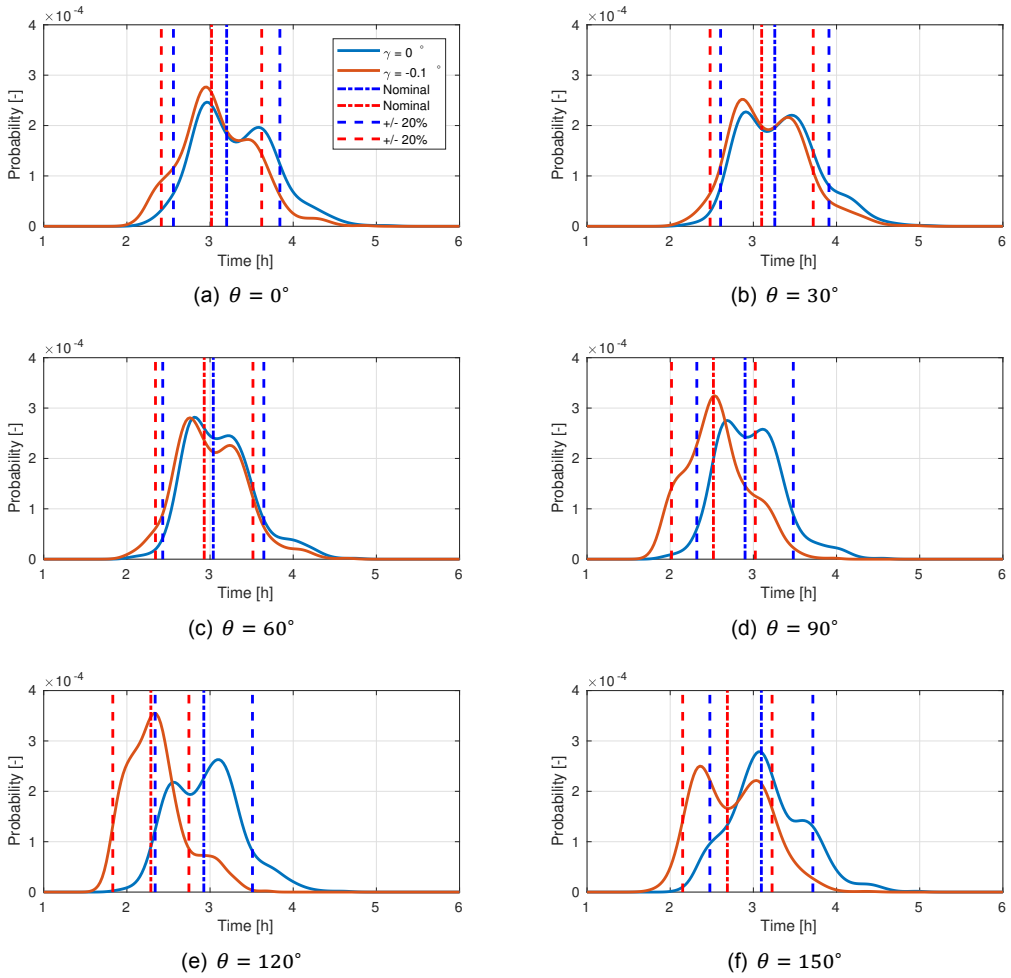

(a) $\theta = 0°$ (b) $\theta = 30°$

(c) $\theta = 60°$ (d) $\theta = 90°$

(e) $\theta = 120°$ (f) $\theta = 150°$

Figure 4.4: Impact probability distributions for PARASOL for different values of true anomaly and flight path angle, time indicates time between 150 km and 40 km altitude

condition is investigated in Section 6.1. Note that any shift of the distribution as shown in Fig. 4.4 is accounted for as the impact track is constructed around the nominal impact point.

The results for true anomalies between 180° and 360° are the same as the ones shown in Fig. 4.4 due to the symmetry of the Earth and its atmosphere. Therefore, these are not shown here as this would be a repetition of what is shown already.

A more detailed view at the distribution of Fig. 4.4(a) is shown in Fig. 4.5.

Figure 4.5 shows that the length of the impact track in this thesis covers a larger range than the range used by the impact predications in Ref. [54]. In Ref. [54] it is assumed that the nominal impact time +/-20% gives the 2σ confidence interval of the impact probability. Similar results were also found in Ref. [13]. From the Monte Carlo analysis in this research, only a 82% confidence interval is reached within the +/-20% bounds. For other values of the true anomaly and flight path angle, confidence intervals between 75% and 88% are found. The lower bound of the +/-20% interval is close to the 2σ lower bound, but the upper bound predicts earlier entries compared to the found PDF and is closer to the 1σ upper bound. Similar results where found for the other values of true anomaly and flight path angle. The longer impact tracks resulting from the described Monte Carlo simulation in this section, compared to the method used in Ref. [54], results in a larger area on the surface of the Earth. For a larger impact area, it is more difficult to only cover uninhabited area. Therefore, the resulting risks are likely to be larger than those calculated with the method described in Ref. [54]. Based on the findings from this Monte Carlo, the casualty risks calculated with the +/-20% bounds in other research, e.g., in Ref. [54] are underestimated.

The above discussion focused on the first case discussed in Section 4.1. However, similar behavior

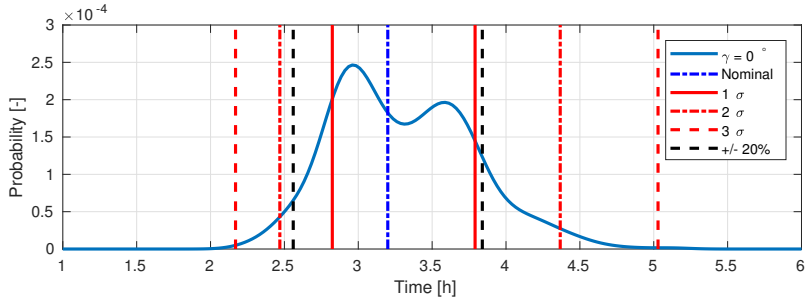

Figure 4.5: Impact PDF PARASOL for $\theta = 0$, $\gamma = 0$

was found for the other cases. The differences are discussed below.

The second case (SMOS), impacts much earlier and also the length of the impact track was found to be shorter. Both observations are expected, since the ballistic coefficient for the SMOS case is much larger. The confidence intervals within +/-20% of the nominal crash time showed values between 80% and 95%. Suggesting that the +/-20% method works better for higher values of ballistic coefficient.

The third case (SPOT5), shows very similar results as the PARASOL case. This is to be expected, since they have similar ballistic coefficients. The results of the last case (SPOT5LIKE) shows similar distributions to the PARASOL case, but the impact times are shifted forward. This can be explained by the lower inclination of the SPOT5LIKE case, which results in smaller variations in altitude caused by the flattening of the Earth. Therefore, the satellite encounters on average higher densities compared to higher inclination orbits.

4.6. Control cut-off altitude

In Section 4.2 the assumption was made that the control of the satellite is cut-off at 150 km altitude. This assumption is necessary because only three degrees of freedom are simulated and only drag is considered. Therefore, torques on the satellite are not known and a cut-off altitude based on encountered torques is not feasible. Furthermore, the satellite parameters required for the assessment of the torques are specific per satellite and this thesis aims to provide general information about the feasibility of the semi-controlled de-orbit strategy, and using such specific parameters reduces the generality of the research.

An initial range for the cut-off altitude is based on literature. The GOCE satellite was functional to altitudes as low as 115 km [52]. It did however switch off its engines at 229 km altitude. The feasibility study for semi-controlled entry performed by CNES used a control cut-off altitude of 150 km [6]. The effect of the control cut-off altitude on the impact time is investigated within the range from 90 km to 250 km altitude. The data is generated by propagation of the satellite cases as discussed in Section 4.1 from a circular orbit at 250 km altitude down to 40 km altitude. The thrust is directed in the direction of the velocity, resulting in maximum deceleration of the satellite. The thrust is cut-off at different altitudes resulting in different impact times. Δt on the y-axis indicates the differences in impact time compared to thrusting down to 90 km altitude.

Figure 4.6 shows differences in impact time in the order of 10^2 s for control cut-off altitudes below 150 km. Thus the influence of the thrust in the last 150 km on the impact time is small. Especially when comparing these numbers to the length of the probability impact track as shown in Section 4.5 which cover a period of several hours. The differences in impact times for higher cut-off altitudes are much larger. In that region the GNC system still has a large influence on the impact time of the satellite. Based on these results, the control cut-off altitude of 150 km is used in the simulation.

For the calculation of the casualty risk of specific satellite cases, for example for future satellites of which all details are known, this altitude assumption should be revisited, and/or an uncertainty in the state at 150 km altitude needs to be implemented after a more detailed analysis of the GNC capabilities in the controlled part of the entry is performed. However, such detailed analysis is out of scope of this research, and is left for future work on this topic.

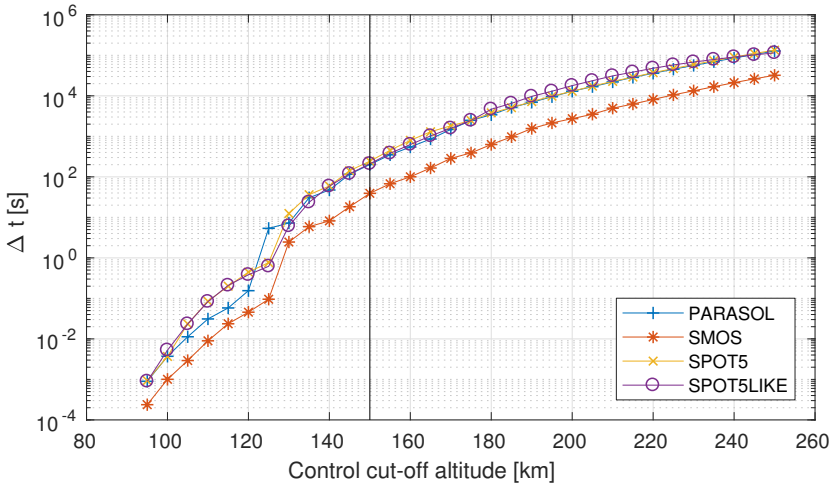

Figure 4.6: Effect of control cut-off altitude on impact time. The results are relative to the impact time for a cut off altitude of 90 km.

4.7. Validation

This section describes the validation of the model. The verification activities can be found in Appendix A and were performed before the validation in this section. These are located in the appendix to improve readability of this chapter. In Appendix A.1 the verification of the control parameterization is discussed. Then, in Appendix A.2, the verification of the entire software chain for the propagation and optimization is performed. Finally in Appendix A.3 the verification of the optimization employing simple population maps is discussed. To validate the complete setup of the simulation, analytical values for the uncontrolled casualty risk, E_{an}, are compared with the uncontrolled risks from simulations, E_{sim} and the values for the uncontrolled casualty risks as found in Ref. [6], E_{CNES}.

The analytical uncontrolled risk is calculated with[4]:

$$E_{an} = \frac{N_i}{A_i} A_c, \tag{4.1}$$

where N_i the total population count between plus and minus the value of the inclination and A_i the area of the slice of sphere between plus and minus the inclination. Note that population above the latitude with the same value as the inclination cannot be hit by debris as the satellite does not cover the area.

The values for the uncontrolled risk from simulations are obtained as follows. For all four cases considered, 200 samples are propagated from an initial altitude of 150 km. The state of each sample is randomly initialized from an uniform distribution. The average of of risks is taken as the value for the uncontrolled risk, E_{sim}. The state has the following bounds:

$$\Delta i \in [-4°, 4°],$$
$$\Omega \in [0°, 360°],$$
$$\theta \in [0°, 360°],$$

where Δi is the difference in inclination with respect to the end-of-life orbit. These bounds will be discussed in Section 4.9

The results of the validation are shown in Table 4.3. $E_{sim,scaled}$ is the uncontrolled risk from the simulations but scaled for population growth to the indicated entry year as this is also done in [6]. Population growth between 2015 and 2040 is expected to be 25% and between 2015 and 2050, 33% [55], thus the risk is increased with these percentages based on the entry year.

Table 4.3 shows good agreement between the analytical uncontrolled risk and the simulated uncontrolled risk. The order of magnitude is correct and the differences are 32% at maximum. Even more interesting is the close approximation with the values found in Ref. [6]. Even though, two completely different methods are used to find the uncontrolled casualty risk, the uncontrolled risks scaled for population growth are well within one order of magnitude from the values in Ref. [6]. For the PARASOL

Table 4.3: Comparison between uncontrolled re-entry risks calculated analytically, by simulations with a random initial state, the simulated risk scaled for population growth, and the risks found in the study performed by CNES in Ref. [6].

	Case 1: PARASOL	Case 2: SMOS	Case 3: SPOT5	Case 4: SPOT5LIKE
$Entry\ year$	2050	2040	2050	2050
E_{an}	$5.1219 \cdot 10^{-5}$	$1.8919 \cdot 10^{-4}$	$3.8347 \cdot 10^{-4}$	$4.7788 \cdot 10^{-4}$
E_{sim}	$3.9095 \cdot 10^{-5}$	$1.6433 \cdot 10^{-4}$	$2.8975 \cdot 10^{-4}$	$4.3280 \cdot 10^{-4}$
E_{an}/E_{sim}	1.31	1.15	1.32	1.10
$E_{sim,scaled}$	$5.1997 \cdot 10^{-5}$	$2.0541 \cdot 10^{-4}$	$3.8536 \cdot 10^{-4}$	$5.7562 \cdot 10^{-4}$
E_{CNES}	$5.20 \cdot 10^{-5}$	$5.26 \cdot 10^{-5}$	$3.11 \cdot 10^{-4}$	$4.59 \cdot 10^{-4}$
$E_{sim,scaled}/E_{CNES}$	1.00	3.91	1.24	1.25

case, exact agreement with the uncontrolled risk in [6] was found. This perfect agreement could be caused by the casualty area, calculated with Eq. (3.10), which has the same values as was found in [6] with high fidelity models. It should be noted that in Ref. [6], the strategy for calculating the risk is different, since a detailed analysis is performed of a fragmented satellite. This includes the calculation of the demise of the different objects. The casualty risk is then based on the left over area and energy per fragment. The largest deviation is found for the SMOS case. This is likely due to the large ballistic coefficient compared to the other considered cases, and the fact that the casualty area in this research is only based on the mass at re-entry, and therefore, does not take aerodynamic properties of the satellite into account.

The close approximation of the simulations with both the analytical solution and the risks, as stated in [6], validate the model used in this thesis. Furthermore, the casualty risks found in this research are consistently overestimated. Therefore, if risks below the limit of 10^{-4} are found, it can be said with high confidence that the actual risk is indeed meeting the requirement.

4.8. Optimization complete de-orbit strategy

This section provides details on the optimization of the complete de-orbit strategy. The objective function for the differential evolution optimization is given by:

$$J = E, \tag{4.2}$$

where E is the casualty expectancy equivalent to the casualty risk as described in Section 3.4. The control parameters are the costates given at two nodes as described in Section 2.6. To find the control profile the costates are linearly interpolated between those nodes. This results in 10 control parameters which are:

$$\mathbf{u} = [\boldsymbol{\lambda}_0, \boldsymbol{\lambda}_1], \tag{4.3}$$

with

$$\boldsymbol{\lambda}_i = \begin{bmatrix} \lambda_{p,i} \\ \lambda_{f,i} \\ \lambda_{g,i} \\ \lambda_{h,i} \\ \lambda_{k,i} \end{bmatrix} \tag{4.4}$$

The optimization is limited to two nodes, because the optimization was already slow for these 10 parameters, increasing the search space even more would further slow it down. The explanation for the bounds for the control parameters can be found in Appendix A and are repeated here alongside the parameters for the differential evolution.

$$\lambda_{p,f,g} \in [-0.1, 0.1], \tag{4.5}$$

$$\lambda_{h,k} \in [-10000, 10000], \tag{4.6}$$

$$jDE = DE/rand/2/bin, \tag{4.7}$$

$$NP = 100, \tag{4.8}$$

$$G = 120, \tag{4.9}$$

$$nodes = 2, \tag{4.10}$$

$$\kappa_x = 10^{-8}, \tag{4.11}$$

$$\kappa_f = 10^{-8}, \tag{4.12}$$

where κ_x is the tolerance for the individuals in the population, indicating minimum difference within the control parameters of the population. Furthermore, κ_f is the tolerance for the fitness in the population, meaning that the optimization is terminated when difference between best and worst individuals in the population is below this threshold. The seed for initializing the population is arbitrarily set to 12345.

4.9. Optimization last 150 km

The optimization from 150 km altitude has the same objective function as the first optimization as given by Eq. (4.2). The control parameters for this optimization are the initial state at 150 km altitude. The eccentricity is set to zero as discussed in Section 4.5, the argument of perigee is set to zero as the eccentricity is zero the location is controlled by varying the true anomaly. The influence of zero eccentricity is investigated in the sensitivity analysis in Section 6.1. The three parameters left are

$$\mathbf{u} = [\Delta i, \Omega, \theta] \tag{4.13}$$

where Δi is the deviation from the baseline inclination as given in Section 4.1. The bounds for the control parameters and parameters for the differential evolution are as follows

$$\Delta i \in [-4°, 4°], \tag{4.14}$$
$$\Omega \in [0°, 360°], \tag{4.15}$$
$$\theta \in [0°, 360°], \tag{4.16}$$
$$NP = 30, \tag{4.17}$$
$$G = 800, \tag{4.18}$$
$$jDE = DE/rand/2/bin, \tag{4.19}$$
$$\kappa_x = 10^{-8}, \tag{4.20}$$
$$\kappa_f = 10^{-8}, \tag{4.21}$$

The bounds for Δi where found by a simulation in which the direction of the thrust is set for maximum inclination change. The satellite is propagated for 3 months to find the minimum and maximum inclination change possible during the controlled part of the de-orbit maneuver. The bounds for Ω and θ cover all possible entry locations at 150 km altitude. Note that a much smaller population for the DE is used for this optimization compared to the optimization of Section 4.8, because less control parameters are used. The seed for initializing the population is arbitrarily set to 12345.

5

Results and discussion

This chapter contains the results of this thesis in which the feasibility of the semi-controlled end-of-life de-orbit strategy is investigated. Chapter 2 provided the necessary dynamical framework for the modeling of the satellites considered in this thesis. The numerical methods in Chapter 3 provided the theory for numerical simulations of the satellites. The simulation setup has been discussed in detail in Chapter 4. Recall that two optimization strategies are employed in this thesis as described in Chapter 1 and Sections 4.8 and 4.9. The first optimization covers the complete semi-controlled end-of-life de-orbit maneuver. Starting at the initial end-of-life orbit the satellite is controlled by defining the direction of the low-thrust propulsion over time. Once the altitude is reached where the attitude of the satellite cannot be guaranteed, the low-thrust propulsion system is turned off and follows a ballistic trajectory towards the surface of the Earth. The second optimization only considers the ballistic part of the trajectory in the last 150 km, since this removes a large portion of the computational effort arising from the controlled phase of the disposal maneuver. The results for the different satellite cases stated in Section 4.1 are presented and discussed one by one in Sections 5.1 to 5.4 respectively. Then a general discussion on the results follows in Section 5.5.

5.1. Case 1: PARASOL

The results for both optimization strategies for the PARASOL case are shown in Fig. 5.1. The satellite parameters for the PARASOL case are described in Section 4.1. Note that the orbit is retro-grade and therefore, the start of the impact track of Fig. 5.1(a) is located in west Africa going upwards. The start of Fig. 5.1(b) is located near Europe and the end of the impact track is located underneath South America. The start of the worst case impact track as shown in Fig. 5.1(c) is located at the bottom of the figure and the end of the impact track is located underneath India.

Both optimizations reduced the risk considerably compared to the uncontrolled case ($3.9095 \cdot 10^{-5}$) as found in Section 4.7. The result of the optimization of the complete setup as shown in Fig. 5.1(a) was found after 71 generations and resulted in casualty risk well below the requirement specified in [1]. The result of the optimization of the last 150 km as shown in Fig. 5.1(b) was found after 79 generations and shows an improved results over the result found in the optimization of the complete setup.

In Fig. 5.1(a) it can be observed that the part of the impact track with the highest impact probability is located near Australia. The largest contributions to the found risk are from the region in west Africa where the population density is high. The contributions of the other two regions indicated are about a third of that in Africa. It interesting to see that the contributions of the region in Papua New Guinea and that of the region east of Papua New Guinea result in a similar contribution to the casualty risk. This is caused by a high population density but low probability in Papua New Guinea, and a low population density but high probability in the other region.

The optimization of the last 150 km provided similar results while reducing the casualty risk one order of magnitude. This is caused by a shift of the impact track in the direction of the end of the impact track due to which west Africa is not covered anymore. As can be seen in Fig. 5.1(b), the inclination of this optimum impact track is closer to 90° as the orbit reaches higher latitudes. The inclination change observed is -3.9° which is close the bound as discussed in Section 4.9. Note that a negative inclination

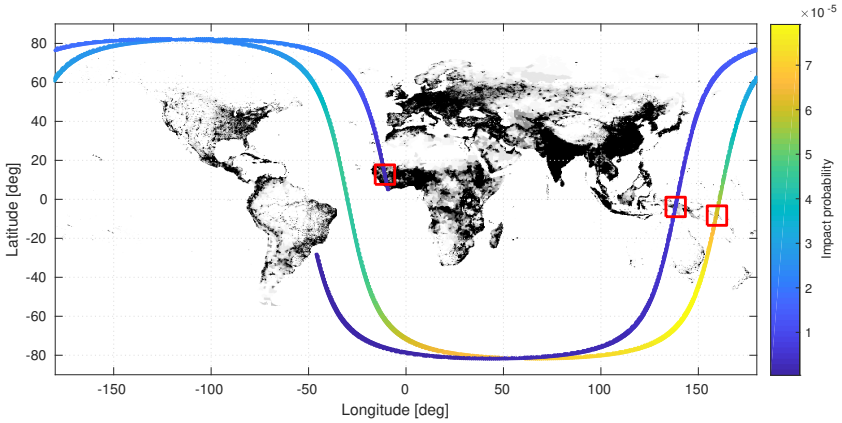

(a) Complete setup. Calculated risk is $2.7321 \cdot 10^{-7}$.

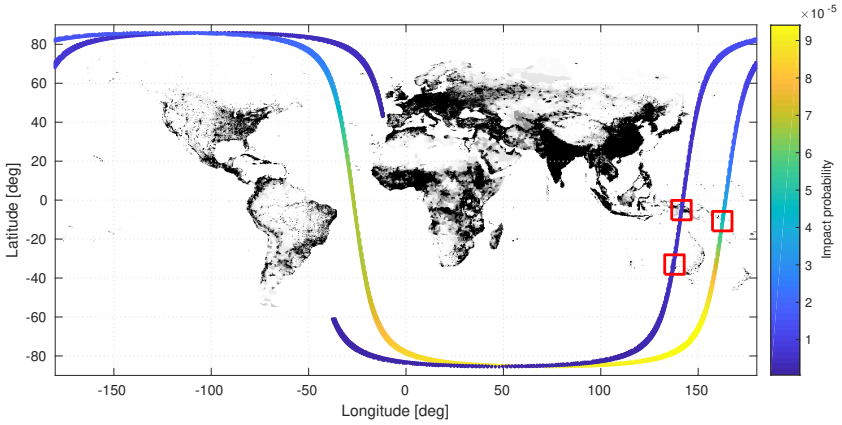

(b) Last 150 km. Calculated risk is $4.4801 \cdot 10^{-8}$.

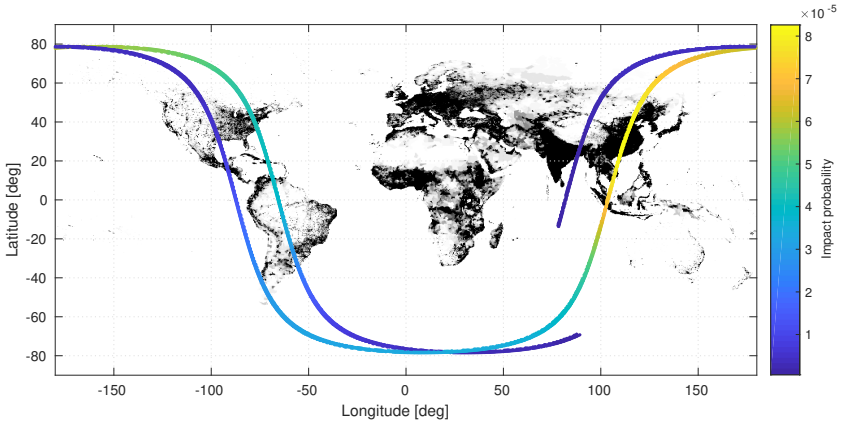

(c) Last 150 km, worst case scenario. Calculated risk is $2.6157 \cdot 10^{-4}$.

Figure 5.1: Optimal impact tracks case 1: PARASOL. The population density is indicated in gray scale, the red squares indicate the areas responsible for the major portion of the casualty risk. Note that the width of impact track is exaggerated.

change results in an orbit reaching higher latitudes. The part of the impact track with highest probability is moved away from Australia. Therefore, the results of the second optimization are expected to be less sensitive to variations in the state at 150 km altitude. The largest contribution to the risk for the optimization of the last 150 km is now located in Papua New Guinea. The second and third largest contributions are from the region in Australia and from the region east of Papua New Guinea.

In Fig. 5.1(c) the impact track and associated risk is shown for an optimization of the last 150 km for maximum casualty risk. This is done as an additional verification of the calculated risks. Several

important observations can be made from Fig. 5.1(c). First, the high impact probability is located above Asia where the population density is high. Second, the inclination is decreased with respect to the end-of-life orbit of the satellite as described in Section 4.1 which is the opposite behavior as found for minimizing the casualty risk. The risk found is 5 times as high as the uncontrolled risk as found in Section 4.7 and it clearly shows the advantage of the semi-controlled disposal strategy as the risks can be reduced dramatically.

The trajectory of the satellite for the optimum of the optimization of the complete setup is shown in Fig. 5.2 together with control profile.

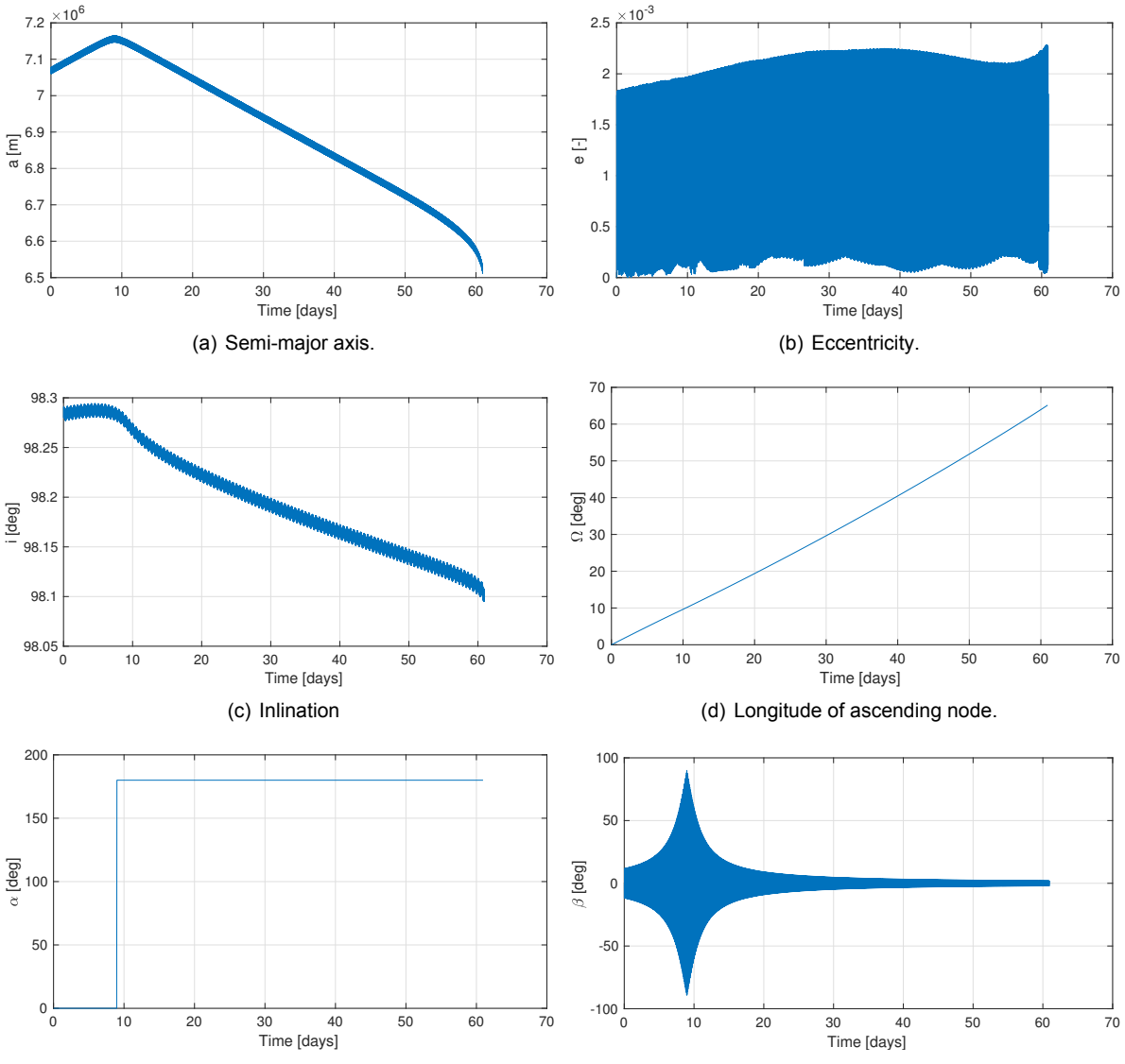

(a) Semi-major axis.

(b) Eccentricity.

(c) Inlination

(d) Longitude of ascending node.

(e) Pitch thrust steering angle.

(f) Yaw thrust steering angle.

Figure 5.2: Optimal low-thrust trajectory case 1: PARASOL down to 150 km altitude, together with optimal thrust profile.

From Fig. 5.2 it can be seen that the transfer down to the 150 km altitude requires 2 months of thrusting. This required 2.8 kg of fuel with the engine properties as discussed in Table 4.1. Figure 5.2(a) clearly shows that the orbit is first increased for 10 days. From this point, the inclination is steady decreased over time as shown in Fig. 5.2(c). Note that the optimum for the optimization from 150 km altitude also decreased its inclination. The increase and decrease of the semi-major axis as shown in Fig. 5.2(a) is also clearly reflected in the thrust profile indicated in Fig. 5.2(e), where the direction of the thrust acceleration is first in the direction of the velocity and after 10 days it is flipped and the thrust acceleration is against the direction of the velocity. The behavior of the inclination corresponds to the

control profile of the yaw angle as shown in Fig. 5.2(f). Note that the yaw angle is adjusted throughout the orbit, since the trajectory covers many orbital revolutions the plot has a solid color. However, general behavior can still be observed from Fig. 5.2(f) After the point where the control for the pitch switches direction, the yaw angle is large, and the effect on the time derivative of the inclination change is clearly visible. Then over time, the yaw angle decreases, which can also be seen in the value for the inclination. The value for the longitude of ascending node is increasing steadily over time due to the J2 perturbation, this behavior is expected for retro-grade orbits. The eccentricity of the orbit remains close to zero for the complete trajectory as shown in Fig. 5.2(b).

5.2. Case 2: SMOS

The results for both optimization strategies for the SMOS case are shown in Fig. 5.3. The satellite parameters for the SMOS case are described in Section 4.1.

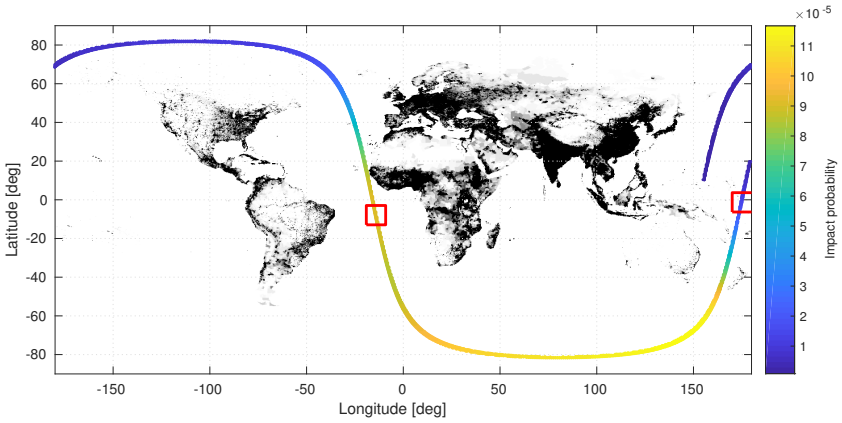

(a) Complete setup. Calculated risk is $1.1962 \cdot 10^{-8}$.

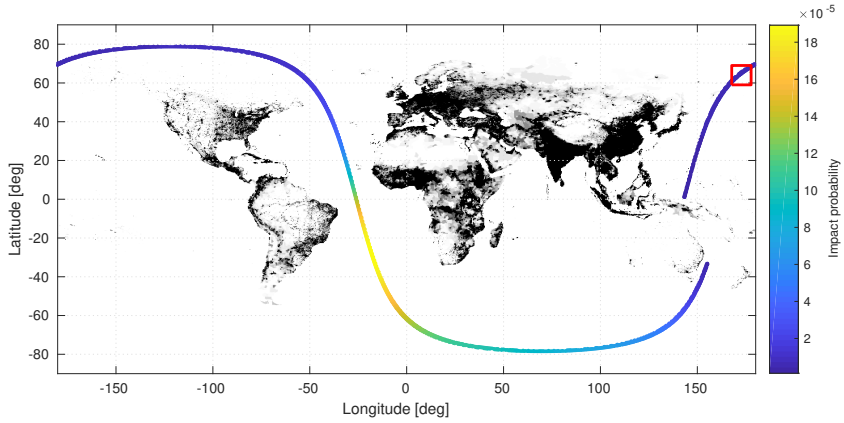

(b) Last 150 km. Calculated risk is $1.6949 \cdot 10^{-9}$.

Figure 5.3: Optimal impact tracks case 2: SMOS. The population density is indicated in gray scale, the red squares indicate the areas responsible for the major portion of the casualty risk. Note that the width of impact track is exaggerated.

Note that the orbit is retro-grade and therefore, the start of the impact track in Fig. 5.3(a) is located at $180°$ longitude going downwards. In Fig. 5.3(b) the start of the impact track is located west of Australia going down and ends just before Papua New Guinea. The risks that are found are very small compared to the uncontrolled case ($1.6433 \cdot 10^{-4}$) as found in Section 4.7. The result of the optimization of the complete setup as shown in Fig. 5.3(a) was found after 117 generations and resulted in casualty risk well below the requirement specified in [1]. The result of the optimization of the last 150 km as shown in Fig. 5.3(b) was found after 111 generations and again shows an improvement over the risk found in Fig. 5.3(a). Figure 5.3 shows the effect of a high ballistic coefficient. The impact track length is decreased significantly with respect to the PARASOL case as shown in Fig. 5.1. As the impact track is shorter, a smaller region is covered and lower casualty risks can be achieved.

In Fig. 5.3(a) it can be observed that the part of the impact track with the highest impact probability is located near Australia comparable with the PARASOL case. The largest contributions to the found risk is from the region to the east of Papua New Guinea where a small region with high population density is located, the probability is relatively low at this point. The second largest contribution to the casualty risk is located in the Atlantic Ocean. Here a small island is located. As the probability of impact is high, this results in a significant contribution to the casualty risk.

The optimization of the last 150 km provided similar results while reducing the casualty risk by an additional order of magnitude. The inclination change observed in Fig. 5.3(b) is 3.2° which is again close to the bound as discussed in Section 4.9. However, for this case, the inclination is increased, resulting in an impact track achieving lower latitudes. In general it is expected that for lower inclinations more inhabitable area is covered, increasing the casualty risk. But, since the impact track is short, the impact track mostly covers oceans resulting in low risks. Also, the part of the impact track with highest probability is shifted towards the Atlantic Ocean, reducing the casualty risks near Australia. Furthermore, the impact track is shifted to the left, such that is nicely located in the middle of the Atlantic Ocean and is expected to be less sensitive to variations of the state at 150 km altitude. The sensitivity will be investigated in Chapter 6.

The trajectory of the SMOS case for the optimum of the optimization of the complete setup shows the same behavior as the PARASOL case shown in Fig. 5.2. Therefore, the figures are not shown here, but can be found in Appendix B. The transfer takes almost 80 days. This is caused by the control profile which increases the altitude of the orbit for a longer period of time. Interesting to note is that the inclination is decreased for the optimization of the complete setup while the inclination for the optimization from 150 km is increased. Since the optimization of the complete setup is more complex, this solution was not found. The transfer required 13.7 kg of fuel with the engine parameters as shown in Table 4.1, which is comparable to the PARASOL case when taking into account to larger dry mass of the satellite.

5.3. Case 3: SPOT5

The SPOT5 case is interesting, as it considers the most massive satellite of all considered cases with a low ballistic coefficient. This results in a long impact track and higher casualty risk as the casualty area is much larger compared to the other cases. The length of the impact track makes targeting of uninhabited area more complex. The satellite parameters are discussed in Section 4.1. The results for both optimization strategies are shown in Fig. 5.4.

Note again, that the orbit is retro-grade and therefore, the start of the impact track in Fig. 5.4(a) is located below Africa going upwards. The start of the impact track for the optimization from 150 km altitude as shown in Fig. 5.4(b) is located in west Africa going upwards. Both optimizations reduced the risk compared to the uncontrolled case ($2.8975 \cdot 10^{-4}$) as found in Section 4.7, a reduction of two orders of magnitude has been achieved. The effect of the long impact track and large mass of the satellite is clearly seen in the results as the possible reductions are much less compared to the other cases. The result of the optimization of the complete setup as shown in Fig. 5.4(a) was found after 114 generations and resulted in casualty risk well below the requirement specified in [1]. The result of the optimization of the last 150 km as shown in Fig. 5.4(b) was found after 702 generations. However, it should be noted that similar results to Fig. 5.1(a) where already found at generation 7 with only a third of the population used during the optimization of the complete setup. The SPOT5 case has a slightly lower ballistic coefficient compared to the PARASOL case, this is directly reflected in the length of the impact track when comparing Fig. 5.4 with Fig. 5.1.

In Fig. 5.4(a) it can be observed that the part of the impact track with the highest impact probability is located near Australia. The findings are similar to that of the PARASOL case. The largest contributions to the found risk are from the region in west Africa where the population density is high. The contributions of the other three regions indicated are about half that of the contribution of west Africa. It interesting to see that the contributions of the regions in Papua New Guinea and Brazil, and that of the region east of Papua New Guinea result in a similar contribution to the casualty risk. This is caused by a high population density but low probability in Papua New Guinea and Brazil, and a low population density but high probability in the other region.

The optimization of the last 150 km provided similar results while reducing the casualty risk even further. The orbit shows large similarities with the optimization of the complete setup. Note that the

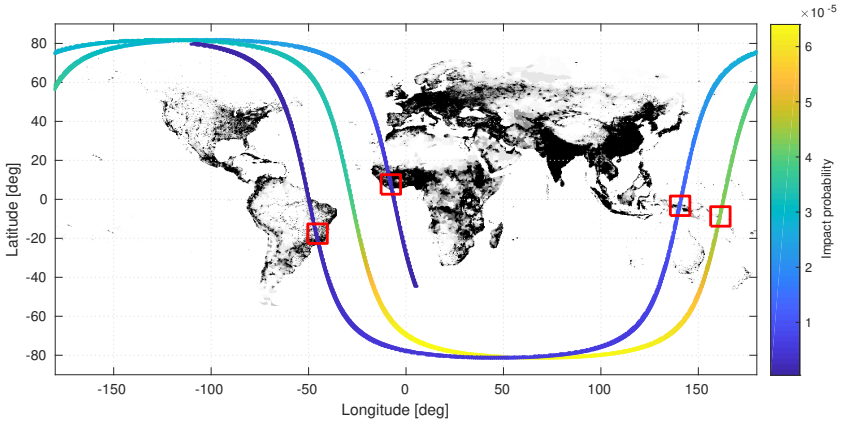

(a) Complete setup. Calculated risk is $5.1685 \cdot 10^{-6}$.

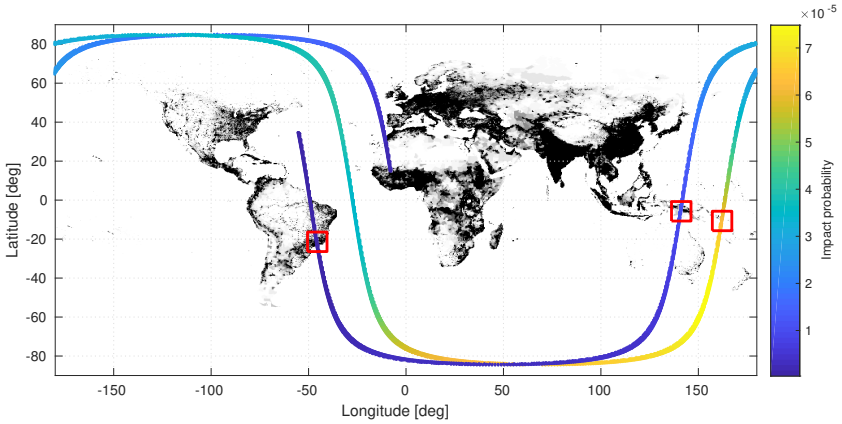

(b) Last 150 km. Calculated risk is $1.3706 \cdot 10^{-6}$.

Figure 5.4: Optimal impact tracks case 3: SPOT5. The population density is indicated in gray scale, the red squares indicate the areas responsible for the major portion of the casualty risk. Note that the width of impact track is exaggerated.

largest difference is the length of the impact track. This is caused by different entry locations between the optima of the complete setup and the optimization of the last 150 km. The track is similar, since the trajectory of the complete setup can have non-zero flight path angles at re-entry. Therefore, the same nominal impact points can be achieved with different re-entry locations. This results in a different impact probability distribution as shown in Section 4.5. The inclination change observed in Fig. 5.4(b) is $-3.2°$ which is again close to the bound as discussed in Section 4.9. Notice that similar behavior for the inclination change is found compared to the PARASOL case in Section 5.1 which also has a long impact track. Also, the part of the impact track with highest probability is shifted towards the Atlantic Ocean, reducing the casualty risks near Australia. Three regions are responsible for the major part of the found casualty risk as shown in Fig. 5.4(b). The regions in Brazil and Papua New Guinea have a high population density but the impact probability is low. The region east of the Papua New Guinea has low population density but high probability.

The trajectory of the SPOT5 case for the optimum of the optimization of the complete setup shows the same behavior as the PARASOL case shown in Fig. 5.2. Therefore, the figures are not shown here, but can be found in Appendix B. The transfer takes over 80 days. This is caused by the lower thrust to mass ratio for the SPOT5 satellite compared to the other cases as described in Table 4.1. The transfer required 68.2 kg of fuel with the engine parameters as shown in Table 4.1. The fuel mass is comparable with the other cases considering the total mass of the satellite.

5.4. Case 4: SPOT5LIKE

This case is the same as the SPOT5 case except it has an inclination of 51° instead of 98.6°. The results for both optimization strategies are shown in Fig. 5.5.

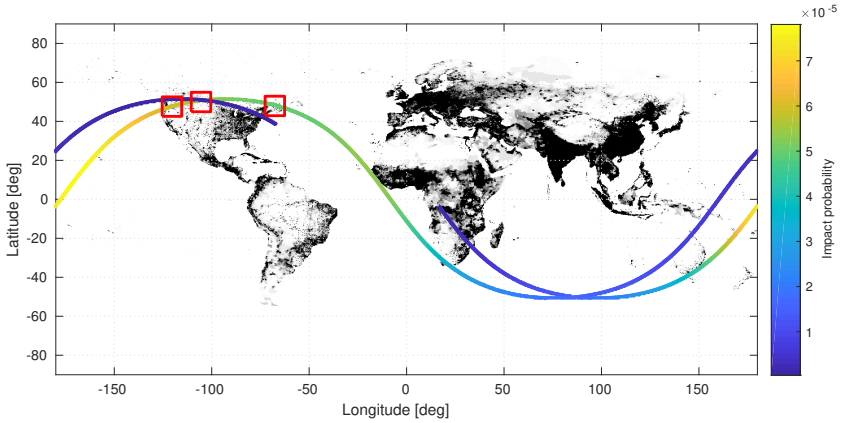

(a) Complete setup. Calculated risk is $2.6802 \cdot 10^{-5}$.

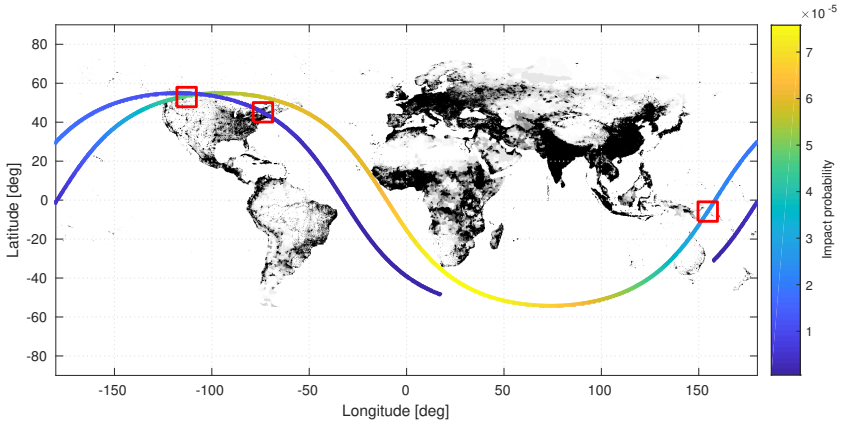

(b) Last 150 km. Calculated risk is $6.4547 \cdot 10^{-6}$.

Figure 5.5: Optimal impact tracks case 4: SPOT5LIKE. The population density is indicated in gray scale, the red squares indicate the areas responsible for the major portion of the casualty risk. Note that the width of impact track is exaggerated.

This time the orbit is pro-grade, so the start of the impact track of Fig. 5.5(a) is located in south of Africa going east. The start of Fig. 5.5(b) is located near Australia also going to the right.

Both optimizations reduced the risk compared to the uncontrolled case ($4.3280 \cdot 10^{-4}$) as found in Section 4.7, a reduction of two orders of magnitude has been achieved. The risks are higher than those found for a higher inclination as discussed in Section 5.3 which indicates the difficulty of finding low casualty risk trajectories for low inclination orbits. However, most orbits in the LEO region are stationed in a sun-synchronous orbit with high inclination [56], for which it is easier to find low risk trajectories. The result of the optimization of the complete setup as shown in Fig. 5.5(a) was found after 84 generations and resulted in casualty risks well below the requirement specified in [1]. The result of the optimization of the last 150 km as shown in Fig. 5.5(b) was found after 628 generations. However, it should be noted that similar results to Fig. 5.1(a) where already found at generation 1 with only a third of the population used during the optimization of the complete setup.

In Fig. 5.5(a) it can be observed that the part of the impact track with the highest impact probability is located in the Pacific Ocean. The value of the risk is almost fully build-up from the contributions in North America where the population densities are relatively high and the probability of impact is also high.

The optimization of the last 150 km provided similar results while reducing the casualty risk even further and is shown in Fig. 5.5(b). Compared to Fig. 5.5(a) the impact track is moved in the direction of the end of the impact track. The result of this is, that the south of Africa is not covered by the impact track, furthermore, the impact probabilities in North America are reduced. The region with the highest contribution to the casualty risk is located in the north west of the United States, followed by the region in the north east of the United States. The inclination change observed in Fig. 5.5(b) is $3.4°$ which is

again close to the bound as discussed in Section 4.9. It is interesting to see that the optimum has a larger inclination compared to the end-of-life orbit as it increases the probability of impacting in North America. It is likely that for lower inclinations the impact track covers Africa which has a high population density. Note that the part of the impact track with highest probability is located very close to Africa, it is expected that the results are much more sensitive to variations in the initial state at 150 km altitude compared to the other cases discussed. The sensitivity for the initial state is investigated in Section 6.1.

The trajectory of the SPOT5LIKE case for the optimum of the optimization of the complete setup shows different behavior for the semi-major axis and eccentricity as shown in Fig. 5.6 with respect to the other cases. The figures for the other relevant Kepler elements and the control profile are similar. Therefore, these figures are not shown here, but can be found in Appendix B.

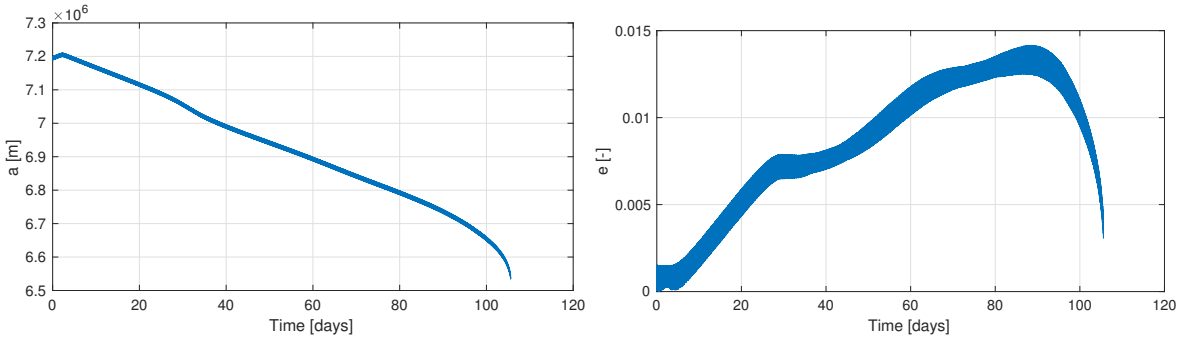

(a) Semi-major axis. (b) Eccentricity.

Figure 5.6: Optimal low-thrust trajectory case 4: SPOT5LIKE down to 150 km altitude

As can be seen in Fig. 5.6(a) the transfer takes over 100 days. This is longer than the SPOT5 case which has the same parameters except for the inclination as shown in Table 4.1. Due to the lower inclination of the SPOT5LIKE case, the satellite is in eclipse more often and cannot thrust continuously. This is also reflected in a reduction of the used fuel mass. The transfer of the SPOT5LIKE case required 58.8 kg of fuel. This is almost 10 kg less than used for the SPOT5 case. Furthermore, note the different behavior of the eccentricity of the satellite shown in Fig. 5.6(b). The eccentricity is increased steadily. The effect of the atmosphere can be clearly seen in the last part of the transfer where the eccentricity is reduced again. This circularization is a known effect caused by the atmosphere as the perigee of the orbit encounters higher drag which reduces the apogee while the perigee is effected to a lesser extend.

5.5. General discussion of results

A summary of the casualty risks for all cases is shown in Table 5.1. Table 5.1 includes the minimal casualty risks for the optimization of the complete setup, the minimal casualty risks for the optimization of the last 150 km, the maximum casualty risks found by optimizing the last 150 km, and the values for uncontrolled casualty risks.

Table 5.1: Summary casualty risk results for both optimizations compared against the risk of uncontrolled entry.

	Case 1: PARASOL	Case 2: SMOS	Case 3: SPOT5	Case 4: SPOT5LIKE
$E_{CS,min}$	$2.7321 \cdot 10^{-7}$	$1.1962 \cdot 10^{-8}$	$5.1684 \cdot 10^{-6}$	$2.6802 \cdot 10^{-5}$
$E_{150km,min}$	$4.4801 \cdot 10^{-8}$	$1.6949 \cdot 10^{-9}$	$1.3706 \cdot 10^{-6}$	$6.4547 \cdot 10^{-6}$
$E_{150km,max}$	$2.6156 \cdot 10^{-4}$	$1.9295 \cdot 10^{-3}$	$1.8634 \cdot 10^{-3}$	$2.6182 \cdot 10^{-3}$
$E_{uncontrolled}$	$3.9095 \cdot 10^{-5}$	$1.6433 \cdot 10^{-4}$	$2.8975 \cdot 10^{-4}$	$4.3280 \cdot 10^{-4}$

All cases considered met the set requirement of $E < 10^{-4}$. In general, large reductions in casualty risks can be achieved by applying a semi-controlled disposal strategy. Note that the casualty risks for the uncontrolled entry is in between the minimum and maximum values for the casualty risks, further strengthening the validation of the casualty risk calculation as described in Section 4.7. Some similarities were found between the different cases. First, the optimal tracks for all cases cover both oceans

where risks are low. Second, Papua New Guinea and Australia are covered by all optimal impact tracks, since it is exactly located on the route over both oceans. In Australia the impact track cover the region with low population density. The effect of the different parameters of the cases discussed in Section 4.1 is also clear. First, the impact of the ballistic coefficient. Lower ballistic coefficients resulted in longer impact tracks, resulting in higher casualty risks. This is because for long impact tracks a shift in along-track direction may decrease the risk at one end of the track, but is likely to increase the risk on the other side. This effect can be seen in Figs. 5.4 and 5.5 where shifting the impact track increases the probability of impact in two of the indicated regions but decreases the probability in the other indicated region(s). Furthermore, the mass of the satellite directly relates to the casualty risk. This is already clear when investigating Eq. (3.10), but is again shown from the results. No clear behavior was found for adjustments to the inclination. Some of the results showed an increase and some a decrease in inclination. The best solution depends the length of the impact track and the initial inclination. This initial inclination does have a clear effect on the casualty risk as shown in Sections 5.3 and 5.4. Inclinations lower than 51° are likely to be problematic, since the track cannot go underneath Africa and over the Unitited States at the same time.

The resulting impact tracks from the optimization of the last 150 km resembled the optima from the optimization of the complete setup. Comparing the states at 150 km altitude did not show similar values. As the simulations in the complete setup have flight path angles which are non-zero, similar nominal impact points can be achieved with large differences in the state at 150 km altitude. During the optimization of the complete setup, some near zero values for the flight path angle at 150 km altitude were found. The low values for the flight path angles are caused by the circulization due to the atmosphere as can be see clearly from Fig. 5.6(b). These findings confirms that the states found in the optimization of the last 150 km can be achieved by a correct thrust profile.

The optimization of the last 150 km was performed, since the optimization of the complete setup was computationally intensive, this is clearly shown when comparing the run times of both optimizations as shown in Table 5.2. Note that the value for the run times for the complete setup, as shown in Table 5.2,

Table 5.2: Overview of run times for the different cases for both optimization strategies. Performed on Intel Xeon processor (type E5-2683 v3.0) with a clock speed of 2.0 GHz

	Case 1: PARASOL	Case 2: SMOS	Case 3: SPOT5	Case 4: SPOT5LIKE
Complete setup	59 h	69 h	77 h	101 h
Last 150 km, average of 5 runs	0.18 h	0.14 h	1.2 h	1.2 h

are based on one run. This is because the run times were too large to run multiple times. The run-times for the optimization from 150 km altitude are much lower and includes larger differences between the cases. The large differences in run-times between the first two cases and the SPOT5 cases are caused by the tolerance settings for the optimization. The risks for the PARASOL and SMOS cases are much lower. Therefore, the population is faster converged since the tolerance is used to check the absolute difference between the worst and best individual in the population.

The behavior of the optimization algorithm is shown in Fig. 5.7 where the best casualty risk per generation is shown for all cases. The behavior of the optimizer for the complete setup is shown in Fig. 5.7(a). This clearly shows the differences in found risks between the first two cases and the SPOT5 cases. The requirement is fulfilled at the first generation. Most improvements of the casualty risks are observed in the first 30 generations. The behavior of the optimization of the last 150 km is shown in Fig. 5.7(b). All cases already found an individual with a risk below the set requirement in generation 1. Most of the reduction in casualty risk is achieved within the first 100 generations. The optimization of the PARASOL and SMOS case both converged well before the generation limit.

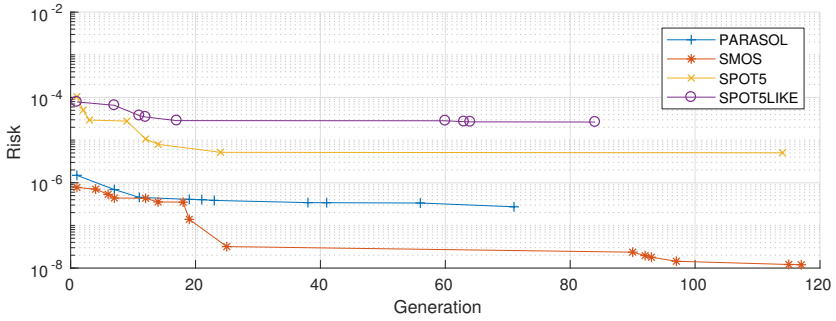

(a) Complete setup.

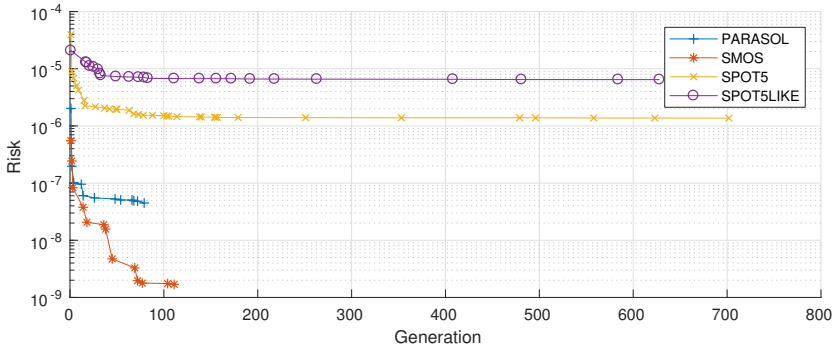

(b) Last 150 km.

Figure 5.7: Best individuals of the jDE algorithm per generation.

6

Sensitivity analysis

This chapter investigates the effect of the assumptions made in Section 4.2 and the decisions made to reduce the computational effort of the optimization in Chapter 4. In Section 6.1, the sensitivity of deviations in initial state at 150 km are investigated. Then, in Section 6.2, the sensitivity of the optimization algorithm to different seeds for the random number generator is investigated. Next, in Section 6.3, the effect of population growth in the future is analyzed. Finally, in Section 6.4 the effect of assuming a normal distribution on the calculated casualty risk is investigated with respect to the KDE PDF employed in this research.

6.1. Exact state at 150 km altitude

To investigate the sensitivity of the assumption of a perfect GNC system down to 150 km altitude, the optimized trajectories from the optimization of the last 150 km in Chapter 5 are perturbed at initial conditions. The longitude of ascending node and the true anomaly of the orbit are varied in the range of [-2°, 2°] and [-10°, 10°] respectively and are compared to the optimized results. These parameters are selected since they cover two important error sources resulting from the controlled part of the disposal strategy. The longitude of ascending node covers the phasing with the Earth, if the satellite arrives a bit later at the correct latitude and altitude, the longitude is decreased. Any errors in the trajectory causing the satellite to enter at a different latitude is captured by varying values of the true anomaly. Furthermore, the effects of these parameters can be clearly related to the impact track figures as shown in Chapter 5, i.e., an increase in values for the true anomaly result in a shift of the impact track in along-track direction and changes to the longitude of ascending node shift the impact track in longitudinal direction. During the controlled part of the disposal strategy, higher deviations in along-track directions are expected compared to the cross-track deviations. Therefore, the true anomaly is varied over a larger range. Furthermore, the flight path angle is varied from 0° to $-0.1°$. The highest flight path angles encountered during the optimization of the complete setup were $-0.06°$, the investigated range is stretched to $-0.1°$ to account for future improvements of the low-thrust propulsion engines which could increase the thrust to mass ratio resulting in steeper entries. These flight path angles were also considered in Section 4.5. The following sections will treat the cases separately, in the same order as before; PARASOL, SMOS, SPOT5, SPOT5LIKE.

6.1.1. Case 1: PARASOL

The results of the sensitivity analysis regarding variations in initial conditions at 150 km altitude, for the PARASOL case are shown in Fig. 6.1. The casualty risks resulting from different initial conditions are indicated by colors ranging from dark blue to yellow corresponding to the magnitude of the casualty risk.

The lowest casualty risks for a flight path angle of zero are found at the center of the sensitivity map as shown in Fig. 6.1(a). This indicates that the optimizer performed well in finding the minimum risk. All considered regions surrounding the optimum have risks well below the requirement that has been set in Ref. [1]. The observed variations are discussed using the baseline impact track as shown in Fig. 5.1(b). The influence of all three parameters is discussed sequentially.

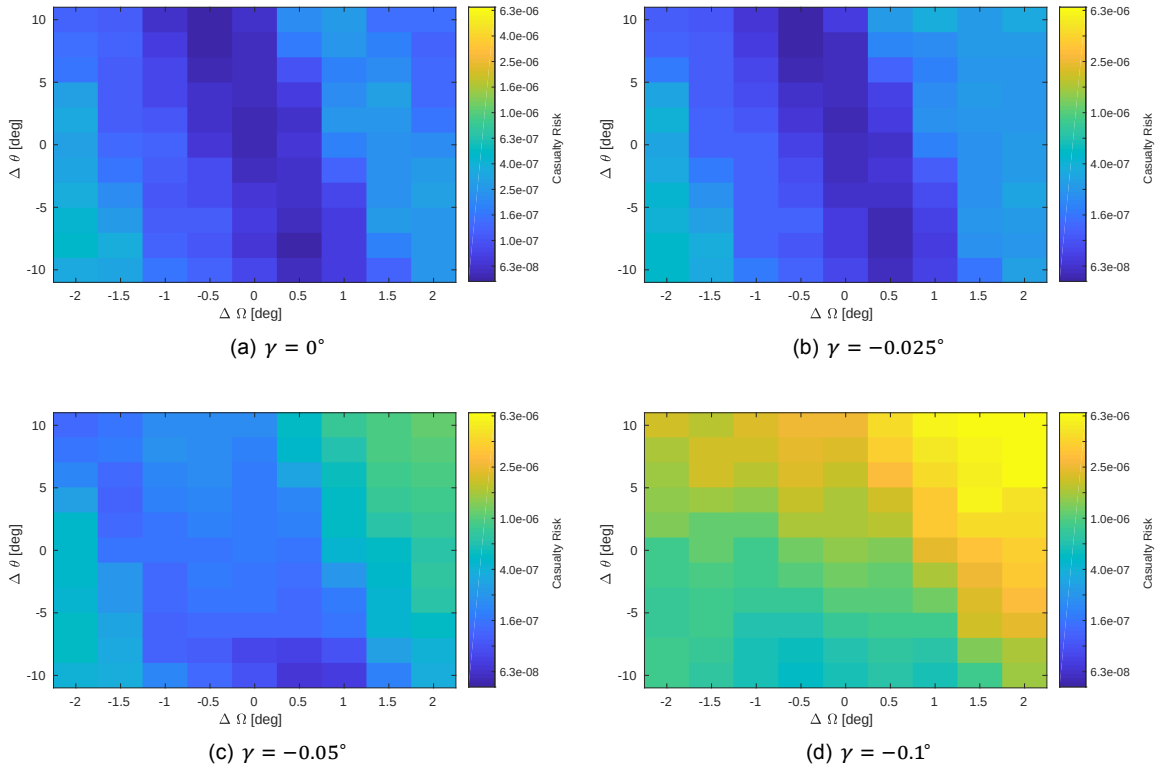

(a) $\gamma = 0^\circ$ (b) $\gamma = -0.025^\circ$

(c) $\gamma = -0.05^\circ$ (d) $\gamma = -0.1^\circ$

Figure 6.1: Sensitivity of the optimal impact track of the PARASOL case to deviations in the state at 150 km.

The increased casualty risk for both negative and positive values for $\Delta\Omega$, are caused by the impact track covering more densely populated areas to the left and right of the impact track in Papua New Guinea. The casualty risk is increased with one order of magnitude within the considered range.

The effect of the differences in the true anomaly are also clearly visible in Fig. 6.1(a). For the found optimum, both negative and positive values for $\Delta\theta$ increase the casualty risk. Shifting the probability function in the direction of the end of the impact track, results in higher casualty risks in Papua New Guinea and Australia, but a decrease in casualty risk at the islands to the east of Papua New Guinea. Shifting the probability function in the direction of the start of the impact track (negative $\Delta\theta$) has the opposite effect. The casualty risks are increased with less than one order of magnitude within the considered range.

Finally, the effect of the flight path angle is large when comparing the differences in casualty risks between Figs. 6.1(a) to 6.1(d). The casualty risk is increased with two orders of magnitude between flight path angles of 0° and -0.1°. Note that an area of high casualty risk arises on the right hand side. This is caused by the earlier impact for steeper entries, which shifts the complete impact track in the direction of the start of the impact track. Steeper entries, dive further into the atmosphere resulting in higher drag and thus a higher deceleration leading to earlier impact. For more negative values of the flight path angle, the impact track covers southern Europe and west Africa. The casualty risk is even further increased when also a longitude shift to the right is present causing the track to cover an even larger portion of Europe.

6.1.2. Case 2: SMOS

The results of the sensitivity analysis regarding variations in initial conditions at 150 km altitude, for the SMOS case are shown in Fig. 6.2. The casualty risks resulting from different initial conditions are indicated by colors ranging from dark blue to yellow corresponding to the magnitude of the casualty risk.

The lowest casualty risks for a flight path angle of zero are found at the center of the sensitivity map as shown in Fig. 6.2(a). This indicates that the optimizer performed well in finding the minimum risk. All

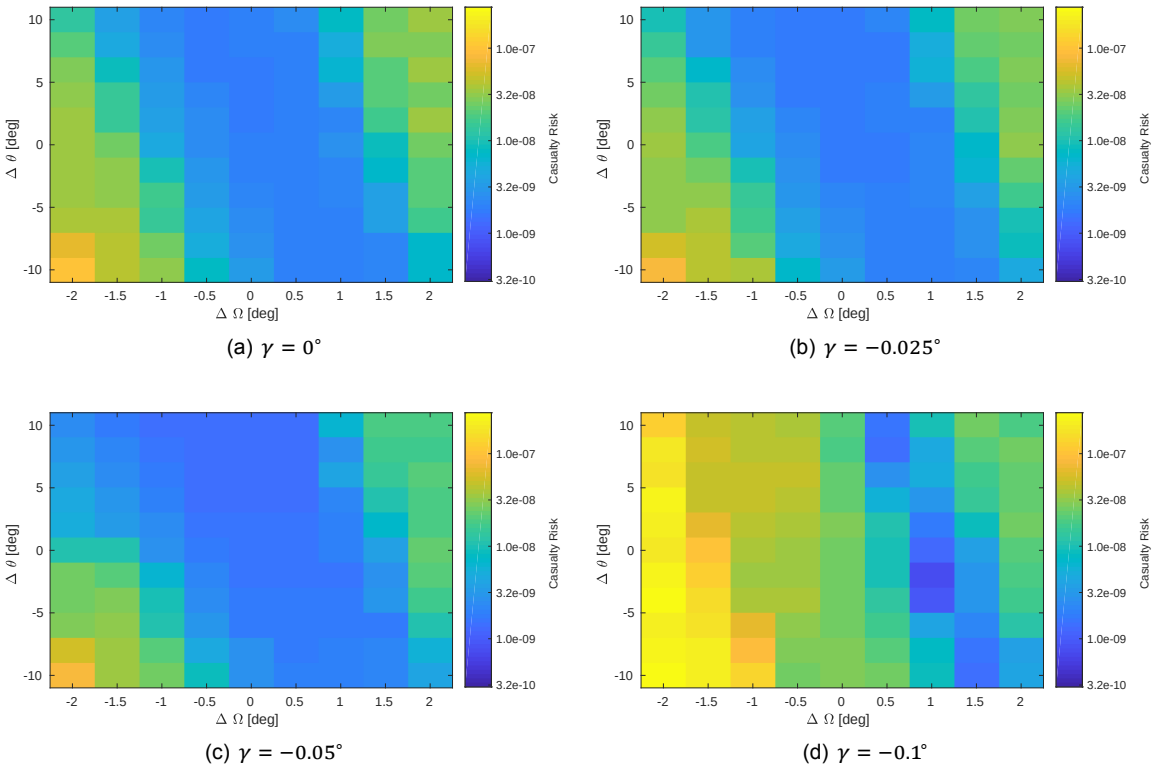

(a) $\gamma = 0°$ (b) $\gamma = -0.025°$

(c) $\gamma = -0.05°$ (d) $\gamma = -0.1°$

Figure 6.2: Sensitivity of the optimal impact track of the SMOS case to deviations in the state at 150 km.

considered regions surrounding the optimum have risks well below the requirement that has been set in Ref. [1]. The sensitivity maps for the SMOS case in Fig. 6.2 are resembling that of the PARASOL case in Fig. 6.1, but the overall casualty risks are one order of magnitude lower.

The casualty risks for the SMOS case are close to zero. Therefore, pointing out where the increased values for the risk originate from is not evident from the figures. The impact track is located such that both to the right and left of the optimal impact track of Fig. 5.3(b) the population density is slightly higher. Also increasing the true anomaly of the satellite increases the casualty risks in the regions at the end of the impact track but decreases the risk at the start of the impact track simultaneously.

The region with the highest risks is located in the lower left of Figs. 6.2(a) to 6.2(d) opposite to the location of the high risk region for the PARASOL case. Note that the trajectory in Fig. 5.3(b) is located close to the coast of Australia. A shift of the impact track to the left causes the impact track to sideswipe the coast of Australia. The effect of small variations in the flight path angle is marginal, the shape of the sensitivity map is similar. For a large difference in flight path angle the resulting risks in the sensitivity map do change. However, all casualty risks are well below the casualty risk requirement set in Ref. [1]. The higher risks in Fig. 6.2(d) are the result of the impact track shifting in the direction of the start of the impact track, this is caused by the steeper entry angles which results in higher probability of impact in Australia which is the main contributer to the casualty risk for the left hand side of the figures in Fig. 6.2.

6.1.3. Case 3: SPOT5

The results of the sensitivity analysis regarding variations in initial conditions at 150 km altitude, for the SPOT5 case are shown inFig. 6.3.

The effect of $\Delta\Omega$ and $\Delta\theta$ are similar to the PARASOL and the SMOS case as shown in Figs. 6.1 and 6.2. For positive values of $\Delta\theta$ the impact track is shifted in the direction of the end of the impact track, increasing the risk in Brazil and Papua New Guinea but simultaneously the risk in the region east of Papua New Guinea is reduced. For negative values of $\Delta\theta$ the impact track covers west Africa which has a high population density, simultaneously the risks in Brazil and Papua New Guinea are reduced. This behavior is reflected in the sensitivity map in Fig. 6.3 where the differences are reasonably small.

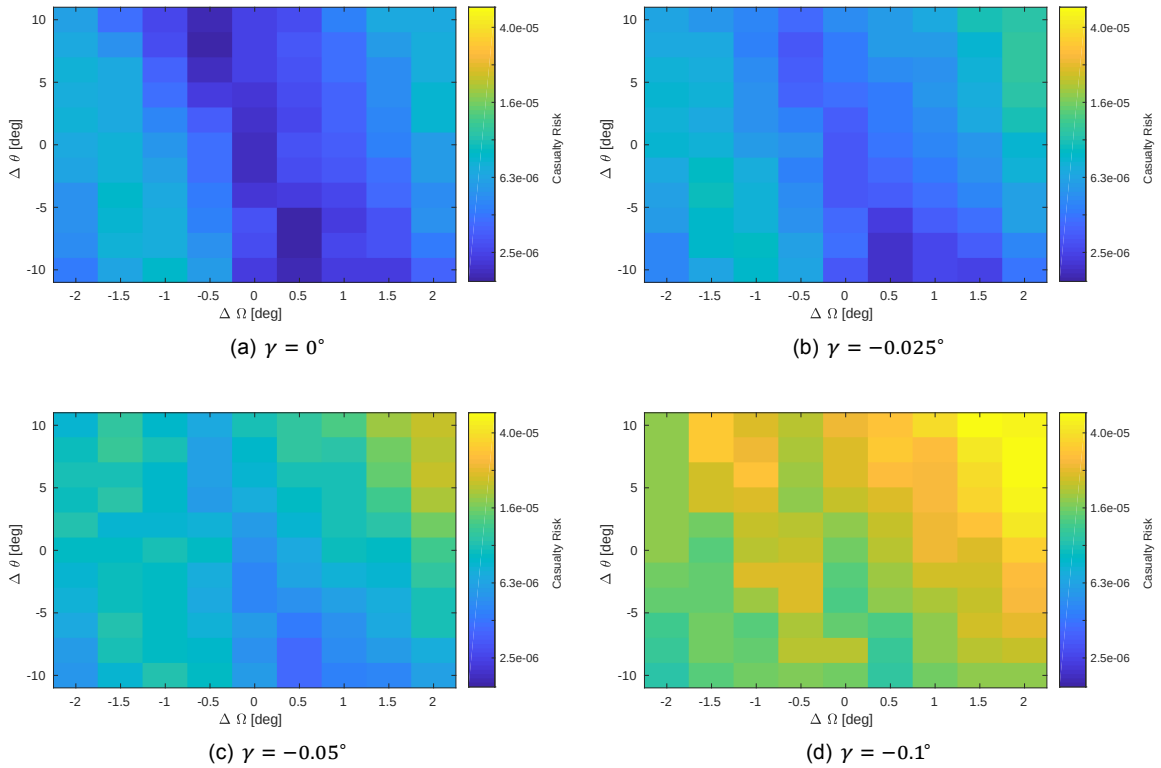

(a) $\gamma = 0^\circ$ (b) $\gamma = -0.025^\circ$

(c) $\gamma = -0.05^\circ$ (d) $\gamma = -0.1^\circ$

Figure 6.3: Sensitivity of the optimimum of the SPOT5 case to deviations in state at 150 km. The green rectangle indicates the minimum casualty risk, red rectangles indicate violations of the casualty risk requirement.

The found risks for a value of the flight path angle of 0 are all one to two orders of magnitude lower than the set requirement as shown in Fig. 6.3(a). The overall risks are increased for more steep entries. The casualty risks for steep entries as shown in Fig. 6.3(d) are close to the set requirement. This is caused by the shift of the impact track in the direction of the start. For such high entry angles the track covers west Africa which has high population density which causes the increase in casualty risk.

6.1.4. Case 4: SPOT5LIKE

The results of the sensitivity analysis regarding variations in initial conditions at 150 km altitude, for the SPOT5LIKE case are shown in Fig. 6.4. The configuration of the impact track found in Fig. 5.5(b) suggested sensitive behavior because the impact track is located close to high population densities in the north of America, west Africa and Papua New Guinea. This sensitive behavior was indeed found, as can be seen in Fig. 6.4. Note that the casualty risk requirement is violated for all values of the flight path angle. The violations are all located in the upper right corner. This is attributed to the shift of the impact track to the right resulting in the coverage of west Africa. The part of the impact track which covers west Africa has high probability. This is clearly reflected by the steep increase in risk in the upper right corner. The flight path angle has much lower effect as for the other cases. This is to be expected as the start and end of the impact track are located in a region with low population densities and these points are not surrounded by large population concentrations as was the case for the PARASOL and SPOT5 where the start of the impact track was located close to west Africa.

6.1.5. General discussion on the sensitivity to deviations in state at 150 km.

In general, systematic behavior was found for deviation in the state of the satellite at 150 km altitude. For all cases, changing the value of the longitude of ascending node caused some parts of the trajectory to cover regions with higher population density. Changing the value of true anomaly resulted in similar behavior. The impact probability in part of the covered regions were increased, resulting in higher risks.

The effect of the flight path angle was found to be marginal for values up to -0.05°. Large differences

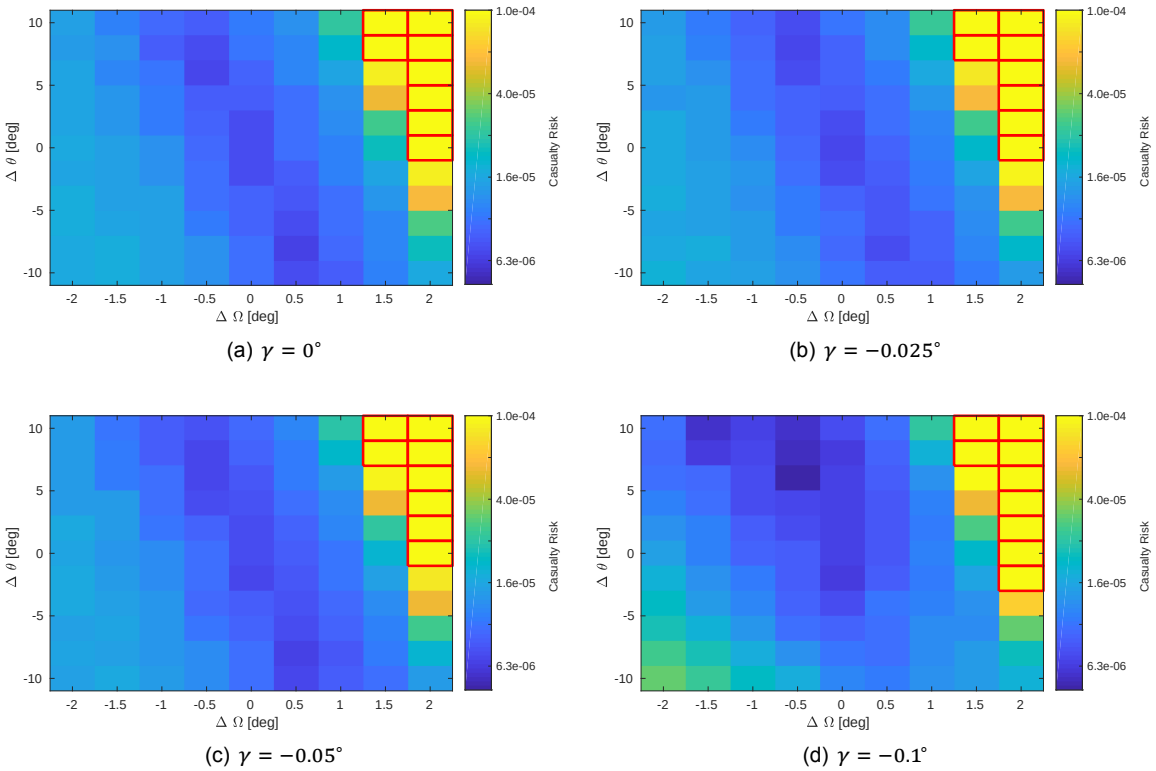

(a) $\gamma = 0°$ (b) $\gamma = -0.025°$

(c) $\gamma = -0.05°$ (d) $\gamma = -0.1°$

Figure 6.4: Sensitivity of the optimimum of the SPOT5LIKE case to deviations in state at 150 km. The green rectangle indicates the minimum casualty risk, red rectangles indicate violations of the casualty risk requirement.

were observed for entry angles of $-0.1°$ in the PARASOL and SPOT5 case. This value for the flight path angle significantly moved the impact track in the direction of start of the impact track, which caused the impact track to cover west Africa. As the population density in west Africa is high, this resulted in a large increase in casualty risk.

It is important to note that the variations in flight path angle due to an imperfect GNC system are likely small and will not effect the results considerably. These variations are small, since the maximum value found for the flight path angle, during the optimization of the complete setup, was found to be $0.06°$, which required dedicated thrusting during the complete controlled part of the disposal strategy. The impact of errors in the GNC stystem is further reduced by the circularization of the orbit caused by the atmosphere. For the optimization of the complete setup, the shift caused by a non zero flight path angle is taken into account as the impact track is constructed around the nominal impact point. However, the changes in shape of the impact PDFs for different flight path angles, as found in Section 4.5, were not taken into account. The optimization of the last 150 km assumed a flight path angle of zero. The entry conditions for the optimal values of the two optimization methods were not located close to each other which is possible as similar nominal impact locations can be achieved with a different combination of the entry location and the flight path angle. For finding the optimal impact track, neglecting the flight path angle for the optimization from 150 km altitude is accurate enough as optimal solutions were found with both optimization strategies which showed large similarities. However, it should be taken into account when a range of entry states is sought for with minimal risks for the GNC system to target.

Finally, only the inclination of the end-of-life orbit was found to affect the sensitivity of the results as is clearly seen when comparing the SPOT5 and SPOT5LIKE case which have the same ballistic coefficient and mass but have different inclination. The mass and ballistic coefficient did not influence the sensitivity behavior of the results. Those parameters merely define the limits of the achievable casualty risks.

In Table 6.1 the impact on the values for the casualty risk are shown for different values of uncertainty in the initial state. The flight path angle is not considered here as it is expected that the errors in that parameter caused by an imperfect GNC system are small. A block of 1x1 indicates an uncertainty of

$0.5°$ in longitude of ascending node and $2°$ in true anomaly and is assumed uniformly distributed.

Table 6.1: Impact on casualty risk for different levels of uncertainty in the initial state at 150 km altitude. The values indicate the average of a block of $n \; x \; n$ pixels centered at the optimal value as shown in the sensitivity maps at the start of this section.

Size of block	Case 1: PARASOL	Case 2: SMOS	Case 3: SPOT5	Case 4: SPOT5LIKE
3x3	+21%	+13%	+40%	+19%
5x5	+80%	+74%	+68%	+37%
7x7	+138%	+293%	+101%	+93%

The values shown in Table 6.1 are used to put the deviations as will be found in Sections 6.3 and 6.4 in perspective. The uncertainty of the 3x3 block in km is approximately 170x670 km, at the equator. It is likely that the GNC system is able to put the satellite in the correct location within these margins.

6.2. Seed variability

In this section the seed used in the optimization is varied in order to guarantee that the obtained results are robust. The seeds used for this sensitivity analysis are $[12345, 12346, 12347, 12348, 12349]$. The first seed is the one used for generating the results in Chapter 5. The evolution of the best casualty risks are shown in Fig. 6.5. Only the first 100 generations are shown as the major improvements are made there. The resulting optimal casualty risks are displayed in Table 6.2.

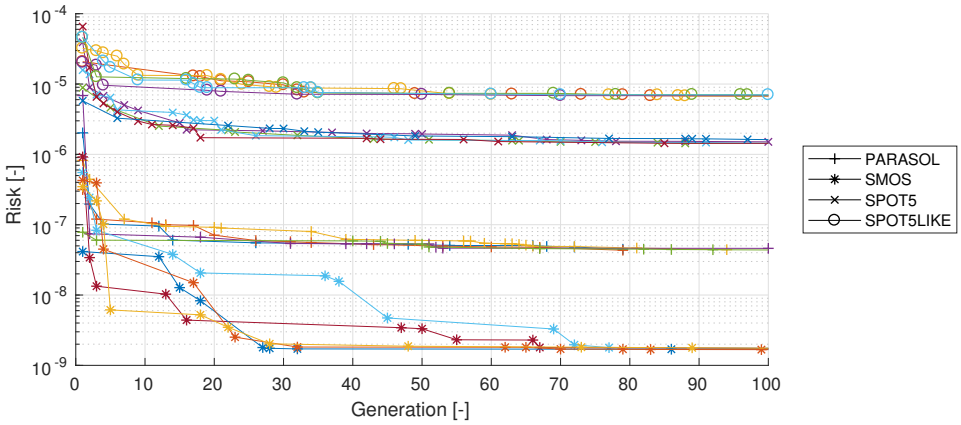

Figure 6.5: Convergence for different seeds of the jDE algorithm

Table 6.2: Optimal casualty risks for the second optimization using different seeds. The seed of 12345 was used for the results in Chapter 5.

Seed	Case 1: PARASOL	Case 2: SMOS	Case 3: SPOT5	Case 4: SPOT5LIKE
12345	$4.4801 \cdot 10^{-8}$	$1.6949 \cdot 10^{-9}$	$1.3706 \cdot 10^{-6}$	$6.4547 \cdot 10^{-6}$
12346	$4.3331 \cdot 10^{-8}$	$1.7340 \cdot 10^{-9}$	$1.3558 \cdot 10^{-6}$	$6.4439 \cdot 10^{-6}$
12347	$4.4162 \cdot 10^{-8}$	$1.6722 \cdot 10^{-9}$	$1.3631 \cdot 10^{-6}$	$6.3738 \cdot 10^{-6}$
12348	$4.5227 \cdot 10^{-8}$	$1.6725 \cdot 10^{-9}$	$1.3586 \cdot 10^{-6}$	$6.3675 \cdot 10^{-6}$
12349	$4.2005 \cdot 10^{-8}$	$1.6844 \cdot 10^{-9}$	$1.2408 \cdot 10^{-6}$	$6.5232 \cdot 10^{-6}$

Table 6.2 shows similar casualty risks for the different seeds for the random number generator. As all cases show similar behavior and the values for the casualty risks are similar, this makes it more likely that the optimum found is the global optimum.

6.3. Population growth

This section investigates the effect of the population growth on the resulting casualty risks. Not only the average growth is taken into account but also regional differences are taken into account. Projections of future population density distributions and the exact population density distributions from the past are obtained from Ref. [14]. Expected regional differences for the population density between 2015 and 2020 are shown in Fig. 6.6.

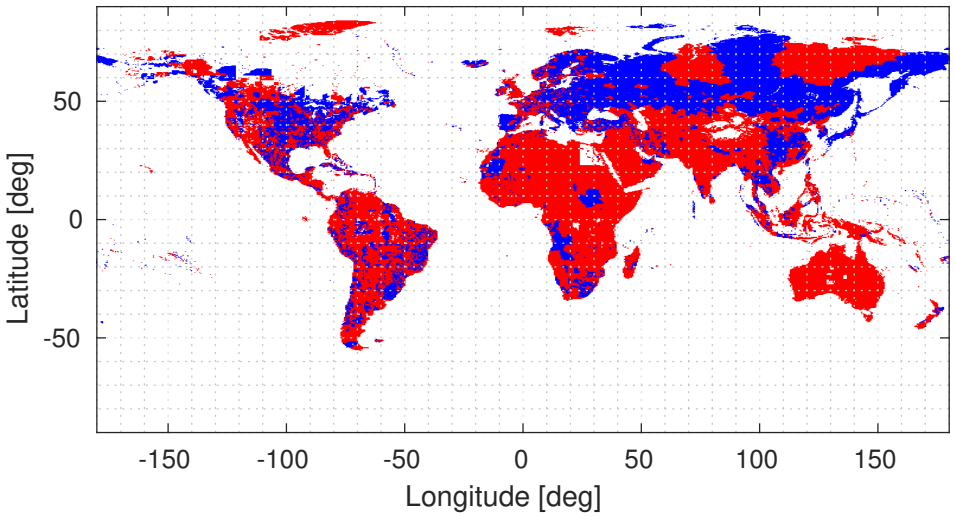

Figure 6.6: Population growth between 2015 and 2020, blue indicate decrease in population, red an increase [14].

Figure 6.6 shows mostly an increase of population density in the areas crossed by the optimal impact tracks in Chapter 5, Africa, Australia, and Papua New Guinea.

The resulting casualty risks, when using the population distribution for 2000 and the expected population distribution for 2020, are shown in Table 6.3. The casualty risks are compared against the average population growth of the world. The average population growth between 2000 and 2015 was 20% and the population is expected to grow 5.6% between 2015 and 2020 [55].

Table 6.3: Effect of projected regional population growth on the casualty risk of the optima.

	Case 1: PARASOL	Case 2: SMOS	Case 3: SPOT5	Case 4: SPOT5LIKE
E_{2000}	$3.6894 \cdot 10^{-8}$	$1.9769 \cdot 10^{-9}$	$1.0311 \cdot 10^{-6}$	$5.6415 \cdot 10^{-6}$
E_{2015}	$4.5103 \cdot 10^{-8}$	$1.7208 \cdot 10^{-9}$	$1.3733 \cdot 10^{-6}$	$6.4840 \cdot 10^{-6}$
E_{2020}	$4.8000 \cdot 10^{-8}$	$1.6434 \cdot 10^{-9}$	$1.5175 \cdot 10^{-6}$	$6.7305 \cdot 10^{-6}$
Δ 2000→2015	+22.3%	-13.0%	+33.2%	+14.9%
Δ 2015→2020	+6.4%	-4.5%	+10.5%	+3.8%

First, observations are made for the differences between 2015 and 2020 after which the differences over the period from 2000 to 2015 are discussed. The PARASOL, SPOT5 and SPOT5LIKE case follow the trend of the average population growth on the Earth. The SPOT5 case has a slightly larger increase in casualty risk which is caused by an above average population growth in Africa. The SPOT5LIKE case has a slightly lower increase in casualty risk which is caused by a decrease of population density in Canada and the north of the United States. The SMOS case shows a decrease of the risk in Table 6.3. The largest contributions for the casualty risk of the SMOS case originate from population concentrations in the east of Russia, the population in this area has decreased over time and therefore a reduction is seen in the casualty risks for the SMOS case. Between 2015 and 2020 the same behavior is observed. The PARASOL, SPOT5 and SPOT5LIKE cases increase with a similar rate as the average population of the world, the PARASOL case is again closest to the average rate, the SPOT5 case a slightly larger increase and the SPOT5LIKE case is a little bit below the average. Again, a decrease in risk is observed for the SMOS case.

The results in Table 6.3 shows that there is no need for accurate regional population growth models. Using the average population growth to scale the casualty risks introduces errors below 12% for the cases with higher risks and a maximum error of 35% for the SMOS case. The errors are below 1% per year for all cases except the SMOS case for which the error is just below 2% per year. To put these numbers in perspective, the differences found here over a period of 15 years are comparable to the increase of the casualty risk due to an uncertainty of $1.5°$ in longitude of ascending node and $6°$ in true anomaly.

Using only the worlds average population growth to scale the risks as is done by the software used Ref. [6] and other debris risk assessment tools such as Ref. [15] is appropriate. In case the precision of the GNC system of the satellite is known, and high-fidelity risk calculations are made, a slightly more accurate predictions can be performed using a population map with regional population growth expectations.

6.4. Effect of a normally distributed impact probability function

This section investigates the effect of using a normally distributed impact PDF for the calculation of the risk. The casualty risk of the optimal impact track is calculated using the KDE PDF from the optimal result and compared to a normally distributed PDF. The PDFs used by the original optimizations and the normal distribution used in this sensitivity analysis are shown in Fig. 6.7.

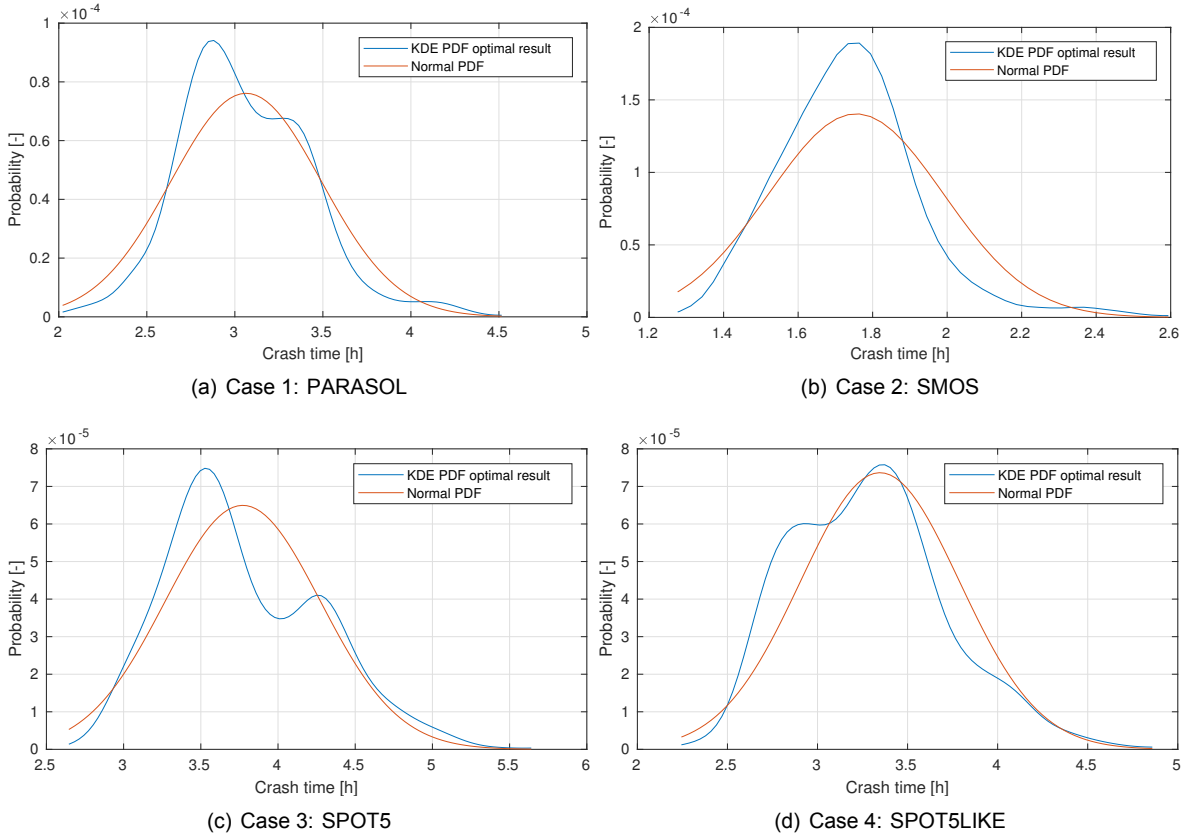

(a) Case 1: PARASOL

(b) Case 2: SMOS

(c) Case 3: SPOT5

(d) Case 4: SPOT5LIKE

Figure 6.7: Overview of the used PDFs for the sensitivity analysis of normally distributed PDF vs the KDE PDF.

The casualty risks calculated using the normally distributed PDF are compared to the baseline casualty risks in Table 6.4.

Table 6.4 indicates small differences in casualty risks between the different cases considered. The small increase for the PARASOL case originates from the overestimation of the impact probability in the end of the PDF as shown in Fig. 6.7(a). This point is located over Papua New Guinea and Australia which are the main contributers to the casualty risk of the optimal solution. The same reasoning can be applied to the SMOS case. In the optimal track of the SMOS case, the region with the largest

Table 6.4: Effect of assuming a normally distributed PDF instead of using a KDE PDF.

	Case 1: PARASOL	Case 2: SMOS	Case 3: SPOT5	Case 4: SPOT5LIKE
E_{KDE}	$4.4801 \cdot 10^{-8}$	$1.6949 \cdot 10^{-9}$	$1.3706 \cdot 10^{-6}$	$6.4547 \cdot 10^{-6}$
E_{Normal}	$4.8140 \cdot 10^{-8}$	$1.8824 \cdot 10^{-9}$	$1.3605 \cdot 10^{-6}$	$5.5309 \cdot 10^{-6}$
ΔE	+7.5%	+11.1%	-0.8%	-14.3 %

contribution to the casualty risk is located in eastern Russia at the end of the impact track. The normal distribution overestimates the probability at this point as shown in Fig. 6.7(b). For the SPOT5 case, the normal PDF shows good agreement with the KDE PDF at the regions which contribute most to the casualty risk as shown in Fig. 6.7(c). For the SPOT5LIKE case, a decrease in the found casualty risk is observed. This is caused by the underestimation of the probability in the first part of the impact track as shown in Fig. 6.7(d). This part part of the PDF corresponds to the region in the north west of the United States which is one of the main contributers to the minimum casualty risk.

The values of the differences shown here are small. Comparing them to the values in Table 6.1 shows that small uncertainties in the state at 150 km altitude have a much larger influence on the results than the shape of the distribution. Therefore, using the more detailed impact PDF is not necessary for the optimization of state at 150 km altitude for the semi-controlled disposal strategy.

7

Conclusions and recommendations

This thesis investigated the feasibility of the semi-controlled end-of-life disposal strategy employing low-thrust electric propulsion. This research aims to bridge two main gaps for the feasibility of this strategy. First, the extent to which the casualty risk can be reduced by using this strategy. Second, the effect of assumptions made in previous research. This chapter concludes the research of this thesis. First, in Section 7.1 the research questions for this thesis are answered. Next, in Section 7.2 recommendations are provided for future work. Finally, the implications of this work are given in Section 7.3.

7.1. Conclusions

In this thesis two research questions with associated subquestions were formulated to bridge the scientific gaps in current literature. The answers to these questions will be provided separately.

1. **What is the reduction in casualty risk possible by employing a semi-controlled end-of-life disposal strategy compared to an uncontrolled strategy?**
   To answer this research question, the trajectory of the disposal strategy for different cases have been optimized with the following assumptions: the satellite is propagated with three degrees of freedom, the satellite is accurately controlled down to 150 km altitude, a population map from 2015 is used, and drag, thrust, and a spherical harmonic gravity field of degree and order 2 are considered the only perturbations. These assumptions were stated in Section 4.2. Justification for these assumptions is presented in Chapters 4 and 6. For all cases the risk was reduced significantly compared to the values for the uncontrolled disposal strategy. The parameters for all cases can be found in Table 4.1. The risk for the PARASOL case was reduced by 3 orders of magnitude, from $3.9095 \cdot 10^{-5}$ to $4.4801 \cdot 10^{-8}$. For the SMOS case the risk was decreased with 5 orders of magnitude, from $1.6433 \cdot 10^{-4}$ to $1.6949 \cdot 10^{-9}$. This large reduction is possible as the satellite has a large ballistic coefficient which results in a much shorter impact track. For the SPOT5 and SPOT5LIKE cases, reductions of two orders of magnitude were found. The risks decreased from $2.8975 \cdot 10^{-4}$ and $4.3280 \cdot 10^{-4}$ to $1.3706 \cdot 10^{-6}$ and $6.4547 \cdot 10^{-6}$ for the SPOT5 and SPOT5LIKE case respectively. The SPOT5 satellite has a lower ballistic coefficient resulting in a longer impact track. For the SPOT5LIKE case the least improvement in casualty risk was found. Due to the low inclination of this case it was more difficult to position the impact track favorably. Uncertainty in the calculated values for the casualty risks are expected to be less than 32% for the PARASOL, SPOT5 and SPOT5LIKE cases, as found in Section 4.7 by comparing uncontrolled risks with values from literature. The uncertainty for the casualty risk of the SMOS case is larger as the effect of the ballistic coefficient on the casualty area is not taken into account since a simple relation is used which is solely based on the entry mass of the satellite as discussed in Section 3.4.

   (a) **What is the effect of only propagating the uncontrolled part of the disposal strategy compared to propagating the complete disposal strategy from the end-of-life orbit?**
   To answer this subquestion, a second optimization was performed, which only simulated the ballistic part of the entry from an altitude of 150 km. The second optimization was performed

under the following assumptions: the satellite is propagated with three degrees of freedom, the state of the satellite at 150 km altitude is exact, the flight path angle at 150 km altitude is fixed to 0°, a population map from 2015 is used, and drag, thrust, and a spherical harmonic gravity field of degree and order 2 are considered the only perturbations. These assumptions are described in more detail in Section 4.2. Justification for these assumptions is presented in Chapters 4 and 6. The impact tracks of both optimizations were found to be highly similar. The casualty risks found were also similar. The optimization from 150 km altitude managed to improve the solution of the complete setup up to 1 order of magnitude for the considered cases.

Besides comparable risks, the run-times of the optimization of the last 150 km are only a fraction of those of the complete setup. The optimization of the complete disposal maneuver required 59 to 101 h. The optimizations of the last 150 km only required run-times of 0.12 to 1.2 h. Future research on the topic should definitely split the problem in two pieces. First, the capabilities of the satellite in the transfer from end-of-life orbit down to 150 km altitude need to be found. Then use this knowledge to find the optimal entry point. When this is performed, the trajectory from end-of-life orbit down to 150 km can be optimized. Note that a-priori knowledge is required for the bounds of the state at 150 km altitude which need to be found from simulations of the controlled part of the disposal strategy.

(b) **What is influence of different ballistic coefficients and/or different initial mass of the satellite on the calculated casualty risk?**

To answer this subquestion, the results of the optimization from 150 km altitude for the PARASOL, SMOS and SPOT5 cases are compared. The same assumptions have been made as discussed above. The ballistic coefficients of the cases are 0.01833, 0.03515, and 0.015 m^2/kg for the PARASOL, SMOS and SPOT5 case respectively. The masses of the satellite are 120, 630, and 3000 kg respectively. The high ballistic coefficient of the second case resulted in a shorter impact probability track. This impact track did not cross any densely populated areas on the Earth and therefore, achieved much lower casualty risks compared to the other cases. The casualty risk for the SMOS case was found to be $1.6949 \cdot 10^{-9}$. The lower ballistic coefficients of the PARASOL and SPOT5 case resulted in a longer impact probability track and therefore it was not possible to find an impact track which did not cross any densely populated area. This resulted in higher values for the casualty risk, the casualty risk for the PARASOL and SPOT5 case were $4.4801 \cdot 10^{-8}$ and $1.3706 \cdot 10^{-6}$ respectively. The difference in risk between these cases is caused by the slightly lower ballistic coefficient for the SPOT5 case, increasing the impact track compared to the PARASOL case. Also, the SPOT5 satellite has a much higher mass. The resulting casualty area is therefore 7.5 times as large and the casualty risk scales linearly with this value as indicated in Section 3.4. Therefore, designing satellites with large ballistic coefficients and low mass is beneficial for the casualty risk.

(c) **To what extent does the inclination of the end-of-life orbit affect the calculated casualty risk?**

To answer this subquestion, the results of both optimizations discussed above are compared for the two SPOT5 cases with inclinations of $98.6°$ and $51°$ respectively. The optimal solution of the SPOT case has a casualty risk of $1.3706 \cdot 10^{-6}$, for the SPOT5LIKE case, which has the lower inclination, a casualty risk of $6.4547 \cdot 10^{-6}$ was found which is almost 5 times as high. Furthermore, the results of the SPOT5LIKE case are much more sensitive to uncertainties in the state at 150 km altitude as found in Section 6.1. This is caused by the configuration of the impact track on the population map. The optimal track lays very close to Africa which has a high population density. Small deviations in the longitude of ascending node causes the satellite to cover this region and the casualty risk easily increases to above the casualty risk limit set by ESA in [1]. When the track is shifted in the opposite direction the risks in North America increase significantly. This sensitive behavior is expected in general, low inclination impact tracks will cover populated area somewhere on the Earth. Therefore, extra care must be taken when designing satellites in LEO with low inclination. The requirements for the GNC system will likely be more strict with respect to the GNC requirements for the same satellite in a higher inclination orbit. To limit the casualty risk of future space missions, high inclination orbits are preferred, as the optimal impact tracks are less sensitive to deviations at 150 km

altitude.

2. **To what extent do the assumptions made in Ref. [6] affect the calculated casualty risk of the semi-controlled disposal strategy?**
   The answer to this research question is based on the outcome of the subquestions. Therefore, the answer is provided after all subquestions are answered.

   (a) **What is the effect of assuming a circular orbit at the point of atmospheric re-entry for the calculation of the casualty risk?**
   To answer this subquestion, a sensitivity analysis was performed in Section 6.1, where the value of the flight path angle at the point of atmospheric re-entry was varied from 0° to a value of -0.1°. This variation of flight path angle shifts the impact track PDF forward in time. The shape of the distribution for steeper entry angles resembles the shape found for a negative change in the true anomaly of the point of atmospheric re-entry. Due to this effect, the re-entry states between the two optimization strategies employed did not show similar values. When performing the optimization of only the last 150 km, the flight path angle needs to be varied. This gives a larger range of possible re-entry conditions which can be targeted with a separate optimization of the controlled part of the trajectory. For the values of the flight path angles up to -0.05° the impact on the casualty risk is marginal. The variations in flight path angle due to an imperfect GNC system are small. The maximum value of the flight path angle encountered during simulations was $-0.06\circ$ which required dedicated thrusting during the complete controlled part of the disposal maneuver. This is caused by the atmosphere which circularizes the orbit. The low accelerations from the low-thrust propulsion systems available to date are not able to change the eccentricity of the orbit to a large enough extend to increase the flight path angle much further. Since the thrust has limited effect on the flight path angles, the errors due to an imperfect GNC will have an even lower impact on the flight path angles and therefore the risk. For finding the optimal impact track on the Earth, neglecting the flight path angle for the optimization from 150 km altitude is accurate enough as similar optimal solutions were found with both optimization strategies employed in this research. However, the flight path angle should be taken into account when a range of entry states is sought for, which can be used by the GNC system as target.

   (b) **What is the effect of scaling the casualty risk with the average population growth with respect to regional expected population growth?** To answer this research question, the casualty risks for the optimal trajectory of four different cases for populations maps from the years 2000, 2015 and 2020 are compared. The casualty risk differences found with the different population maps are compared with the average growth of the population. The average population growth between 2000 and 2015 was 20%. The casualty risk of the optimal trajectory of the PARASOL case increased with 22.3% between 2000 and 2015. The population growth in the covered regions followed the trend of the population growth of the world. The risk of the SPOT5 case increased with 33.3%. The regions covered by the optimal impact track of the SPOT5 case covered regions with higher regional population growth compared to the average population growth. The increase of the SPOT5LIKE case was only 14% since the population density in Canada and the north of the United States increased with less that the average world population growth. The SMOS case showed a decrease in risk of 13% over the period from 2000 to 2015 since the covered regions showed a decrease in population. The average population growth in the period between 2015 and 2020 is expected to increase with 5.6%. All cases except the SMOS case followed this trend. The differences in casualty risks between 2015 and 2020 are 6.4%, -4.5%, 10.5% and 3.8% for the PARASOL, SMOS, SPOT5 and SPOT5LIKE case respectively. Similar behavior was found as for the period between 2000 and 2015.
   These results shows that there is no need for accurate regional population growth models. Using the average population growth to scale the casualty risks introduces errors below 1% per year for all cases except the SMOS case. For that case the error is within 2% per year. These differences are marginal if compared against the uncertainty in the calculated risk of 30%. For high-fidelity casualty risk calculation of specific cases, these regional differences should be considered, as the uncertainty in the calculated risk is lower.

   (c) **What is the effect of assuming a normally distributed impact probability function for**

the calculation of the casualty risk with respect to a non-parametric probability function dependent on the location of the atmospheric re-entry?
To answer this subquestion, the calculation of the casualty risk for the optimal trajectories is repeated with a normal probability density function(PDF). Four cases are again considered which are described in Table 4.1. The PDF in this thesis is constructed using the non-parametric method of kernel density estimation (KDE) as discussed in Section 4.5. The difference in the casualty risks between both the KDE PDF and the normal PDF are 7.5%, 11.1%, -0.8% and -14.3% for the PARASOL, SMOS, SPOT5 and SPOT5LIKE case respectively. The increase of the risk for the PARASOL case is caused by an overestimation of the impact probability in Papua New Guinea. For the SMOS case the increased value of the casualty risk originates from an overestimation of the impact probability in the eastern part of Russia. For the SPOT5 case the impact probabilities in the regions which contributed most to the total casualty risk were similar. When the region of largest contribution to the total casualty risk was located in the middle of the impact track the results would be much different as large differences between the PDFs are present in the middle. However, for the optimal results this part of the impact track is located in the Atlantic Ocean and therefore the impact is low. For the decrease in risk as found for the SPOT5LIKE case is caused by an underestimation of the probability of impact in the north-west of the United States which is the region with the largest contribution to the total casualty risk. The differences in risk are small when comparing to the uncertainty in the risk calculation in general. Therefore, using a normal PDF for the impact probability is accurate enough for finding an optimal impact track on the Earth and to get an estimate of the resulting casualty risk. For high-fidelity casualty risk calculation of specific cases, a non-parametric distribution is recommended, as the uncertainty in the calculated risks in that case are lower.

By combining the answers of the subquestions stated above, the second research question can be answered. The effects of the assumptions in [6] on finding the optimal trajectory are small. Using non zero flight path angles are relevant for finding the range of conditions which could be targeted in the controlled part of the entry. For the finding the value of the minimum casualty risk, taking the flight path angle into account is not required. Using the average population growth to scale the casualty risk to a future impact year introduces minor errors in the calculated risk. However, the uncertainty of the low-fidelity model introduces larger errors in the calculated risk. The impact of using a normal PDF instead of a non-parametric PDF is also small compared to the uncertainties of the calculation of the risk. Using a non-parametric PDF and regional population growth expectations are only recommended for high-fidelity casualty risk calculation but are not required for finding the re-entry point resulting in minimum risk.

7.2. Recommendations

Based on the results and conclusions of this research recommendations are given in this section. These topics require attention for future research into the feasibility of the semi-controlled end-of-life disposal strategy and to limit the casualty risk of future end-of-life satellite disposals.

First, a detailed analysis is required for the controlled part of the disposal maneuver. The limitations of the GNC system of representative satellites need to be investigated, i.e., satellites in LEO equipped with low-thrust propulsion of which the uncontrolled risk is above 1 in 10000. The accuracy to which the state of the satellite can be controlled at the point of re-entry is important for a more detailed calculation of the casualty risk of a satellite. A better knowledge of these capabilities increase the accuracy of the risks found in this thesis.

Second, a more robust optimization needs to be performed of the last 150 km. If the knowledge of the accuracy of the GNC system on representative satellites is increased, this can be taken into account during the optimization. This should result in an optimum which is less sensitive to perturbations in the state at 150 km and behavior as seen in Section 6.1 for the SPOT5LIKE case is avoided.

Furthermore, for the design of future satellite missions it is recommended to have a large ballistic coefficient and minimize the mass of the satellite, since this reduces the length of the impact track and the casualty area of the satellite, resulting in smaller casualty risks.

Finally, it is recommended for future preliminary assessments of the casualty risks for semi-controlled re-entries, that only the uncontrolled phase is simulated. The computational effort of optimizing the

complete trajectory is too large. If an optimized trajectory for the controlled phase is required, it is recommended to use a different integrator, since integrators are available which achieve similar accuracies with less function evaluations. Furthermore, the application of multi-threading for the optimization could to reduce the run-times considerably. The method of orbital averaging could also help in reducing the computational effort as is used in other low-thrust optimizations. However, it must be investigated down to which altitude this method is valid. Another solution would be to find the altitude from which the GNC system is still capable of achieving the desired states at re-entry from any state at that altitude above the Earths surface. In that case the first part from end-of-life orbit does not need to be propagated reducing a large part of the computational effort.

7.3. Implications

The results obtained in this thesis can be brought to a broader perspective. This research formed the next step in the investigation of the feasibility of the semi-controlled end-of-life disposal strategy. Applying this strategy can greatly reduce the expected casualty risks of de-orbiting satellites to far below the requirement currently set. With the current launch rate of 357 launched objects and the current requirement, on average at least 1 person will die every 28 year due to debris from space. This number is likely larger as many of the large orbiting bodies result in much higher risks. For example the Tiangong-1 space station which de-orbited recently had a probability larger than 1 in 5000. When applying the semi-controlled re-entry strategy on average 1 person dies every 2800 years, which is a much more reassuring number for the population on the Earth. Ultimately, (semi-)controlled entries are applied to all satellites at end-of-life.

A

Verification

This chapter gives an overview of the verification activities performed. The activities described in this chapter verify the correct implementation of the numerical methods as described in Chapter 3 First, in Appendix A.1 the basic implementation of the control parameterization is verified. Next, in Appendix A.2 the implementation of the optimization is verified. This is done by targeting different orbital elements with the costates as control parameters. Also a combination of elements is targeted for. Then, an optimization is performed for minimizing the casualty risk with simplified population maps and a small impact track in Appendix A.3.

A.1. Control parameterization

The implementation of the control parameterization as discussed in Section 2.6 is verified in this section. An arbitrarily chosen satellite is propagated with constant values for the costates. The direction of the thrust and the change of the orbit over time is checked for correct behavior. The initial orbital elements are $a = 20000$ km, $e = 0$, $i = 0$ rad, $\omega = 0$ rad, $\Omega = 0$ rad, $\theta = 0$ rad. Furthermore, the thrust of the satellite is 10 N, and the mass of the satellite is 800 kg. The costates are set to $1 \cdot 10^{-9}$ unless otherwise stated. Furthermore, only the central gravity and the thrust are taken into account as perturbations. The satellite is simulated for one orbital revolution to indicate the direction of the thrust and for multiple revolutions to indicate the long term effect of such a thrust profile. The verification results for the first costate is shown in Fig. A.1. The cross in the figures indicates the starting position of the satellite, the arrows indicate the direction of the thrust and the blue dot indicates the Earth.

In Fig. A.1(a) the direction of the thrust acceleration is shown for a positive value for λ_p. Note that all other costates are set to a small value. As expected the thrust acceleration is directed against the flight direction, causing a deceleration of the satellite. This is also reflected in the orbital behavior when the satellite is propagated for a longer period as shown in Fig. A.1(b). It can be seen that the semi-latus rectum of the satellite is reduced since the satellite moves closer to the central body. Note that, a positive value of λ_p results in a decrease in p, this is because the control parameterization, as discussed in Section 2.6, specifies the direction of the thrust, which is opposite to the thrust acceleration. Therefore, the behavior seen here is the expected behavior. In Figs. A.1(c) and A.1(d) the acceleration and trajectory for a negative value of λ_p is shown. Note that the opposite effect is observed compared to Figs. A.1(a) and A.1(b). The thrust acceleration is in the direction of the velocity. This increases the semi-latus rectum which can be seen by the satellite spiraling outward. The behavior seen in Fig. A.1 is exactly as expected.

The verification results for the second costate is shown in Fig. A.2.

As described in Eq. (2.3), modified equinoctial element f is related to the Keplerian element e, and the cosine of $\omega + \Omega$. This relation is also visible in Fig. A.2(b), which shows the long term effect of a thrust acceleration in the direction indicated in Fig. A.2(a). The eccentricity is increased. Furthermore, the perigee ($\omega + \Omega$) is located at 180° such that the value for f is most negative ($\cos(180^\circ)$). Again note that, a positive value of λ_f results in a decrease in f, this is because the control parameterization, as discussed in Section 2.6, specifies the direction of the thrust, which is opposite to the thrust acceleration. For a negative value of λ_f as shown in Figs. A.2(c) and A.2(d) the eccentricity is also increased while the

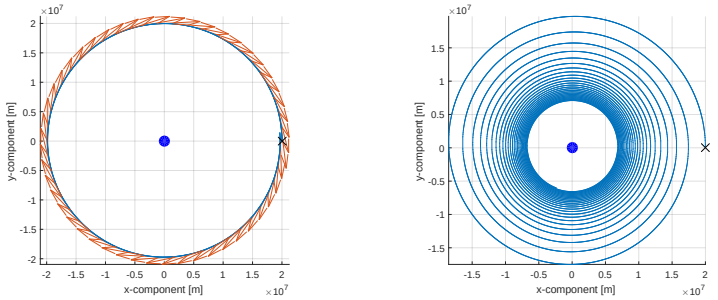

(a) $\lambda_p = 1 \cdot 10^9$ (b) $\lambda_p = 1 \cdot 10^9$

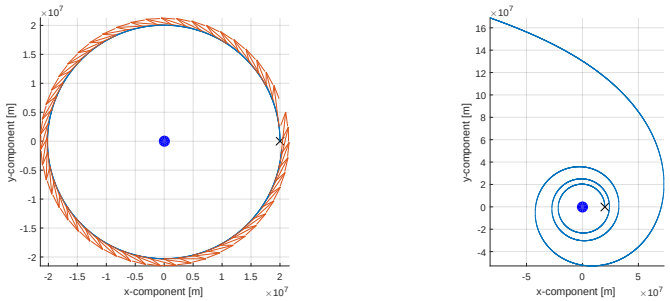

(c) $\lambda_p = -1 \cdot 10^9$ (d) $\lambda_p = -1 \cdot 10^9$

Figure A.1: Resulting direction of the thrust and change of satellite orbit for the verification of λ_p.

perigee is located at the other side of the central body at $0°$ to maximize the value of f. The directions of the thrust acceleration as indicated in Figs. A.2(a) and A.2(c) have similar orientations as described in [11, 32] for maximum eccentricity change. The behavior seen in Fig. A.2 is thus exactly as expected.

The verification results for the third costate is shown in Fig. A.3.

As described in Eq. (2.3), modified equinoctial element g is related to the Keplerian element e, and the sine of $\omega + \Omega$. Therefore, the same behavior as Fig. A.2 is expected but with the perigee located $90°$ further in clockwise direction as shown in Fig. A.3. This is exactly what is observed.

The verification results for the fourth costate is shown in Fig. A.4.

As described in Eq. (2.3), modified equinoctial element h is related to the tangent of Keplerian element i, and the cosine of Ω. This relation is also visible in Fig. A.4(b), which shows the long term effect of a thrust acceleration in the direction indicated in Fig. A.4(a). The inclination is increased. Furthermore, the longitude of ascending node is located at $180°$ such that the value for h is most negative ($\cos(180°)$). Again note that, a positive value of λ_h results in a decrease in h, this is because the control parameterization, as discussed in Section 2.6, specifies the direction of the thrust, which is opposite to the thrust acceleration. For a negative value of λ_h as shown in Figs. A.4(c) and A.4(d) the inclination is also increased while the perigee is located at the other side of the central body at $0°$ to maximize the value of h. The directions of the thrust acceleration as indicated in Figs. A.4(a) and A.4(c) have similar orientations as described in [11, 32] for maximum inclination change. The behavior seen in Fig. A.2 is thus exactly as expected.

The verification results for the fifth costate is shown in Fig. A.5.

As described in Eq. (2.3), modified equinoctial element k is related to tangent of Keplerian element i, and the sine of Ω. Therefore, the same behavior as Fig. A.4 is expected but with the longitude of ascending node located $90°$ further in clockwise direction as shown in Fig. A.5. This is exactly what is observed.

All results shown above verify the correct implementation of the control parameterization and the control parameterization can be applied to the optimization problem.

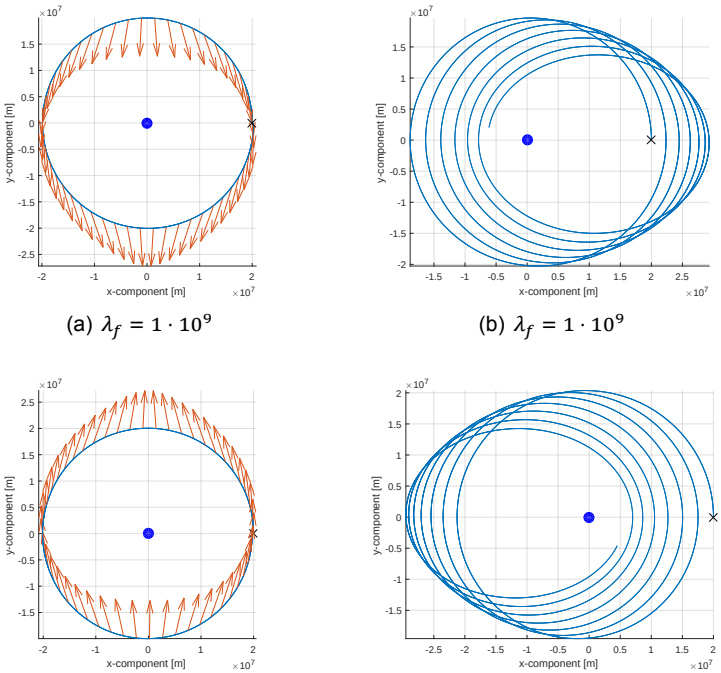

(a) $\lambda_f = 1 \cdot 10^9$ (b) $\lambda_f = 1 \cdot 10^9$

(c) $\lambda_f = -1 \cdot 10^9$ (d) $\lambda_f = -1 \cdot 10^9$

Figure A.2: Resulting direction of the thrust and change of satellite orbit for the verification of λ_f.

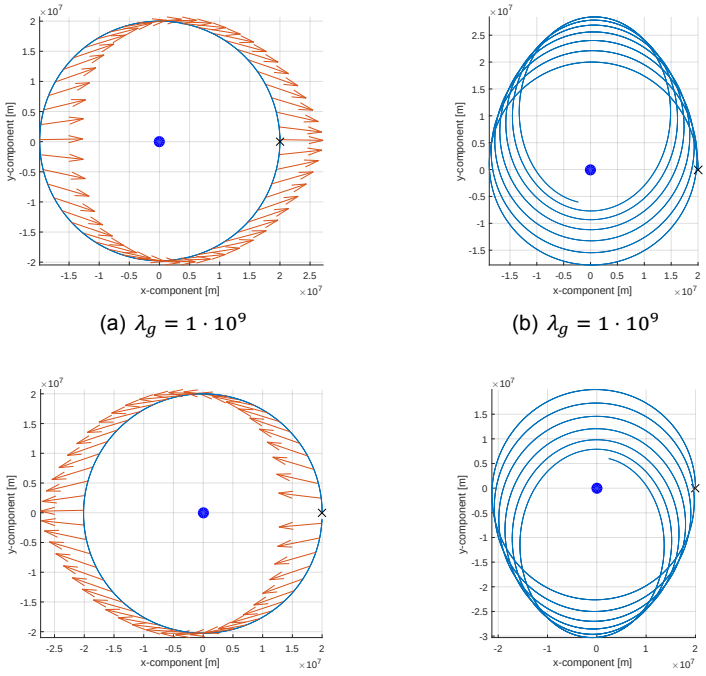

(a) $\lambda_g = 1 \cdot 10^9$ (b) $\lambda_g = 1 \cdot 10^9$

(c) $\lambda_g = -1 \cdot 10^9$ (d) $\lambda_g = -1 \cdot 10^9$

Figure A.3: Resulting direction of the thrust and change of satellite orbit for the verification of λ_g

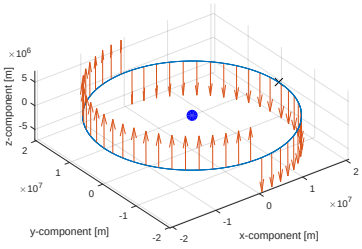

(a) $\lambda_h = 1 \cdot 10^9$

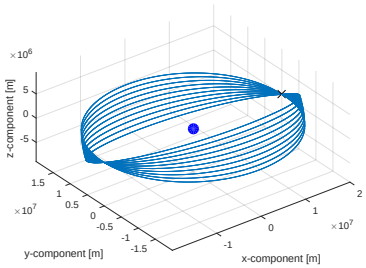

(b) $\lambda_h = 1 \cdot 10^9$

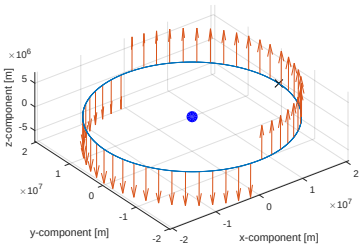

(c) $\lambda_h = -1 \cdot 10^9$

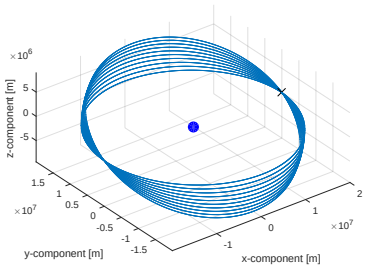

(d) $\lambda_h = -1 \cdot 10^9$

Figure A.4: Resulting direction of the thrust and change of satellite orbit for the verification of λ_h.

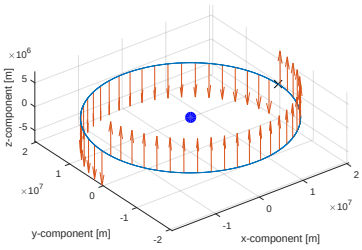

(a) $\lambda_k = 1 \cdot 10^9$

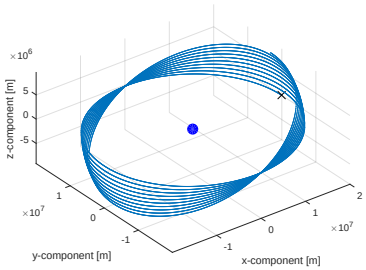

(b) $\lambda_k = 1 \cdot 10^9$

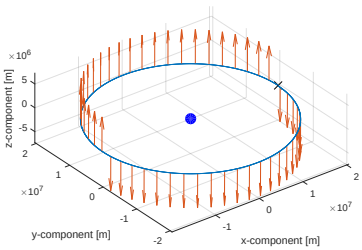

(c) $\lambda_k = -1 \cdot 10^9$

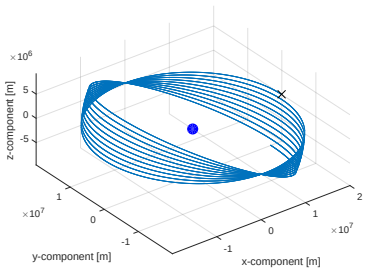

(d) $\lambda_k = -1 \cdot 10^9$

Figure A.5: Resulting direction of the thrust and change of satellite orbit for the verification of λ_k.

A.2. Differential evolution

This section describes the verification of the the entire software chain of this thesis. It is verified whether the propagation of the satellite in the environment is correctly linked to the optimization employing the jDE algorithm. The dynamical model used is discussed in Chapter 2 and the numerical methods applied are discussed in Chapter 3. The setup of the simulator is: discussed in Chapter 4. To verify the software chain, several cases are used which provide information about the correct linking of the propagation and optimization. First, the orbital parameters and satellite parameters used for the analysis are discussed. Next, single orbital elements are targeted. Finally, combinations of orbital elements are used as target.

A.2.1. Initial conditions and objective function

Aerodynamic drag is neglected and only the central gravity is used. The initial parameters for all the optimizations are:

$a = 20 \cdot 10^6$ m,	$\omega = 0°$,	$m = 400$ kg,
$e = 0.2$,	$\Omega = 0°$,	$I_{sp} = 2000$ s,
$i = 28.5°$,	$\theta = 0°$,	$F_{thrust} = 10$ N.

The objective function used by the jDE algorithm is defined in Eq. (A.1).

$$f = \sum_{k=0}^{n} W_k \cdot J_k \cdot (1 + 1000 P_i) \tag{A.1}$$

where f is the value of the objective function, n is the number of cost functions used, W_k the weight assigned to cost function J_k as given in Eq. (A.2). Finally, P_i is the penalty function with value 0 or 1 depending on whether a constraint for that cost function is violated. By assigning weights in this objective function, specific orbital elements can be targeted for. Furthermore, in case a targeted orbital element is not close to the desired value a penalty is given to force the optimization to search for solutions within a desired range of the orbital elements. This is only relevant for optimizations with multiple targets. The weights are assigned at in the upcoming sections as they are different for each investigated case. The constraints indicating the desired range for the orbital elements are:

$\Delta a < 1 \cdot 10^5$ m	$\Delta i < 0.015$ rad	$\Delta\Omega < 0.015$ rad
$\Delta e < 0.01$	$\Delta\omega < 0.015$ rad	

$$J_t = \frac{|t_t - t_{lb}|}{t_{ub} - t_{lb}} \tag{A.2a}$$

$$J_{a,\dots,\Omega} = \frac{\Delta OE}{|OE_i - OE_t| + \epsilon} \tag{A.2b}$$

where t_t is the transfer time, t_{lb} the lower bound for the transfer time used in the optimization and t_{ub} the upper bound. Furthermore, OE are the orbital elements $[a, e, i, \omega, \Omega]$, subscript i and t are indicating the initial and target orbital element respectively. ϵ is a small number added such that the function does not result in NaN values when initial and target OE are the same. Note that the true anomaly is omitted, this element changes rapidly and is therefore not useful in the optimization of the transfer trajectory. The controls are shown in Eq. (A.3), the costates are defined at two nodes and are linearly interpolated in between. The nodes are located at t_{lb} and t_{ub}.

$$\mathbf{u} = [\boldsymbol{\lambda}_0, \boldsymbol{\lambda}_1] \tag{A.3}$$

with

$$\boldsymbol{\lambda}_i = [\lambda_{p,i}, \lambda_{f,i}, \lambda_{g,i}, \lambda_{h,i}, \lambda_{k,i}] \tag{A.4}$$

The settings for the jDE are as follows:

$t_{lb} = 0$ h
$t_{ub} = 33$ h
$\lambda_{p,f,g,h,k} \in [-10, 10]$

$NP = 33$
$G = 1000$
$jDE = DE/rand/2/bin$

$\kappa_x = 10^{-8}$
$\kappa_f = 10^{-8}$

A.2.2. Single orbital element targeting

The first case has one target, which is a semi major axis of $23 \cdot 10^6$ m, the weights W_i for the objective functions are all zero except $W_a = 1.0$. Case 2 targets an eccentricity of 0.6, the weights W_i for the objective functions are all zero except $W_e = 1.0$. Case 3 targets an inclination of $18.5°$, the weights W_i for the objective functions are all zero except $W_i = 1.0$. Case 4 targets an argument of periapsis of $45.0°$, the weights W_i for the objective functions are all zero except $W_i = 1.0$. Case 5 targets a longitude of the ascending node of $20.0°$, the weights W_i for the objective functions are all zero except $W_i = 1.0$. Table A.1 shows the results of the optimization. The column 'Gen' indicates in which generation the last improvement of the objective occurred. The elements which are not targeted are grayed out.

Table A.1: Verification of single orbital element targeting, Δ indicate the absolute difference with respect to the target orbit.

Case	Gen	Δa [m]	Δe[-]	Δi [deg]	$\Delta\omega$ [deg]	$\Delta\Omega$ [deg]
# 1	87	2.9286	4.2868e-03	5.25036e-08	23.9425	0.0000
# 2	97	9.3606e06	1.5768e-08	5.7764e-07	1.6364	0.0000
# 3	517	6.8683e06	3.6534e-02	4.6591e-04	1.5375	6.8244
# 4	61	2.6496e07	6.5286e-02	1.4807e-07	1.9009e-05	0.0000
# 5	631	2.5822e06	1.1762e-01	5.9638	2.1250e01	4.6338e-02

Table A.1 shows that the the optimization converges to the correct orbital elements. However, only single orbital elements are targeted which can be seen in the large differences in the other elements. The convergence of case 3 and case 5 is slower compared to the other cases. These cases correspond to a change in inclination and longitude of the ascending node. These are slowly varying elements and could be more difficult for the optimizer since only little effect can be seen over small time periods as a much larger Δv is required to accomplish a change in these parameters. This effect must be considered in the optimizations of this study. Figure A.6 shows the convergence progress of case 3 and 5.

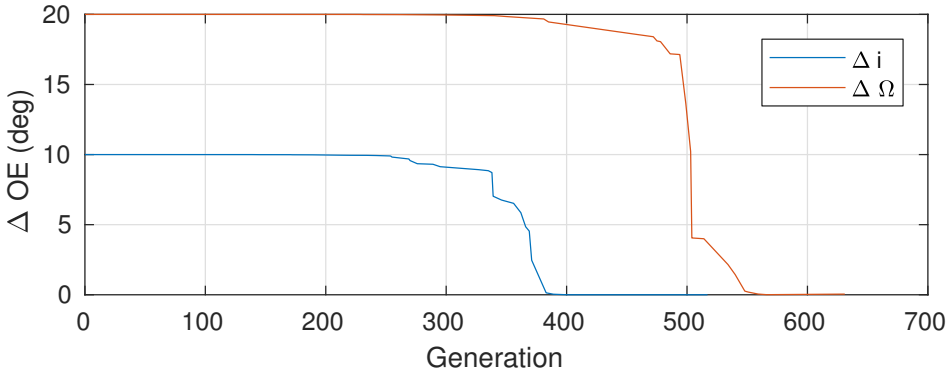

Figure A.6: Convergence progress for the optimization with targets i and Ω.

A.2.3. Multiple orbital elements targeting

When targeting only a single orbital element, as done in Appendix A.2.2, large differences arise in the orbital elements which are not targeted. In this section also these other parameters are targeted. This increases the complexity for the optimizer. Several cases were investigated to verify the optimization with multiple objectives. The target orbit for the optimization is defined by the following orbital elements: $a = 23 \cdot 10^6$m, $e = 0.6$, $i = 18.5°$, $\omega = 45.0°$, and $\Omega = 20.0°$. The initial conditions are as described in Appendix A.2.1. The other simulation parameters are the same as in Appendix A.2.2. The weights are shown in Table A.2. The results are shown in Table A.3.

Table A.2: Weights multiple orbital element targetting verification

Case	W_t	W_a	W_e	W_i	W_ω	W_Ω
# 1	1.0	10.0	10.0	0.0	0.0	0.0
# 2	1.0	0.0	10.0	10.0	0.0	0.0
# 3	1.0	10.0	0.0	10.0	0.0	0.0
# 4	1.0	10.0	0.0	0.0	10.0	10.0

Table A.3: Verification of multiple orbital element targeting

Case	Gen	t_{tof} [s]	Δa [m]	Δe [-]	Δi [deg]	$\Delta\omega$ [deg]	$\Delta\Omega$ [deg]
# 1	742	1.0755e05	3.6448e04	2.1921e-04	2.1921e04	10.000	20.145
# 2	990	8.7949e04	5.5813e06	1.3074e-03	6.8391e-03	46.741	13.950
# 3	785	1.4248e04	1.3851	0.40429	10.000	21.057	20
# 4	322	2.7425e04	44.508	0.42685	10.000	1.4928e-02	20

These results shown in Table A.3, confirms that the optimization with multiple targets is more difficult. It requires more generations to find a solution. The errors between the final and target orbit are larger than found in the single target case in Table A.1. Notice the bad performance in inclination and longitude of ascending node in case 3 and 4. $\Delta i = 10°$ for case 3, which means no inclination change was performed at all. The same holds for the $\Delta\Omega = 20$ in case 4, indicating that no change in longitude of ascending node was performed at all. This again shows that care must be taken with the slowly varying inclination and longitude of ascending node. The good performance in inclination of case 2 could be the result of the high eccentricity, since inclination changes at large apogee are more effective. Considering the results of this section and Appendix A.2.2, it can be concluded that the optimization of the trajectories is working properly, and is considered verified. Furthermore, for the optimization in this thesis, the bounds for λ_h and λ_k are set $1 \cdot 10^5$ times as large as the other costates to increase the probability of the optimizer to change the inclination or longitude of ascending node of the orbit to reduce the casualty risks. If this is not implemented, the out-of-plane freedom of the optimizer is not used are optimal solution could be left out.

A.3. Optimization with simple population map

This section shows the results of the verification of the optimization algorithm with simple population maps. Two cases are considered, one with population depending on the latitude with the highest population density around the equator as shown in Fig. A.7(b), and one with the a longitude dependent population map as shown in Fig. A.8(b). The target is to minimize the amount of casualties inside an impact track of specified dimensions . The following parameters for the satellite and the jDE are used for both cases.

$t_{max} = 4$ days,
$h_{end} < 90$ km,
$K = 0.0025$ m^2/kg,
$I_{sp} = 2000$ s,
$F_{thrust} = 10$ N,
$m = 400$ kg,
$\lambda_{p,f,g} \in [-0.1, 0.1]$,
$\lambda_{h,k} \in [-10000, 10000]$,
$NP = 120$,
$G = 100$,
$jDE = DE/rand/2/bin$,

where t_{max} is the maximum simulation time, this was selected to limit the computational burden of the optimization, h_{end} is the altitude at which the simulation is stopped, at this altitude the amount of casualties is calculated. K, I_{sp}, F_{thrust}, m the ballistic coefficient, specific impulse, thrust and mass of the satellite respectively, chosen arbitrary. At first the costate bounds were all set to $\in [-100, 100]$ as used in Appendix A.2. Similar behavior as in Appendices A.2.2 and A.2.3 was found, which was the difficulty of finding a solution with an inclination change or longitude of ascending node change required. It was found that the contribution of the other costates ($\lambda_{p,f,g}$) were too large and therefore the optimizer had problems finding the trajectories with large changes in i of Ω. This has been fixed by changing the bounds of the costates to the values above as already discussed in Appendix A.2.3 Without these larger bounds for λ_h and λ_k, no change in the inclination was observed at all. The values

for the bounds of the costates as shown in this section are used for the optimization of the actual problem in Chapter 5 and for all verification cases in this chapter. The objective function is given by Eq. (A.5) which is a simplified version of Eq. (3.7) used in the optimizations in this thesis.

$$J = E = \sum_{i}^{n} \sum_{j}^{m} \rho(\phi_{i,j}, \lambda_{i,j}), \tag{A.5}$$

where $n = 20$ is the number of equally spaced along-track points and $m = 2$ the number of equally spaced cross-track points. These values are chosen arbitrarily. i and j indicate the individual impact points. Furthermore, $\rho(\phi_{i,j}, \lambda_{i,j})$ is the population density at coordinates $(\phi_{i,j}, \lambda_{i,j})$ of point (i, j). The points are located around the nominal impact point, where points $(i, 1)$ are located at the start of the track with an along-track distance to the nominal point of $\frac{\Delta d_{at}}{2}$, where Δd_{at} is the along-track length of the impact track. Furthermore, points (i, m) are located at the end of the impact track at a distance $\frac{\Delta d_{at}}{2}$ from the nominal point. Similarly, the points $(1, j)$ are located at a cross-track distance of $\frac{\Delta d_{ct}}{2}$ in negative $\hat{\mathbf{y}}_B$ axis direction as specified in Section 2.1, where Δd_{ct} is the cross-track length of the impact track. Furthermore, the points (n, j) are located at a cross-track distance of $\frac{\Delta d_{ct}}{2}$ in positive $\hat{\mathbf{y}}_B$ axis direction. The controls are the same as in the optimizations of this thesis and repeated in Eq. (A.3).

A.3.1. Latitude dependent population map

The first case uses a population map with the population centered around the equator. The population density decreases towards the poles. The following additional parameters are used for this case:

$a = 6938$ km, $\quad i, \omega, \Omega, \theta = 0°, \quad \Delta d_{ct} = 100$ km.
$e = 0, \quad \Delta d_{at} = 1000$ km,

In Fig. A.7 the best orbit is shown after 100 generations.

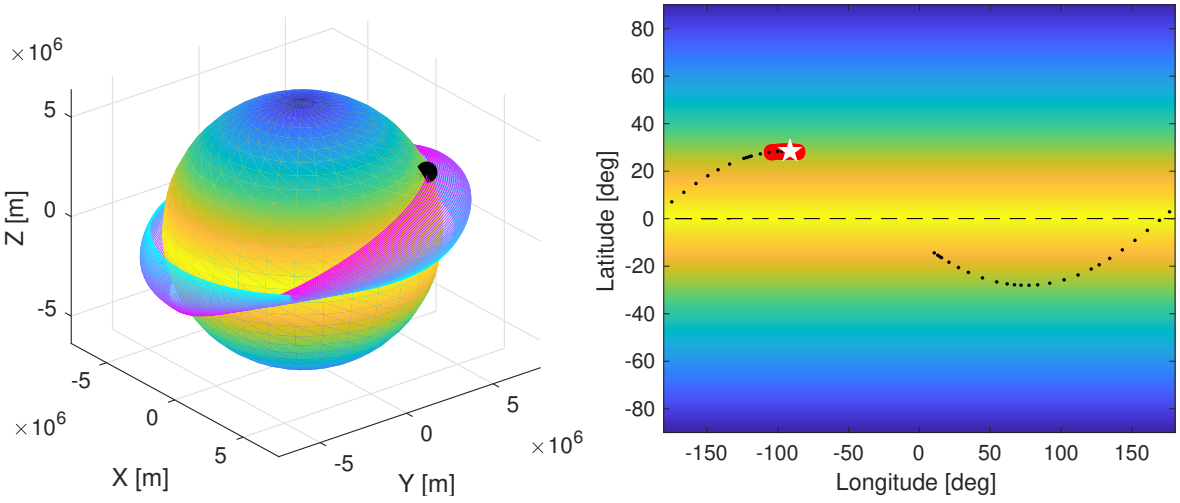

(a) Orbit from turquoise to purple, crash location in black.

(b) impact tracks, dashed line indicates initial track, dotted line indicates final track, red area is impact zone, white star is center of impact zone.

Figure A.7: Verification of optimization with equatorial centered population map.

The verification results presented in Fig. A.7 show the increase of the inclination to decrease the amount of population at the impact location. Furthermore, it demonstrates the timing capability of the optimizer by crashing exactly at the highest latitudes. Furthermore, the altitude is first increased before decreasing again to 90 km altitude. This can be explained by the number of nodes used, namely two. With only two nodes the system is not capable of a constant semi-major axis during inclination change since it has to decrease the altitude at some point to below 90 km. To have enough time for the inclination change, it first increases its altitude. A three node optimization potentially removes this unnecessary movement.

The best costates after 100 generations are:

$$\boldsymbol{\lambda}_0 = \begin{bmatrix} -3.384 \cdot 10^{-5} \\ 8.495 \cdot 10^{-2} \\ -1.059 \cdot 10^{-2} \\ -7.300 \cdot 10^{3} \\ 9.375 \cdot 10^{3} \end{bmatrix}$$

$$\boldsymbol{\lambda}_1 = \begin{bmatrix} 3.435 \cdot 10^{-5} \\ -3.990 \cdot 10^{-2} \\ 3.058 \cdot 10^{-3} \\ -4.691 \cdot 10^{3} \\ 6.001 \cdot 10^{3} \end{bmatrix}$$

These costates confirm the behavior described above. The altitude is first increase as $\lambda_{0,p}$ is negative, then it is decreased as seen by the positive value for $\lambda_{1,p}$. The values for λ_h and λ_k are large at the first node, but at the second node the focus is on the reduction of the altitude. The effects of parameters λ_h and λ_g are opposite in direction between the first and second node. The effect of these parameters is likely counteracted due to this. The simulation time was limited (4 days). Therefore, optima reaching higher latitudes were not achieved since the satellite needs to reach altitudes below 90 km within 4 days. The optimum used the full 4 days for the maneuver. The findings of this section verify the correct linking of the propagation and the optimization for targets which require an inclination change, and verifies the timing capability of the software chain.

A.3.2. Longitude dependent population map

The second case uses a population map which is dependent on the longitude. The density increases from 0° longitude towards $\pm 90°$ longitude and decrease again towards 180◦ longitude. The following additional parameters are used for this case:

$a = 6938$ km,	$\omega, \Omega, \theta = 0°$,	$\Delta d_{at} = 2000$ km,
$e = 0$,	$i = 90°$,	$\Delta d_{ct} = 100$ km

In Fig. A.8 the best impact track after 100 generations is shown. The rotational motion of the planet is the same as that of the Earth.

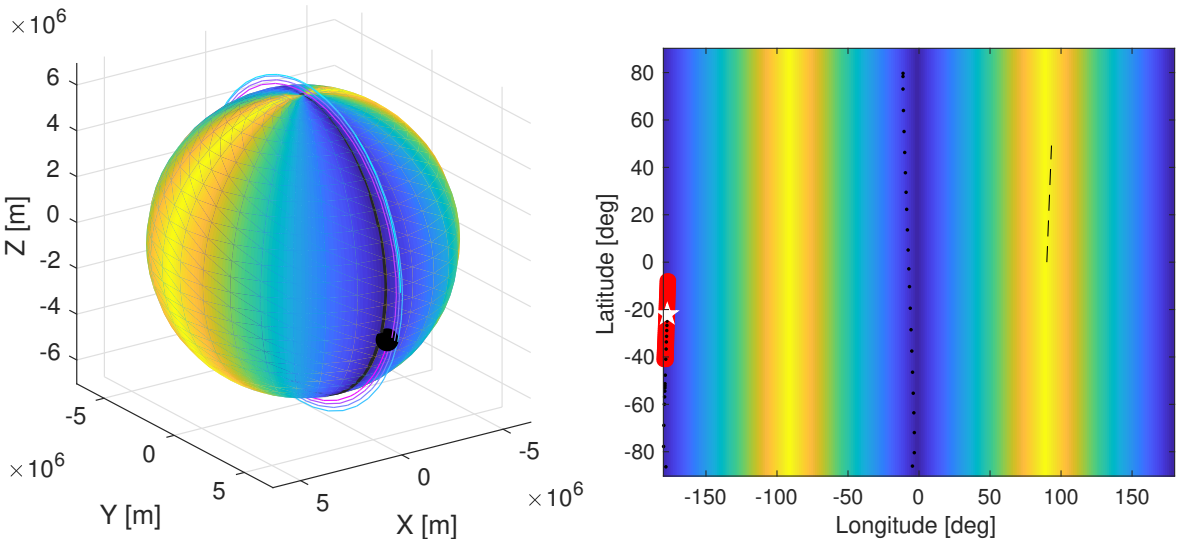

(a) Orbit from turquoise to purple, crash location in black.

(b) impact tracks, dashed line indicates initial track, dotted line indicates final track, red area is impact zone, white star is center of impact zone.

Figure A.8: Verification of optimization with longitude dependent population map.

The results in Fig. A.8 show the timing capability of the optimizer. The semi-major axis is first increased and then decreased until impact, in this time, the planet underneath, is rotated such that the crash occurs at a longitude with low population density. The optimization converges to an impact with a low population density.

The best costates after 100 generations are:

$$\boldsymbol{\lambda}_0 = \begin{bmatrix} -2.397 \cdot 10^{-5} \\ -6.577 \cdot 10^{-2} \\ 1.471 \cdot 10^{-2} \\ 8.606 \cdot 10^{1} \\ -8.786 \cdot 10^{1} \end{bmatrix}$$

$$\boldsymbol{\lambda}_1 = \begin{bmatrix} 8.054 \cdot 10^{-2} \\ -6.382 \cdot 10^{-2} \\ -8.433 \cdot 10^{-2} \\ 4.865 \cdot 10^{3} \\ 7.141 \cdot 10^{2} \end{bmatrix}$$

These costates confirm the behavior described above. The altitude is first slightly increased as $\lambda_{0,p}$ is negative, then it is decreased as seen by the large positive value for $\lambda_{1,p}$. Note that the satellite crashes much earlier than the satellite in Appendix A.3.1. The nodes are spaced 4 days apart. Therefore, the costates at the first node mostly determine the trajectory of the satellite. The costates affecting the inclination of the orbit λ_h and λ_k are relatively low at the first node, indicating that the focus is on the in plane movement of the satellite. The other costates do not indicate clear behavior. The results of this optimization clearly indicate the timing capabilities of the optimizer which is considered important for minimizing the casualty risk. The findings of this section verify the correct linking of the propagation and the optimization for impact timing. Based on the findings of bothAppendix A.3.2 and Appendix A.3.1 the complete software chain for the propagation and optimization as implemented in this research is verified.

B

Optimal low-thrust trajectories.

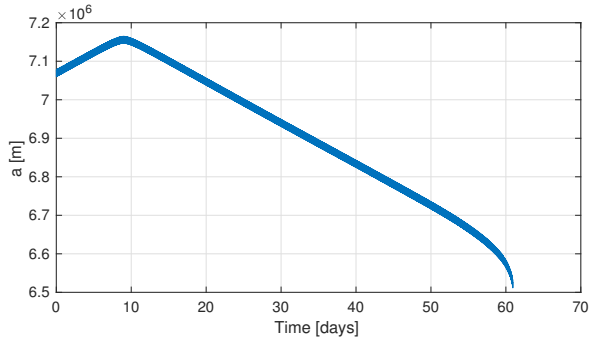

(a) Semi-major axis.

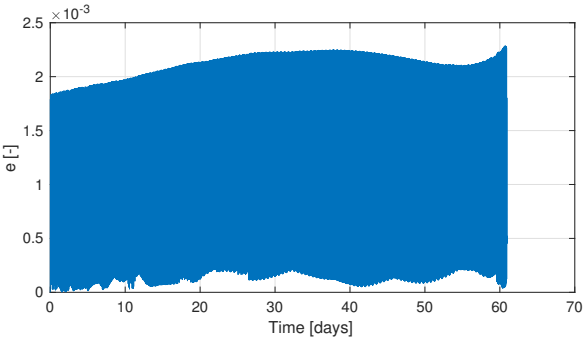

(b) Eccentricity.

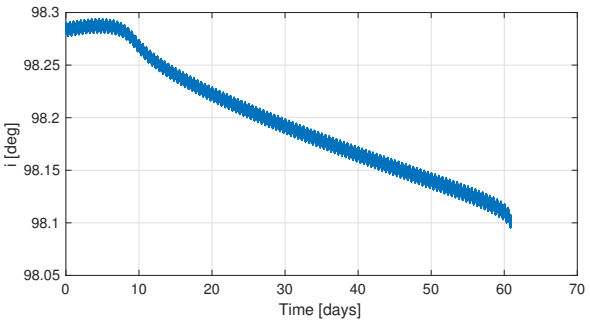

(c) Inlination

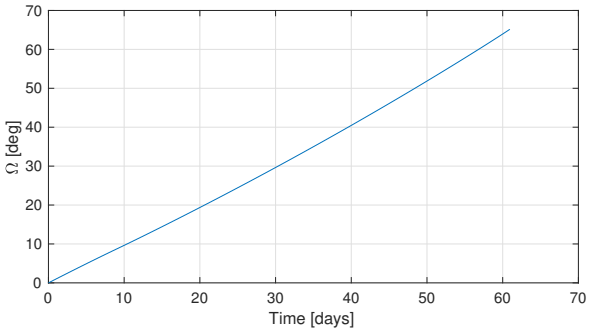

(d) Longitude of ascending node.

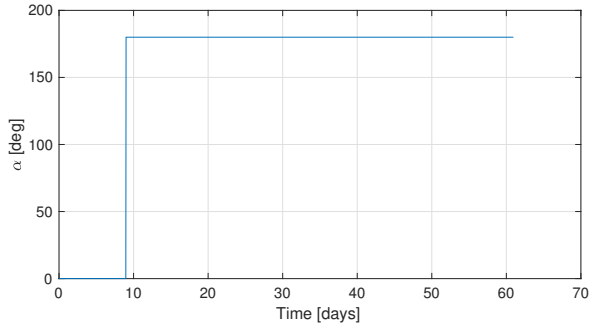

(e) Pitch thrust steering angle.

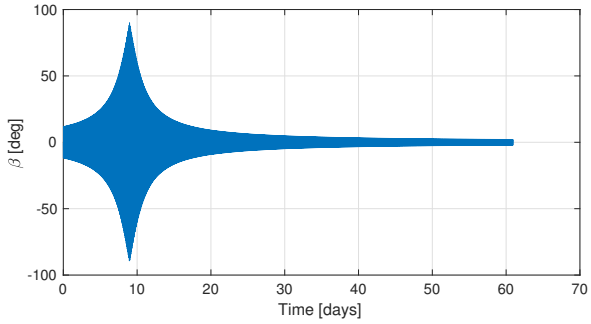

(f) Yaw thrust steering angle.

Figure B.1: Optimal low-thrust trajectory case 1: PARASOL down to 150 km altitude, together with optimal thrust profile.

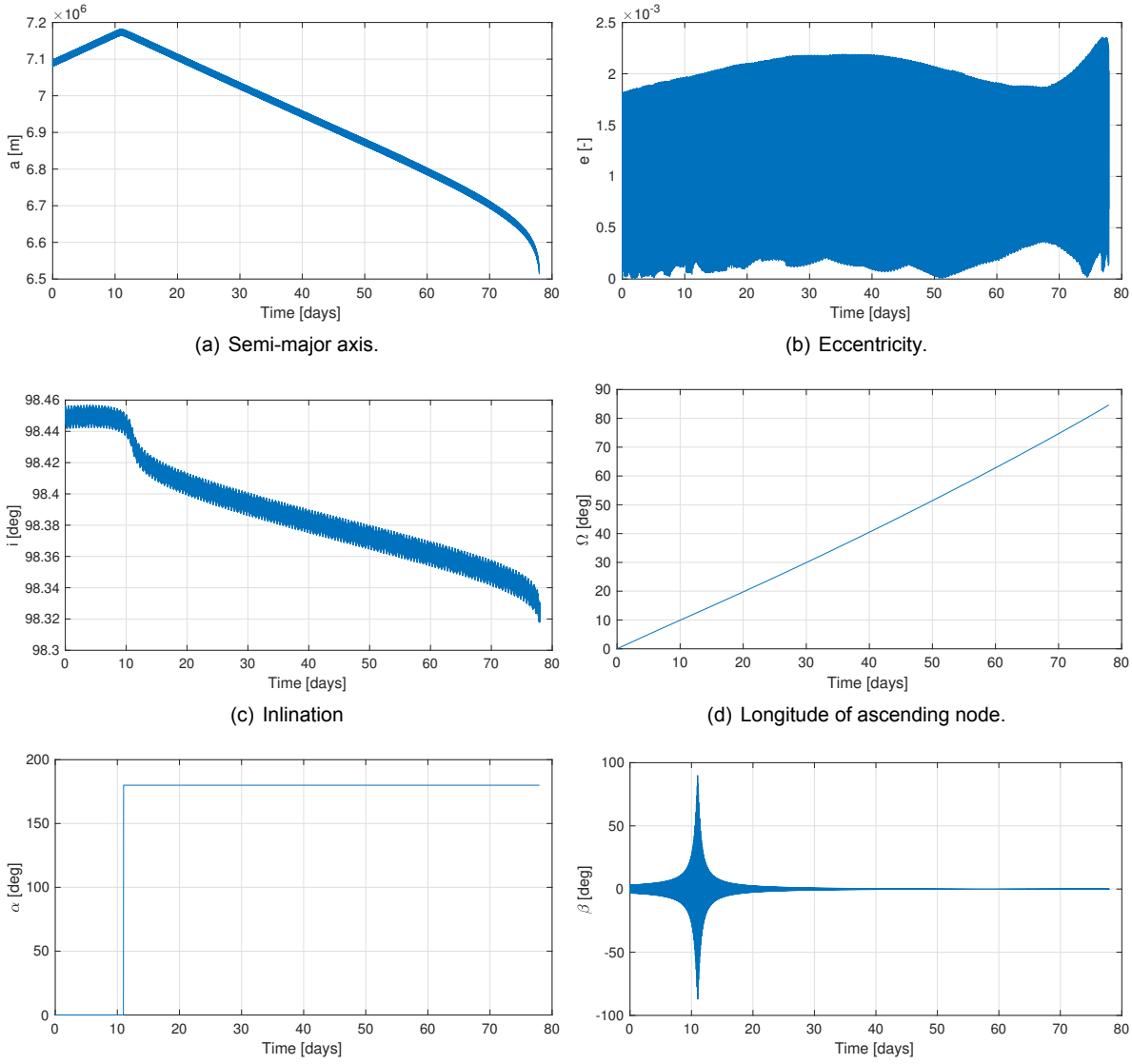

(a) Semi-major axis.

(b) Eccentricity.

(c) Inlination

(d) Longitude of ascending node.

(e) Pitch thrust steering angle.

(f) Yaw thrust steering angle.

Figure B.2: Optimal low-thrust trajectory case 2: SMOS down to 150 km altitude, together with optimal thrust profile.

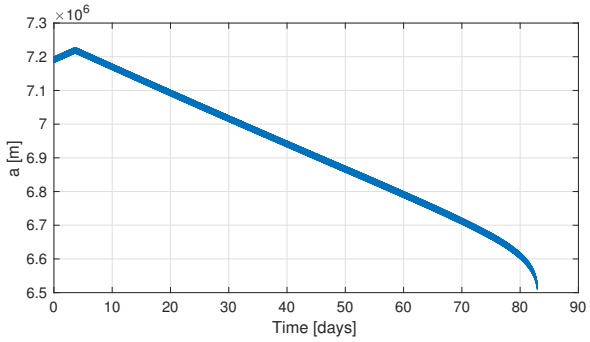

(a) Semi-major axis.

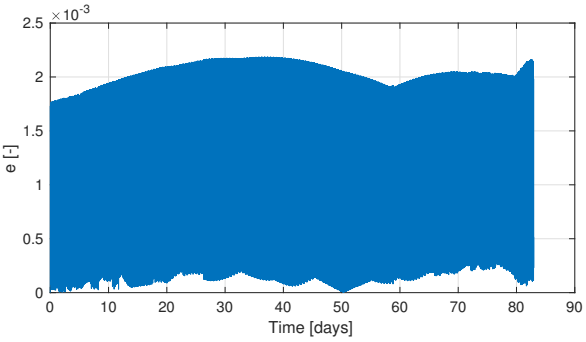

(b) Eccentricity.

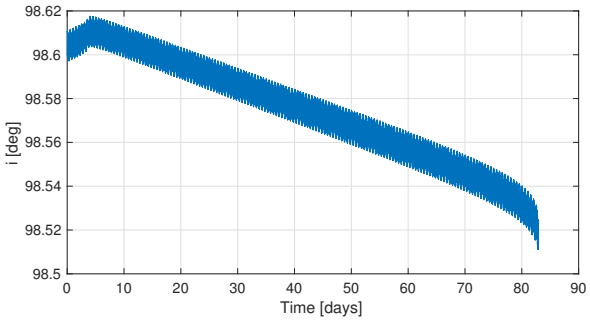

(c) Inlination

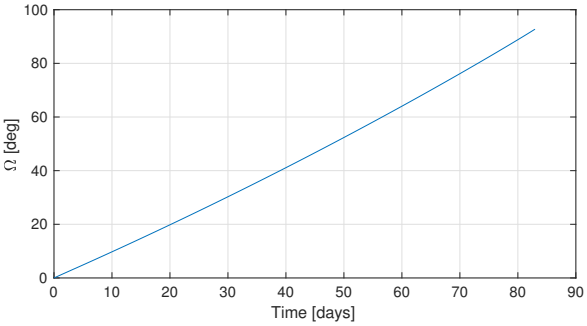

(d) Longitude of ascending node.

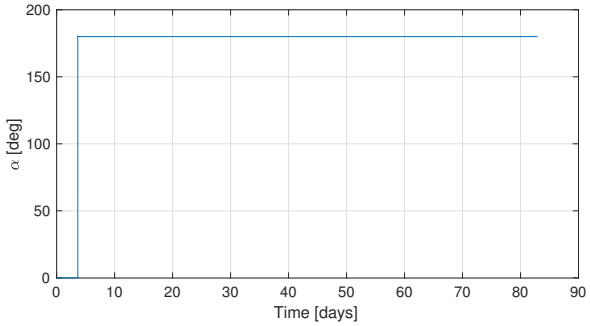

(e) Pitch thrust steering angle.

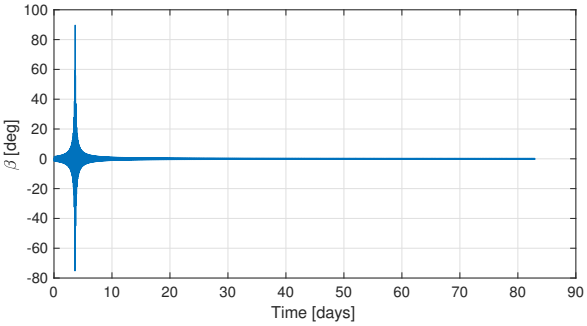

(f) Yaw thrust steering angle.

Figure B.3: Optimal low-thrust trajectory case 3: SPOT5 down to 150 km altitude, together with optimal thrust profile.

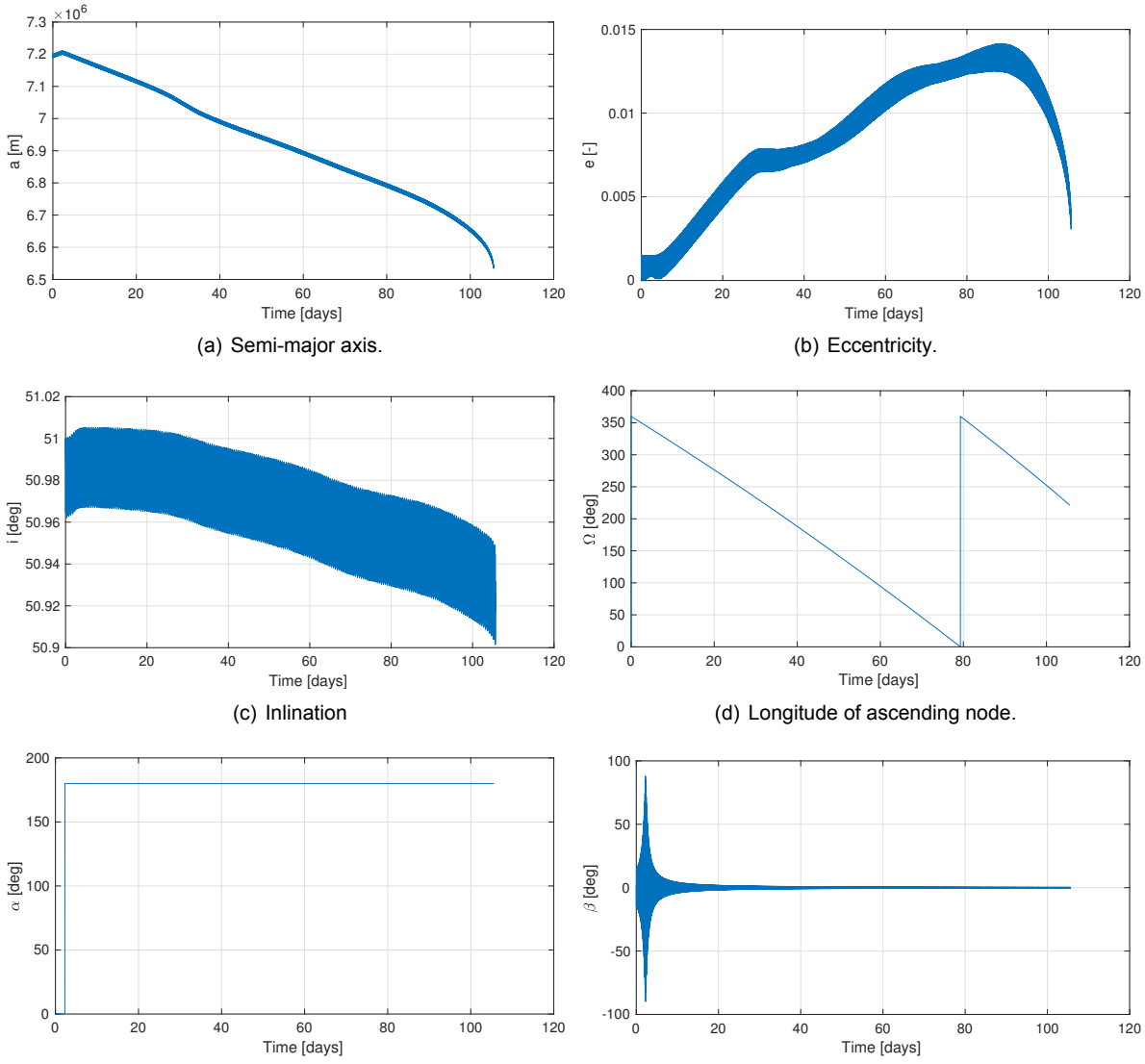

(a) Semi-major axis.

(b) Eccentricity.

(c) Inlination

(d) Longitude of ascending node.

(e) Pitch thrust steering angle.

(f) Yaw thrust steering angle.

Figure B.4: Optimal low-thrust trajectory case 4: SPOT5LIKE down to 150 km altitude, together with optimal thrust profile.

Bibliography

[1] ESA, “Statement of work ESA express procurement EXPRO: Impact of Controlled and Semi-Controlled Re-Entry on Spacecraft Design,” , Dec. 2015.

[2] ESA Director General’s Office, “Space Debris Mitigation Policy for Agency Projects, ESA/ADMIN/IPOL(2014)2,” , March 2014.

[3] Inter-agency space debris coordination committee steering group, “Space Debris, IADC Assessment Report for 2011,” , 2013.

[4] ESA, “ESA Space Debris Mitigation Compliance Verification Guidelines,” , Feb. 2015.

[5] Boniface, C., Charbonnier, J., et al., “An overview of electric propulsion activities at CNES,” 2017.

[6] Gaudel, A., Hourtolle, C., et al., “De-Orbit Strategies With Low-Thrust Propulsion,” *Space Safety is No Accident: The 7th IAASS Conference*, edited by T. Sgobba and I. Rongier, Springer International Publishing, Cham, 2015, pp. 59–68.

[7] Janovsky, R., “End-of-life de-orbiting strategies for satellites,” *54th International astronautical congress of the international astronautical federation, the international academy of astronautics, and the international institute of space law*, American Institute of Aeronautics and Astronautics, 2003.

[8] Ferrier, P., Crebassol, P., et al., “VENμS Vegetation and environment monitoring on a new micro satellite,” *IEEE International Geoscience and Remote Sensing Symposium*, 2010.

[9] Dankanich, J., “Low-thrust Propulsion Technologies, Mission Design, and Application,” *Aerospace Technologies Advancements*, InTech, 2010, p. 492.

[10] Izzo, D., “PYGMO and PYKEP: Open source tools for massively parallel optimization in astrodynamics (the case of interplanetary trajectory optimization),” International Conference on Astrodynamics Tools and Techniques, 2012.

[11] Kluever, C. ., *Spacecraft trajectory optimization*, Cambridge University Press, 2010. Chapter 5.

[12] Ronse, A. L. A. B., and Mooij, E., “Statistical impact prediction of decaying objects,” *Journal of Spacecraft and Rockets*, Vol. 51, No. 6, 2014, pp. 1797–1810.

[13] Geul, J., Mooij, E., and Noomen, R., “Analysis of Uncertainties and Modeling in Short-Term Reentry Predictions,” *Journal of Guidance, Control, and Dynamics*, 2018, pp. 1–14.

[14] Center For International Earth Science Information Network, “Gridded population of the world, version 4 (GPWv4): population density adjusted to match 2015 revision of UN-WPP country totals, revision 10,” Accessed:25/01/2018, 2017.

[15] ESA, Institute of Aerospace Systems, Technische Universitat Braunschweig, “DRAMA Final Report, Upgrade of ESA’s Space Debris Mitigation Analysis Tool Suite,” , 2014.

[16] Opiela, J. N., “Improvements to NASA’s Estimation of Ground Casualties from Reentering Space Objects,” *54th International Astronautical Congress of the International Astronautical Federation, the International Academy of Astronautics, and the International Institute of Space Law*, American Institute of Aeronautics and Astronautics, 2003.

[17] Tapley, B. D., Schutz, B. E., and Born, G. H., *Statistical orbit determination*, Elsevier Acedemic Press, 2004.

[18] Mooij, E., “The motion of a vehicle in a planetary atmosphere,” Delft University of Technology, Faculty of Aerospace Engineering, Dec. 1994.

[19] Vallado, D. A., *Fundamentals of Astrodynamics and Applications*, 3rd ed., Microcosm Press, Spinger, 2007.

[20] Ho, J., Park, I., et al., “The comparison of the classical Keplerian Orbit Elements, non-singular orbital elements (equinoctial elements), and the cartesian state variables in Lagrange planetary equations with J_2 perturbation: Part 1,” *Journal of Astronamy and Space Science*, 2011.

[21] Montenbruck, O., and Gill, E., *Satellite Orbits*, Springer Nature, 2000.

[22] Hintz, G. R., “Survey of Orbit Element Sets,” *Journal of Guidance, Control, and Dynamics*, Vol. 31, No. 3, 2008, pp. 785–790.

[23] Walker, M., Ireland, B., and Owens, J., “A set of modified equinoctial orbit elements,” *Celestial Mechanics*, Vol. 36, No. 4, 1983, pp. 409–419.

[24] Walker, M., “Errata: A set of Modified Equinoctial Orbit Elements,” *Celestial Mechanics*, Vol. 38, No. 4, 1986.

[25] Picone, J. M., Hedin, A. E., et al., “NRLMSISE-00 empirical model of the atmosphere: Statistical comparisons and scientific issues,” *Journal of geophysical research*, Vol. 107, No. A12, 2002, pp. SIA 15–1–SIA 15–16.

[26] Vallado, D. A., and Kelso, T., “Earth Orientation Parameter and Space Weather Data for Flight Operations,” *23rd AAS/AIAA Space Flight Mechanics Meeting*, 2013.

[27] Lemoine, F. G., Kenyon, S., et al., “The development of the Joint NASA GSFC and the National Imagery and Mapping Agency (NIMA) geopotential model EGM96.” *NASA/TP-1998-206861*, 1998.

[28] Acton, C., “Ancillary Data Services of NASA’s Navigation and Ancillary Information Facility,” *Planetary and Space Science*, Vol. 44, No. 1, 1996, pp. 65–70.

[29] Acton, C., Bachman, N., et al., “A look towards the future in the handling of space science mission geometry,” *Planetary and Space Science*, Vol. 150, 2018, pp. 9–12.

[30] Meng, Y., “Minimum-fuel spacecraft transfer trajectory solved by direct/indirect hybrid continuation method,” *Hangkong Xuebao/Acta Aeronautica et Astronautica Sinica*, Vol. 38, No. 1, 2017, p. 22.

[31] Kluever, C. A., and R., O. S., “Direct approach for computing near-optimal low-thrust Earth-orbit transfers,” *Journal of Spacecraft and Rockets*, Vol. 35, No. 4, 1998, p. 509–515.

[32] Boudestijn, E., “Development of a low-thrust Earth centered transfer optimizer for the preliminary mission design phase.” Master’s thesis, Delft University of Technology, 2014.

[33] Jenkins, M. G., “Optimization of low-thrust trajectories in Earth-centered orbit, the case for CleanSpace One,” Master’s thesis, Delft University of Technology, 2015.

[34] Bulirsch, R., and Stoer, J., *Introduction to Numerical Analysis*, Spinger-Verlag, 1991.

[35] Burden, R. L., and Douglas, F. J., *Numerical analysis*, 7th ed., Australia Brooks/Cole, 2001.

[36] Dirkx, D., and Mooij, E., “Propagation and optimization: numerical integration,” (lecture slides), 2017.

[37] Wang, D., Tan, D., and Liu, L., “Particle swarm optimization algorithm: an overview,” *Soft Computing*, Vol. 22, No. 2, 2017, pp. 387–408.

[38] Vavrina, M. A., and Howell, K. C., “Global Low-Thrust Trajectory Optimization through Hybridization of a Genetic Algorithm and a Direct Method,” *AIAA/AAS Astrodynamics Specialist Conference and Exhibit*, American Institute of Aeronautics and Astronautics, 2008.

[39] Storn, R., and Price, K., “Differential Evolution - A Simple and Efficient Heuristic for global Optimization over Continuous Spaces,” *Journal of Global Optimization*, Vol. 11, 1997, pp. 341–359.

[40] Vavrina, M., and Howell, K., “Multiobjective optimization of low-thrust trajectories using a genetic algorithm hybrid,” *Advances in the Astronautical Sciences*, Vol. 134, 2009, pp. 781–800.

[41] Yamamoto, T., Sato, S., et al., “Mission design of DESTINY+,” *International Astronautical Congress*, 2016.

[42] Taheri, E., Li, N., and Kolmanovsky, I., “Co-state initialization for the minimum-time low-thrust trajectory optimization,” *Advances in Space Research*, Vol. 59, No. 9, 2017, pp. 2360–2373.

[43] Lin, H.-S., He, B., et al., “Design of low-thrust multitask exploration orbit based on gravity-assist,” *Guti Huojian Jishu/Journal of Solid Rocket Technology*, Vol. 40, No. 1, 2017, pp. 121–127.

[44] Jimeniz-Liuva, D., “Hybrid optimization of low-thrust many-revolutions trajectories with coasting arcs and longitude targeting for propellant minimization.” Master’s thesis, Delft University of Technology, 2017.

[45] Eiben, A. E., Hinterding, R., and Michalewicz, Z., “Parameter Control in Evolutionary Algorithms,” *IEEE Transactions on Evolutionary Computation*, Vol. 3, 1999, pp. 124–141.

[46] Brest, J., Greiner, S., et al., “Self-Adapting Control Parameters in Differential Evolution: A Comparative Study on Numerical Benchmark Problems,” *IEEE Transaction on Evolutionary Computation*, Vol. 10, 2006, pp. 646–657.

[47] Ao, Y., and Chi, H., “Experimental Study on Differential Evolution Strategies,” *2009 WRI Global Congress on Intelligent Systems*, Vol. 02, IEEE, Los Alamitos, CA, USA, 2009, pp. 19–24.

[48] Storn, R., and Price, K., “Minimizing the real functions of the ICEC’96 contest by Differential Evolution.” *IEEE*, 1996.

[49] Price, K., Storn, R., and Lampinen, J. A., *Differential Evolution - A Practical Approach to Global Optimization*, Springer, 2006.

[50] Bowman, A. W., and Azalini, A., *Applied Smoothing Techniques for Data Analysis*, 1997.

[51] Klinkrad, H., Fritsche, B., Lips, T., and Koppenwallner, G., *Re-entry prediction and on-ground risk estimation*, Springer Berlin Heidelberg, Berlin, Heidelberg, 2006, pp. 241–288.

[52] Steiger, C., Romanazzo, M., et al., “The de-orbiting of ESA’s Gravity Mission GOCE - Spacecraft Operations in Extreme Drag Conditions,” *SpaceOps conferences*, 2014.

[53] Pardini, C., and Anselmo, L., “On the accuracy of satellite reentry predictions,” *Advances in Space Research*, Vol. 34, No. 5, 2004, pp. 1038–1043.

[54] H.Klinkrad, “Methods and Procedures of Re-Entry Predictions at ESA,” 2013.

[55] United Nations, “World Population Prospects, Data Booklet,” , 2017.

[56] Hogervorst, F., “Restricting the re-entry area for semi-controlled LEO satellites using low thrust propulsion.” , Feb 2017. Literature study.